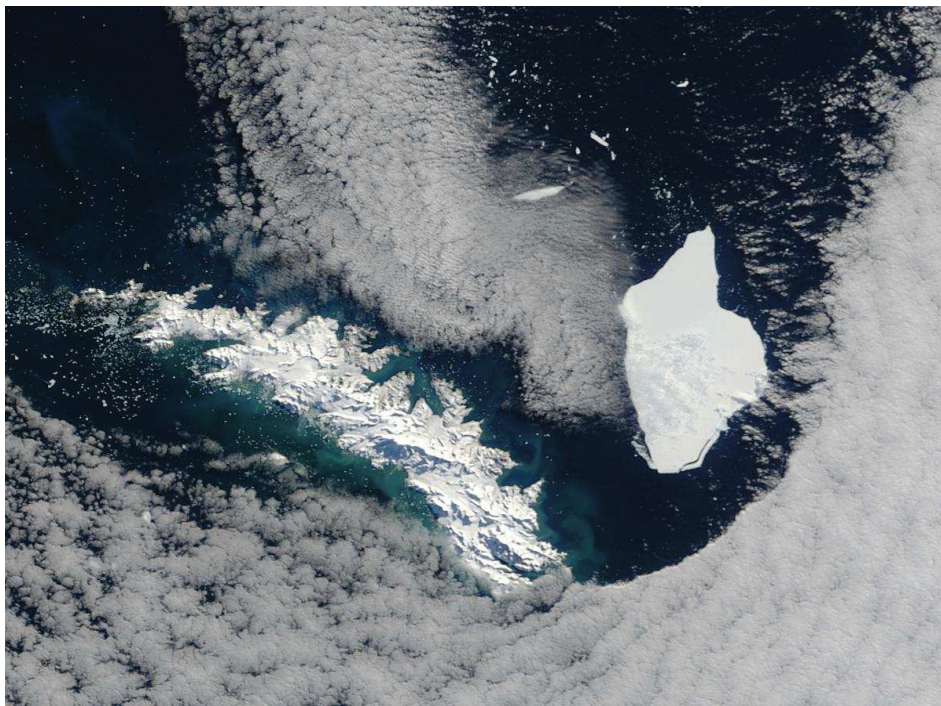


# **EVOLUTION OF ANTARCTIC TABULAR ICEBERGS**

**DANIELA JANSEN**

**ALFRED WEGENER INSTITUTE FOR POLAR AND MARINE RESEARCH  
BREMERHAVEN  
GERMANY**

**APRIL 2008**



Dissertation zur Erlangung des Grades Dr. rer. nat.  
vorgelegt dem Fachbereich Geowissenschaften  
der Universität Bremen

Titelbild: Modis Rapid Response Team, NASA/GSFC

---

# Contents

<b>Abstract</b>	<b>1</b>
<b>Zusammenfassung</b>	<b>3</b>
<b>1 Introduction</b>	<b>5</b>
1.1 Tabular icebergs and the mass balance of the Antarctic ice sheet	5
1.2 Processes governing tabular iceberg evolution	9
1.3 Objectives	10
<b>2 Publication synopsis</b>	<b>13</b>
2.1 Model experiments on large tabular iceberg evolution: ablation and strain thinning	13
2.2 Basal melting of A-38B: A physical model constrained by satellite observations	13
2.3 Iceberg-generated tremor in the vicinity of South Georgia Island	14
<b>3 Ice flow and thermodynamic model</b>	<b>15</b>
3.1 Fundamental principles of ice dynamics in ice shelves and icebergs	16
3.2 Diagnostic model equations: ice shelf velocities	19
3.3 Prognostic model equations: temperature and ice thickness	22
3.4 Numerical solution	23
<b>4 Basal melting of tabular icebergs</b>	<b>25</b>
4.1 A thermodynamic model for the ice-ocean interaction	26
4.2 The turbulent exchange velocity at the ice-ocean boundary	27
4.3 Freeboard changes derived from ICESat altimetry	28

<b>5 Seismic events originated from tabular icebergs</b>	<b>31</b>
5.1 Data and data processing	32
5.2 Grounded iceberg events: stick-slip-induced tremor	33
5.3 Floating iceberg events: fluid-flow-induced tremor	34
5.4 Ocean swell as a source of iceberg fracturing?	37
<b>6 Conclusion and outlook</b>	<b>41</b>
<b>Bibliography</b>	<b>45</b>
<b>Danksagung</b>	<b>53</b>
<b>Appendix –Publications</b>	<b>55</b>
A Model experiments on large tabular iceberg evolution: ablation and strain thinning	55
B Influence of Inlets on tabular iceberg evolution	77
C Basal melting of A-38B: A physical model constrained by satellite observations	83
D Iceberg-generated tremor in the vicinity of South Georgia Island	101

# Abstract

The aim of this study was to investigate and quantify the role of the various processes affecting a large tabular iceberg during a typical lifecycle from calving to final decay. The thesis comprises three publications, each addressing a different aspect of the evolution of the tabular iceberg A-38B, which calved from the Ronne Ice Shelf in October 1998.

The first publication is focussed on inherent ice dynamics. To investigate the relevance of strain thinning to iceberg evolution, a numerical ice shelf model was adapted to the iceberg case. The interaction with atmosphere and ocean was included in the model, but parameterised in a simple way and estimated on the base of measurements and external model data. A five year simulation of the evolution of iceberg A-38B showed that basal melting is the primary cause for change of iceberg geometry during drift, whereas strain thinning is only relevant in cold areas where basal melting is low.

Thus, the second part of the thesis concentrates on an improved basal melting approach. In the drift period between the entering of the Scotia Sea in March 2003 until the grounding near South Georgia in 2004, freeboard changes of A-38B were observed from analysis of ICESat Laser altimeter profiles. The iceberg melt rate was then fitted by varying the turbulent exchange parameters for temperature and salt at the ice ocean boundary to match the altimeter results. The data analysis indicated, that the iceberg passed through three melting regimes during its drift, each characterised by a different magnitude of turbulent exchange between iceberg and ocean depending on drift conditions. The analysis showed also that drifting tabular icebergs export more melt water to the Scotia Sea than previously assumed.

To shed light onto the final stage of iceberg evolution, the third publication is focussed on the investigation of the grounding process of A-38B and related seismic events. The characteristic spectrograms of such signals probably represent excitation of elastic modes of the ice masses by stick-slip friction. Data records from the seismic station on South Georgia Island also comprised harmonic tremor events generated by the floating iceberg A-43G. This second class of iceberg-generated tremor is probably excited by fluid flow through a major rift structure and is related to particular current regimes around the iceberg.



# Zusammenfassung

Das Ziel der vorliegenden Arbeit war die Untersuchung und Bewertung der verschiedenen Prozesse, die auf einen großen Tafeleisberg während eines typischen Driftverlaufs einwirken. Die Arbeit umfasst drei Publikationen, die jede für sich einen bestimmten Aspekt der Entwicklung des Tafeleisberges A-38B beleuchten, der im Oktober 1998 vom Ronne-Schelfeis gekalbt ist.

Im ersten Teil der Arbeit wurde hauptsächlich die innere Eisdynamik eines Tafeleisberges betrachtet. Um mehr über die Bedeutung der gravitationsbedingten Ausdünnung zu erfahren, wurde ein bereits bestehendes eisdynamisches Schelfeismodell auf die veränderten Bedingungen eines Tafeleisberges angepasst. Der Einfluss von Ozean und Atmosphäre auf den Eisberg wurde ebenfalls in diesem Modell berücksichtigt, in diesem ersten Teil jedoch näherungsweise mit Messdaten und externen Modellergebnissen parametrisiert. Eine Simulation der Entwicklung des Tafeleisberges A-38B über fünf Jahre seiner Drift zeigte, dass basales Schmelzen den bei weitem größten Anteil an der Veränderung der Eisbergform während der Drift ausmacht. Ausdünnung aufgrund von eisdynamischen Prozessen spielte hingegen nur in sehr kalten Gebieten eine Rolle, in denen die basalen Schmelzraten gering waren.

Aus diesem Grund zielt der zweite Teil der vorliegenden Arbeit auf die Verbesserung des basalen Schmelzansatzes: Während der Drift durch die Scotia Sea und der Gründungsphase nahe der Insel South Georgia dokumentierten mehrere ICESat Laser-Altimeter-Profile die Änderung des Freibords von A-38B. Durch Variation des turbulenten Austauschkoefizienten für Temperatur und Salz an der Eisberg-Ozean-Grenzschicht wurden die Schmelzraten auf die von ICESat gemessenen Werte angepasst. Die Ergebnisse dieser Anpassung zeigten, dass die Schmelzrate des Eisberges abhängig von den Driftbedingungen variierte und weit mehr Süßwasser in Form von Eisbergen in die Scotia Sea exportiert wurde als bisher angenommen.

Um das letzte Stadium der Eisbergentwicklung näher zu betrachten, ist der letzte Teil der Arbeit der Untersuchung von Gründungsprozessen und den damit verbundenen seismischen Ereignissen gewidmet. Die charakteristischen Spektrogramme solcher Signale erklären sich möglicherweise dadurch, dass elastische Moden des Eiskörpers durch den

Wechsel von Haften und Gleiten (Stick-Slip Prozess) angeregt werden. Die Analyse der Daten der seismischen Station auf der Insel South Georgia enthielten allerdings auch Ereignisse, die eindeutig einem frei schwimmenden Eisberg, A-43G, zugeordnet werden konnten. Diese zweite Klasse von durch Eisberge verursachten Tremor-Effekten wird wahrscheinlich durch den Wasserfluss durch Spalten im Eisberg angeregt und ist abhängig von bestimmten Strömungsbedingungen an der Öffnung der Spalten.

# 1

## Introduction

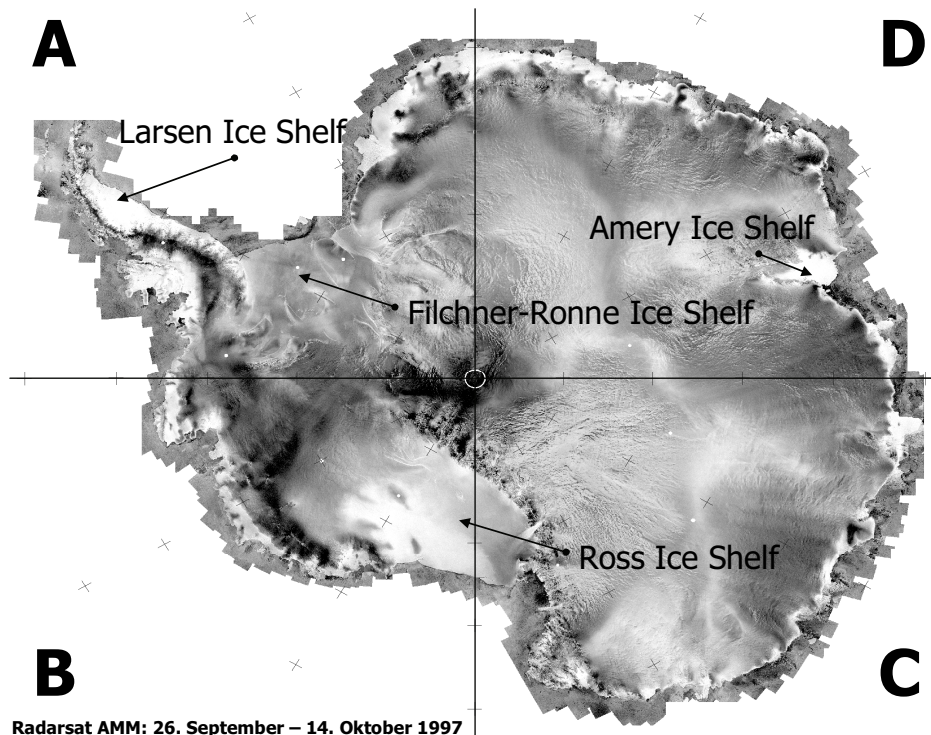
### 1.1 Tabular icebergs and the mass balance of the Antarctic ice sheet

Large tabular icebergs calved from ice shelves at the periphery of the Antarctic continent are remarkable glacial features of the earth's southern polar region. Covering thousands of square kilometres, several hundred meters thick and deteriorating progressively during their drift in the Southern Ocean, they represent active components of the ice sheet–ice shelf–ocean system. Calving at the ice fronts of Antarctica leads to a mean annual mass loss of about  $2000 \text{ Gt a}^{-1}$ , representing by far the largest negative term in the overall mass budget of the ice sheet (*Jacobs et al.*, 1992). About one half of the mass loss rate results from detachment of small icebergs, whereas the second half is due to calving of large tabular icebergs with a major axis greater than 28 km. Since the calving cycles of the latter mostly amount to several decades, the total number of large iceberg break-offs per year is subject to strong variations (e.g., *Jacobs et al.*, 1992).

Calving generally confines the seaward extensions of ice shelf bodies and is part of the usual cycle of steady ice front advance and sudden retreat, while in the long-term mean an almost stationary frontal line position is observed. This mean ice shelf front position is determined by the furthest seaward pinning points of the ice shelf (e.g. *Grosfeld and Sandhäger*, 2004). Beyond this boundary the ice-flow is no longer confined by the bay geometry. Thus, the ice shelf also spreads perpendicularly to the main flow direction. This particular stress regime leads to the formation of large rifts or inlets perpendicular to the ice shelf front (e.g. *Lazzara et al.*, 1999). *Joughin and MacAyeal* (2005) used InSAR (Interferometric Synthetic Aperture Radar) data to measure the opening rates of such rifts. While the growth phase of the inlets may last decades, the actual calving process of the inlet-confined ice shelf tongues is caused by abrupt crack propagation, usually along a straight line connecting two inlet tips. In contrast to the propagation of the slow growing rifts, which can be predicted by means of linear fracture mechanics (*Hamann and Sandhäger*, 2006), the final calving mechanism is not yet understood in detail (*Benn et al.*, 2007).

In contrast to the regular calving events, which are part of the natural mass loss compensated by advection due to ice shelf spreading, irreversible iceberg discharge leads to a partial or total loss of formerly stable ice

shelves. An example is the disintegration of the Larsen A and B Ice Shelf at the north-eastern coast of the Antarctic Peninsula. This ice shelf collapse, which released a huge amount of smaller icebergs into the Weddell Sea, took place in early 1995 and 2002 and was associated with regional atmospheric warming and increased surface melting (Rott *et al.*, 1998; Rack and Rott, 2004; Scambos *et al.*, 2000).



Radarsat AMM: 26. September – 14. Oktober 1997

**Figure 1.1:** RADARSAT mosaic of the Antarctic Ice Shelf. Tabular icebergs are named by a sequential number and the letter for their particular quadrant of origin. Image courtesy: Canadian Space Agency RADARSAT 1997.

The calving of large tabular icebergs with diameters of tens of kilometres is restricted to the large Antarctic ice shelf systems and some glacier tongues. The National Ice Center (NIC; Washington D.C., USA) provides an iceberg data base for tabular icebergs with a major axis greater than 18.5 km (<http://www.natice.noaa.gov/products/iceberg/index.htm>). These records began in 1976 and were initially based on visible and infrared satellite data, supplemented with ship or aircraft reconnaissance (Long *et al.*, 2002). The icebergs are named with a letter which determines the quadrant of origin (fig 1.1), and a sequential number. Icebergs originating in the Weddell- and Bellinghausen Seas are labelled with the letter A. This includes icebergs calved from the Filchner-Ronne Ice Shelf and the Larsen C Ice Shelf, but also large icebergs calved off the Pine Island Glacier or the Twaites Glacier. B stands for the Ross Sea up to 180° W and is therefore used for most of the Ross Ice Shelf icebergs (e.g. B-15, fig 1.2). Icebergs labelled with the letter

C originate at the eastern part of the Ross Ice Shelf and at glacier tongues between 180 and 90° E. The letter D denotes icebergs from the final quadrant, which mainly stem from the Amery Ice Shelf.

## Tabular iceberg B-15

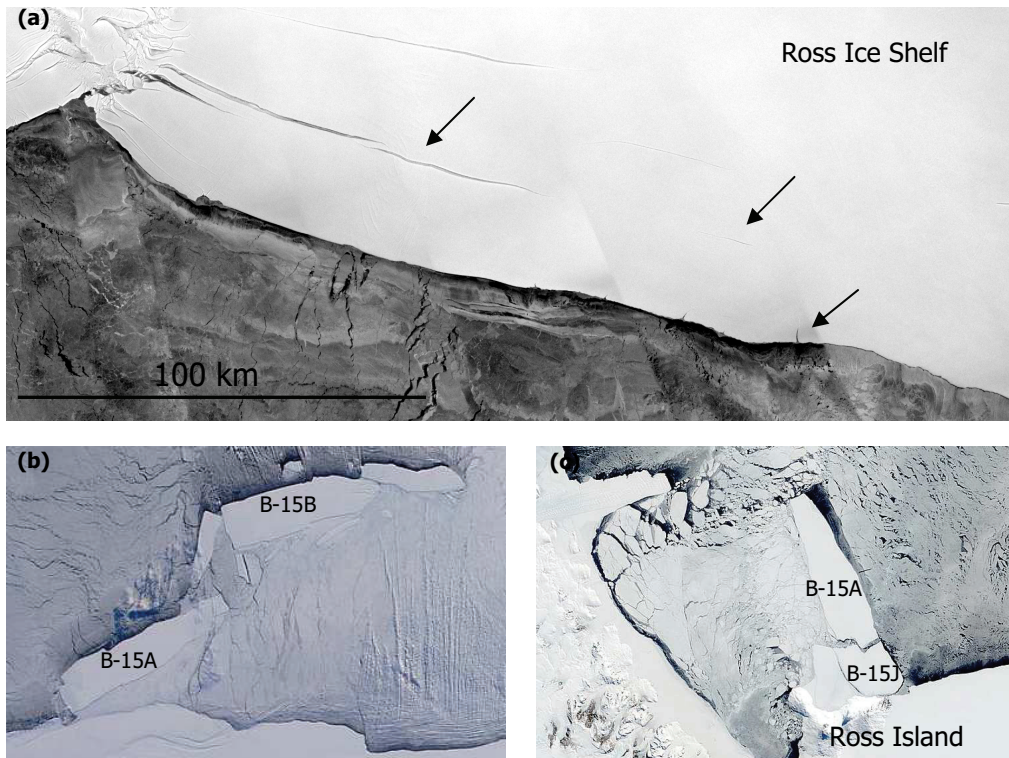


**Figure 1.2:** Iceberg from the Ross Ice Shelf

Iceberg B-15, which calved from the Ross Ice Shelf in March 2000, covered an area of dimensions 290 km by 37 km shortly after its calving and remains the largest berg ever observed (*Young, 2001*). **(a)**: The calving line followed a pre-existing rift structure parallel to the ice shelf front, indicated by the arrows. **(b)**: B-15 broke apart into several sections of which one, B-15A, grounded near Ross Island and had major impact on the sea ice conditions, leading to problems with the shipping access to McMurdo Sound. **(c)**: In October 2003, it finally broke apart and continued its drift to the north and west. Some of the smaller icebergs, which calved from the Ross Ice Shelf near Roosevelt Island in 2000, even reached the southern coast of New Zealand in late 2006 (*Cull, 2007*). Image courtesy: Canadian Space Agency RADARSAT 1997 and MODIS Rapid Response Team NASA/GFSC.

## Tabular iceberg A-38

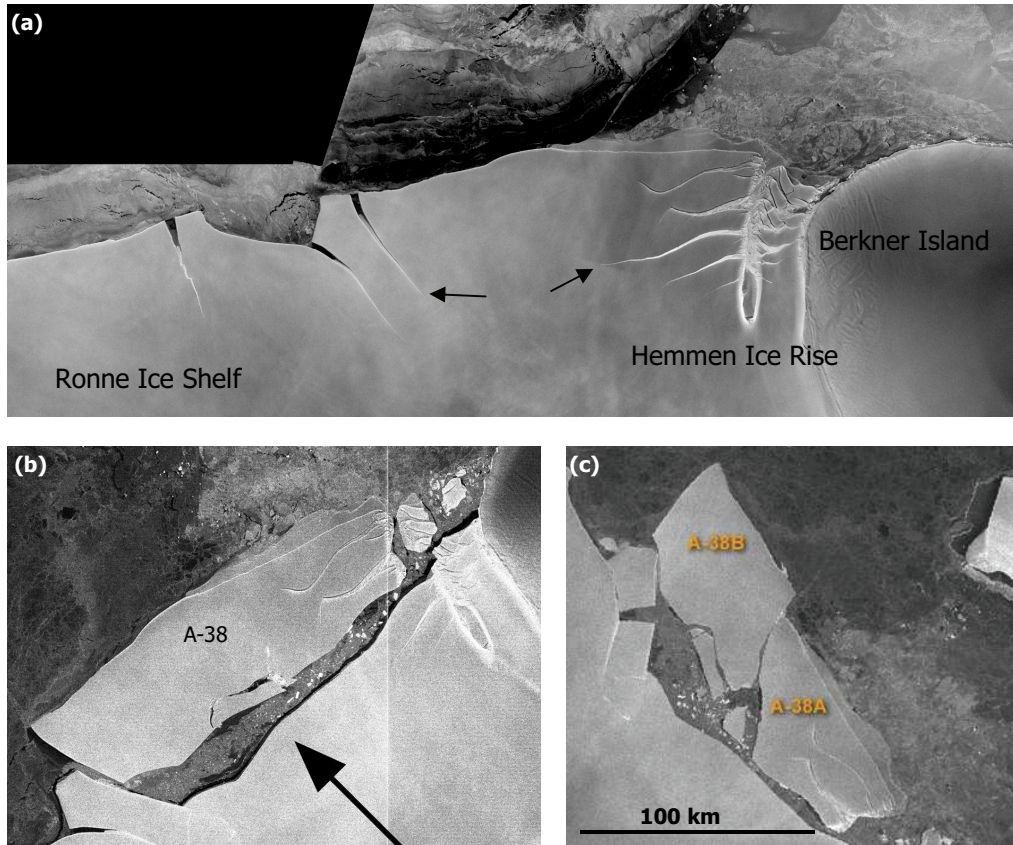


**Figure 1.3:** Iceberg from the Filchner-Ronne-Ice Shelf

In October 1998, the giant tabular iceberg A-38 calved from the Ronne-Ice Shelf west of Berkner Island. **(a):** The crack which led to this calving event followed the connecting line between two inlet tips, indicated by the arrows. **(b):** The tabular iceberg had an approximate size of  $150 \text{ km} \times 50 \text{ km}$  and was first detected on 15 October 1998 by satellite imagery. **(c):** Following a collision with the ice shelf front shortly after calving, A-38 broke into two halves of about equal size: A-38A, formerly the eastern part, still containing two major inlets of 40 km length, and A-38B, the western part, on which this study is focused. Image courtesy: Canadian Space Agency RADARSAT 1997/98.

## 1.2 Processes governing tabular iceberg evolution

Considering a typical lifecycle of a large tabular iceberg from calving to final decay, the iceberg is subject to various influencing factors affecting different aspects of its evolution.

The drift of a tabular iceberg is determined by the driving forces of ocean currents and wind, but also by the surrounding sea ice conditions. The latter become the governing driving force when the sea ice concentration reaches 90 % due to the fact that a closed sea ice cover collects wind momentum over a huge area (*Lichey and Hellmer, 2001*). Thus, the drift velocity of a tabular iceberg is subject to strong variations depending on current, wind and sea ice cover.

The drift paths of large icebergs are tracked by analysing satellite image sequences gathered with various sensors (e.g., *Ballantyne, 2002*), from which is evident that most icebergs follow similar pathways (Fig. 1.4). Icebergs originating at the Filchner Ronne Ice Self usually follow the Weddell Gyre towards the Antarctic Peninsula and then drift north along the coastline. Reaching the tip of the peninsula and the boundary of the sea ice cover, some icebergs drift further north towards South Georgia Island or to the South Sandwich Islands. Other icebergs stay within the Gyre and return eastwards (*Schodlok et al., 2006*). Icebergs from the Ross Ice Shelf drift eastwards within the Antarctic circumpolar current or follow the Antarctic coastal current, which is directed westwards and restricted to a narrow channel close to the coast of Antarctica.

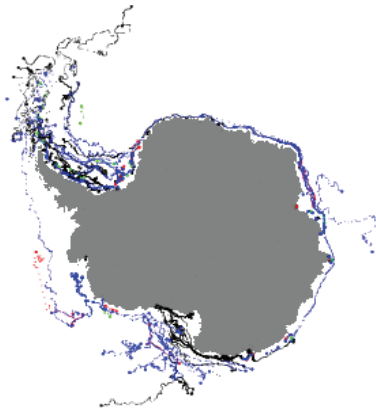


**Figure 1.4:** Drift routes of Antarctic tabular icebergs (1978 and 1992-2004, Antarctic Iceberg tracking database, Brigham Young University, Provo, Utah, USA)

The drift path and the associated environmental conditions such as ocean and air temperature have a major impact on the stability of tabular icebergs. Grounded shortly after calving near to the ice shelf they may endure decades without any signs of decay, as could be observed in the case of the Filchner icebergs A-22 and A-23. In contrast, icebergs grounded in the vicinity of South Georgia Island, which is located at the latitude of  $54.5^{\circ}$  S survive for one year at most until their final decay.

The shape of large tabular icebergs does not change significantly

during long periods of their drift. Small scale calving at the margins due to wave erosion and lateral melting only affects a small proportion of the entire

iceberg. Considering an idealized rectangular tabular iceberg with side lengths of 30 and 50 km and a thickness of 200 m, the iceberg's sides, which are subject to calving, comprise a boundary surface of 32 km<sup>2</sup>, whereas the basal boundary surface amounts 1500 km<sup>2</sup>. Thus, the most effective erosion process occurs at the iceberg's base due to basal melting, which causes continuous thinning of the iceberg and leads to the release of cold freshwater into the ocean. This process may influence the stability of the water column and effect water mass formation (*Gladstone et al.*, 2001). Surface melting also plays a role in iceberg erosion, at least when the iceberg reaches latitudes where the air temperature stays above the freezing point for longer periods. If the iceberg surface becomes impermeable due to percolating and refreezing melt water in the upper firn layer of the iceberg, the formation of melt ponds may occur, as has been observed for the iceberg A-43B (*Scambos et al.*, 2005).

A further process contributing to continuous iceberg deformation is the strain thinning associated with ice-shelf-like spreading of the iceberg. The degree of such spreading, which is driven by the stress imbalance at the ice front and gradients in the ice thickness distribution, depends on the temperature regime within the ice body and the iceberg geometry.

Singular events such as collisions or grounding on shallow continental shelves may also have a major influence on tabular iceberg evolution. The iceberg A-38 collided shortly after its calving with the Ronne Ice Shelf edge, which lead to the splitting of the iceberg into two parts and the calving of another iceberg from the ice shelf (fig 1.3). Grounding events are not necessarily connected with iceberg fracturing, but represent a significant perturbation in the local bathymetric settings and may initiate changes in the circulation regime (*Grosfeld et al.*, 2001) as well as in the local sea ice conditions (*Massom,2001; Massom et al.,2003; Martin et al.*, 2007).

### 1.3 Objectives

The aim of this study was to investigate and quantify the role of the various processes influencing tabular iceberg evolution and their impact on the surrounding system. Reflecting the different nature of the processes investigated, this thesis is subdivided into three parts, each concentrating on a particular aspect of tabular iceberg evolution. part I and II are related to ice deformation and basal melting, respectively. Part III is related to seismic events, triggered by grounded and floating icebergs.

A question of special interest in the context of part I is whether drifting tabular icebergs can be regarded as a model for ice shelves under warming conditions, as has been proposed in recent publications (*Scambos et al.*, 2005; *MacAyeal et al.*, 2006). To evaluate whether there could be an

analogy, it is essential to understand the role of inherent ice dynamics for the tabular iceberg.

The amount of basal melting affects the stability of ice shelves and icebergs to a similar degree and this is addressed in part II of this study. Beside the consequences of thinning due to melting for the iceberg itself, more precise estimates of how much melting occurs in the different oceanographic regimes would contribute to a better understanding of the iceberg's impact on its surrounding system.

Finally, in part III, the grounding process of the iceberg A-38B was investigated by analysing the associated tremor events recorded at the HOPE seismic station, South Georgia. In search of comparable events attributed to other tabular icebergs the data analysis yielded another class of iceberg-generated tremor caused by floating icebergs, which is presented and discussed in the last part of the thesis.



## 2

# Publication synopsis

**2.1 Daniela Jansen, Henner Sandhäger, and Wolfgang Rack (2005). Model experiments on large tabular iceberg evolution: ablation and strain thinning.** *Journal of Glaciology*, 51(174), 363-372.

This paper describes the model for inherent iceberg dynamics and introduces the results of the first model applications. Several sensitivity runs were performed, systematically testing the flow velocity part separately from the temperature evolution and basal or surface erosion scenarios. Also, the first application to a real tabular iceberg (A-38B) is shown, modelling its evolution from the position in front of the ice shelf edge up to South Georgia Island. The emphasis in this part of the study was on ice dynamics, whereas the basal and surface mass balances were predetermined as external forcing parameters. We concluded that the strain thinning of tabular icebergs due to their inherent stress distribution is of minor importance in comparison to the expected magnitude of basal melting.

**2.1.2 Poster:** Daniela Jansen, Henner Sandhäger, W. Rack (2005). **Influence of inlets on tabular iceberg evolution.** *Geophysical research abstracts*, Vol. 7, 08174.

To complement this part of the thesis, further model studies were performed to investigate the influence of debris-filled inlets within tabular icebergs. The transition between the inlet filling and the iceberg was implemented *via* a modified boundary condition, leading to a gradual decoupling depending on filling temperature and thickness. The simulations revealed that the inlets have only minor effects on the inherent dynamics during drift, although satellite observations (MODIS) show that they influence the pattern of the final break-up.

**2.2 Daniela Jansen, Michael Schodlok, and Wolfgang Rack (2007). Basal melting of A-38B: A physical model constrained by satellite observations.** *Remote sensing of Environment*, 111(2-3), 195-203.

The second part of the thesis, which is presented in this publication, was focused on the basal melting process. We used ICESat altimetry data as a

method for monitoring the iceberg freeboard change during its drift. From a combination of satellite altimetry and the physical relations involved in basal melting it became obvious that tabular icebergs are subject to different melting regimes during their drift, depending on drift velocity and surrounding ocean currents. In case of A-38B the entire drift was separated into three melting regimes. As the iceberg drift in the Weddell Sea was influenced by sea ice motion and the shallow shelf region was subject to vigorous tidal mixing, the turbulent exchange between iceberg and ocean is relatively high in the first period of drift. When the iceberg enters the Scotia Sea and accelerates, the melting plume is probably transported along with the iceberg. Melting is again enhanced when the iceberg is grounded at South Georgia Island. These findings may contribute to a better estimation of the quantity and distribution of iceberg-related freshwater input into the Southern Ocean.

**2.3 Daniela Jansen, Christian Müller. Iceberg-generated tremor in the vicinity of South Georgia Island.** Submitted to Geophysical Journal International.

To investigate the grounding processes of tabular iceberg A-38B, we evaluated the seismic records from the HOPE seismic station on South Georgia Island from 1 December 2003 to 29 January 2004. The combination of MODIS data and ETOPO2 bathymetry of the island shelf enables classification of the tremor as ground collision events. Iceberg A-38B caused a high-energy tremor with diffuse spectral features when it first collided with the steeply rising sea floor near to the coast of South Georgia Island. Evaluation of seismic data recorded during a second time frame from 1 December 2002 to 31 March 2003 revealed tremor events generated by a floating iceberg. Harmonic tremor occurred when A-43G, a Ronne Ice Shelf iceberg containing a major rift structure, was caught in an eddy at the Southern Antarctic Circumpolar Current Front (SACCF) in the northwest of South Georgia. The characteristic signature of either grounding iceberg or floating iceberg events indicates, that the excitation mechanisms of these oscillations are of a different nature.

# 3

## Ice flow and thermodynamic model

Similar to the behaviour of ice shelves, tabular icebergs spread under their own weight under the influence of gravity. The driving forces for the ice flow result from the imbalance of lithostatic pressure inside the ice body and the hydrostatic pressure at the ice edge as well as the thickness gradient of the iceberg. As the friction at the ice-ocean boundary and therefore vertical shear can be neglected, the pressure difference induces longitudinal stresses which lead to a thinning of the ice body towards the ice edge (*Paterson, 1994*).

The spreading process of ice shelves and icebergs is subject to the same physical relations. The flow of ice shelves, however, is controlled by external conditions such as the coupling to the solid earth at the grounding line or ice rumples and the coastline, and also by inflow velocities of feeding glaciers or ice streams (*Sandhäger, 2000*). In this respect, a tabular iceberg represents the simplest form of a floating ice body with a large horizontal extension relative to its vertical dimension. In other words, the iceberg can be regarded as a small ice shelf surrounded by a calving front.

The inherent dynamics of ice shelves have been subject to numerous model studies, focussing in recent years on the processes at the grounding line or the impact of shear zones and variable ice rheology. However, little is known about the role of strain thinning for the simple geometry of a tabular iceberg or to what extent the overall thickness change during drift can be explained by this process. The iceberg draft is an essential parameter for simulating iceberg drift, in which strain thinning has been neglected so far (*Schodlok et al., 2006; Lichey and Hellmer, 2001*). Numerical simulations of iceberg spreading can either support this approximation or deliver guide values of strain rates which can be implemented in drift models. These simulations would also provide information about the stress distribution within an iceberg and reveal whether the final decay might be induced by particular stress regimes.

Another important factor regarding iceberg stability is the temperature profile. Erosion of the warmer parts near to the ice-ocean interface could lead to a decrease in the mean temperature, which changes the rheological properties of the ice body. Thus, a thermodynamic model approach

simulating the evolution of the ice temperature with respect to changing surface temperatures and surface and basal erosion is also necessary.

As the governing principles of ice flow are the same for tabular icebergs as those implemented in ice shelf models, an existing model (*Grosfeld and Sandhäger, 2004*) was adapted in this study to investigate the role of inherent ice dynamics and thermodynamics in tabular iceberg evolution (Publication I). A first series of numerical experiments with idealized icebergs of constant density and temperature was performed to test the main modules of the iceberg model and to gain insight into the characteristic ice dynamics. A second series of model studies included the impact of ocean and atmosphere as well as variable density and temperature distributions within geometrically idealized icebergs. Finally, the model was applied to the geometry of the tabular iceberg A-38B, which calved from the Ronne Ice Shelf in 1998, to simulate its evolution during its 5-year drift from the ice shelf edge to South Georgia Island.

### **3.1 Fundamental principles of ice dynamics in ice shelves and icebergs**

On a microscopic scale the deformation of polycrystalline ice can be described as a combination of moving dislocations within the single crystals and also crystals moving relative to each other, crystal growth, recrystallization or migration of crystal boundaries (e. g. *Paterson, 1994*). However, to describe the behaviour of large natural ice bodies, the ice is usually treated as a continuum, whose response under stress is determined by a single constitutive relation (*van der Veen and Payne, 2004*). The precondition for applying the physical relations for continuum mechanical problems (a small volume element of the relevant ice body is large enough that macroscopic parameters like density and stress may be defined, but also small enough to be regarded as an infinitesimal element (e. g. *Stephani and Kluge, 1995*)) are met for large ice bodies like ice shelves and icebergs.

In the following the fundamental principles of ice flow are introduced and the deduction of the iceberg model equations from these will be explained. The equations apply to a polycrystalline ice body within a Cartesian coordinate system with  $x$  and  $y$  axis parallel to the earth's surface (curvature of the earth can be neglected) and a  $z$  axis with the positive direction pointing upward and its origin at sea level. The iceberg freeboard is called  $h$  and the total ice thickness  $H$ . The horizontal components of the flow velocity vector are  $u$  and  $v$  and the vertical velocity component  $w$ .

**Balance of forces:**

The flow of ice in the stage of secondary creep can be described by the Stokes equation, i.e. the inertial forces acting on the ice can be neglected due to the dominating viscous forces. The only body force acting on the ice to be regarded is gravitation, and the balance of forces reduces to

$$\vec{\nabla} \cdot \boldsymbol{\sigma} = \rho(z) \cdot \vec{g} \quad (3.1)$$

with  $\boldsymbol{\sigma}$  as the stress tensor and  $\vec{g} = (0, 0, -g_z)$  as the gravitational acceleration with  $g_z = 9.81 \text{ ms}^{-2}$ . The lithostatic pressure, which is the first invariant of the stress tensor,  $P = \frac{1}{3} \cdot (\sigma_{xx} + \sigma_{yy} + \sigma_{zz})$ , does not contribute to deformation within the ice body. The stress tensor is therefore replaced by the deviatoric stress tensor  $\boldsymbol{\tau}$  with  $\tau_{ii} = \sigma_{ii} - P$  and  $\tau_{ij} = \sigma_{ij}$ , with  $i, j \in (x, y, z)$ .

**Conservation of mass :**

The general formulation of mass conservation for a volume element in its differential form is

$$\frac{\partial \rho}{\partial t} + \vec{\nabla} \cdot (\rho \cdot \vec{u}) = 0 \quad (3.2)$$

As the density of the ice body is prescribed by an equation of state established for the Ronne Ice Shelf (*Sandhäger et al.* 2004), and the influence of firn compaction is neglected, the mass balance can be calculated independent of temporal density changes (*Grosfeld and Sandhäger*, 2004) and reduces to:

$$\vec{\nabla} \cdot (\rho \cdot \vec{u}) = 0 \quad (3.3)$$

**Conservation of heat:**

The heat balance equation expresses the temperature change with time as a consequence of heat transfer due to heat conduction and advection, and due to inner heat production resulting from deformation of the ice (e. g. *Sandhäger*, 2000):

$$\rho c_p \cdot \frac{\partial T}{\partial t} = \vec{\nabla} \cdot (k \cdot (\vec{\nabla} \cdot T)) - \rho c_p \cdot \vec{u} \cdot (\vec{\nabla} \cdot T) + \delta H_i \quad (3.4)$$

where  $T$  is the ice temperature,  $c_p$  is the specific heat capacity,  $k$  the thermal conductivity, and  $H_i$  the inner heat production due to deformation of the ice. However, for the special case of temperature evolution in an ice shelf or an iceberg, several assumptions simplify this relation significantly (*Sandhäger*, 2000; *Paterson*, 1994):

The thermal conductivity  $k$  depends only on the temperature, the dependence on ice density may be neglected when regarding large ice

bodies. For consolidated ice,  $k$  can be approximated by the empirical relation (Huybrechts, 1992)

$$k = 9.828 \frac{\text{W}}{\text{mK}} \cdot \exp(-5.7 \cdot 10^{-3} \cdot T \text{ K}^{-1}) \quad (3.5)$$

Heat conduction in the horizontal plane can be neglected, as the horizontal temperature gradients are very small in comparison to the vertical gradients. For the same reasons the gradient of the thermal conductivity is only significant in the vertical direction. Thus, equation (3.4) reduces to

$$\rho c_p \cdot \frac{\partial T}{\partial t} = \frac{\partial k}{\partial T} \cdot \left( \frac{\partial T}{\partial z} \right)^2 + k \cdot \frac{\partial^2 T}{\partial z^2} - \rho c_p \cdot \bar{u}(\bar{\nabla} \cdot T) + \delta H_i \quad (3.6)$$

### Constitutional relation:

The so called flow law describes the viscous-plastic behaviour of polycrystalline ice under load. A commonly used relation was found by Glen in 1955 and is valid for a stress interval between 50 kPa and 200 kPa which represents the stresses associated with deformation of glaciers and other natural ice masses (Paterson, 1994).

Glen's flow law relates the rate of deformation of the ice with the applied load:

$$\dot{\epsilon}_{ij} = A \cdot \tau^{n-1} \tau_{ij} \quad (3.7)$$

where  $\tau$  is the so called effective stress, representing the second invariant of the stress tensor:  $2 \cdot \tau^2 = \tau_{xx}^2 + \tau_{yy}^2 + \tau_{zz}^2 + 2 \cdot (\tau_{xy}^2)$ .

The deformation rate, a tensor which describes the amount of deformation of an ice body over time, is defined as follows:

$$\dot{\epsilon}_{ij} = \frac{1}{2} \cdot \left( \frac{\partial u_i}{\partial x_j} + \frac{\partial u_j}{\partial x_i} \right), \quad (3.8)$$

with  $u_i$  being components of the flow velocity vector and  $i, j \in (x, y, z)$ .

As equation (3.7) is also valid for the tensor invariants, it can be expressed in the following way, with an effective deformation rate  $\dot{\epsilon}$  analogous to  $\tau$ :

$$\dot{\epsilon}_{ij} = A^n \cdot \dot{\epsilon}^{1-\frac{1}{n}} \cdot \tau_{ij} \quad (3.9)$$

The constant is set to 3 in this study, in agreement with other model studies and some laboratory measurements (Alley, 1992; Huybrechts, 1992; Paterson, 1994).  $A$  is called the flow or rate factor and represents the influence of temperature on the flow of ice. It is given by the Arrhenius relation:

$$A = m \cdot A_0 \cdot \exp\left(-\frac{Q}{R \cdot T^*}\right), \quad (3.10)$$

with an enhancement factor  $m$ , which is set to 1 in this study, the gas constant  $R = 8.314 \text{ J mol}^{-1} \text{ K}^{-1}$ , and the *in situ* melting temperature  $T^* = 0.00087 \text{ K m}^{-1} \cdot (h - z)$  (Sandhäger, 2000).  $Q$  is the activation energy required for deformation and was determined empirically, as was  $A_0$ , which represents the influence of ice structure and composition. We oriented at the numbers recommended by Paterson and applied two different values which depend on a temperature threshold (Publication I).

### Ice shelf approximation:

In contrast to grounded ice, the impact of friction at the base of a floating ice body can be neglected, leading to the assumption that the vertical shear stress is zero:  $\tau_{xz} = \tau_{yz} = 0$ . Thus, the ice body is in hydrostatic equilibrium with depth-invariant horizontal flow velocities. This leads to significant simplifications of the equations of ice flow.

## 3.2 Diagnostic model equations: ice shelf velocities

Combining the ice shelf approximation, the continuum-mechanical balance equations for momentum and mass and the constitutional relation yields the model equations for the horizontal flow velocities of floating ice bodies. After integration over the vertical column, the equations read (e.g., MacAyeal *et al.*, 1986):

$$2 \frac{\partial}{\partial x} (F \dot{\epsilon}_{xx}) + \frac{\partial}{\partial x} (F \dot{\epsilon}_{yy}) + \frac{\partial}{\partial y} (F \dot{\epsilon}_{xy}) = \bar{\rho} g H \frac{\partial(h-H)}{\partial x} + g \frac{\partial}{\partial x} \left( \int_{h-H}^h \int_z^h \rho dz' dz'' \right) \quad (3.11)$$

$$2 \frac{\partial}{\partial y} (F \dot{\epsilon}_{yy}) + \frac{\partial}{\partial y} (F \dot{\epsilon}_{xx}) + \frac{\partial}{\partial x} (F \dot{\epsilon}_{xy}) = \bar{\rho} g H \frac{\partial(h-H)}{\partial y} + g \frac{\partial}{\partial y} \left( \int_{h-H}^h \int_z^h \rho dz' dz'' \right) \quad (3.12)$$

$$F = H A \bar{\epsilon}^{-\frac{1}{n}} \dot{\epsilon}^{\frac{1}{n}-1},$$

The bar indicates the depth averaged value of the respective parameter. The vertical component of the flow velocity is a direct consequence of the conservation of mass:

$$\rho w = (\dot{\epsilon}_{xx} + \dot{\epsilon}_{yy}) \int_z^h \rho dz' + u \frac{\partial}{\partial x} \left( \int_z^h \rho dz' \right) + v \frac{\partial}{\partial y} \left( \int_z^h \rho dz' \right) + \frac{\partial}{\partial t} \left( \int_z^h \rho dz' \right) - \rho_c a_s, \quad (3.13)$$

where  $\rho_c$  represents the density of completely consolidated ice ( $915 \text{ kg m}^{-3}$ ),  $a_s$  the surface accumulation rate measured in  $\text{m a}^{-1}$  ice equivalent, and  $t$  the time. The equation has been integrated over the vertical column, as the horizontal velocities are depth invariant.

### Boundary conditions at the ice edge

The boundary condition required for the flow velocity at the ice edge (fig. 3.1) is based on the balance of forces formulated for an idealized geometry (Weertman, 1957).

$$H \int_{h-H}^h \sigma_{xx} dz = H \int_{h-H}^0 P_w dz \quad (3.14)$$

$$\Leftrightarrow H \int_{h-H}^h \left( 2\tau_{xx} + \tau_{yy} - g \int_z^h \rho dz' \right) dz = H \int_{h-H}^0 g \cdot \rho_w \cdot z dz, \quad (3.15)$$

where  $P_w$  represents the hydrostatic pressure. If the ice flow takes place in the  $x$ -direction, perpendicular to the iceberg front, the condition reads after replacing  $\tau_{xx}$  and  $\tau_{yy}$  by equation (3.8) and (3.9):

$$\frac{\partial u}{\partial x} = A^{-\frac{1}{n}} \dot{\epsilon}^{1-\frac{1}{n}} \frac{g}{2H} \left( \int_{h-H}^h \int_z^h \rho dz' dz - \rho_w \frac{(h-H)^2}{2} \right) - \frac{1}{2} \frac{\partial v}{\partial y}, \quad (3.16)$$

where  $\rho_w$  is the density of sea water. As there is no transfer of shear forces at the ice shelf edge, no shear deformation is possible:

$$\dot{\epsilon}_{xy} = 0 \quad \text{or} \quad \frac{\partial v}{\partial x} = -\frac{\partial u}{\partial y}$$

This boundary condition is valid along the entire iceberg front, which is different to the conditions for ice shelves, where there is a coupling to the solid ground and to the inner ice sheet. The ice front boundary condition alone is not unique; each velocity field with rigid body rotations and a translation superimposed onto the velocity of ice flow is still a solution of the model equations. However, the superimposed velocity fields lead to spurious contributions to the advection in calculating temperature distribution or to the calculated thickness evolution and may even cause divergences in the numerical solution of the model equations. Therefore, the iceberg dynamic model has to be adapted by reducing these superimposed fields instantaneously by the constraint of minimal kinetic energy.

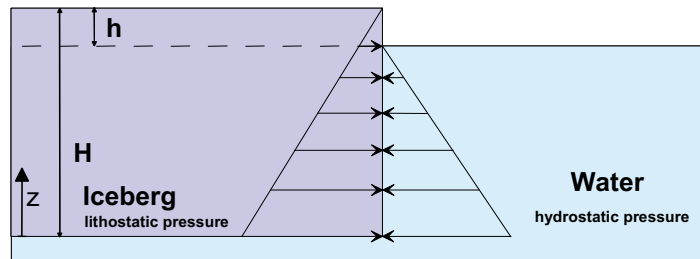


**Figure 3.1:** Imbalance of hydrostatic and lithostatic pressure at the iceberg margin. The arrow indicates the positive  $z$ -direction. The origin of the  $z$ -axis is located at the sea level.

### Boundary condition for debris filled inlets

For the edges of ice debris-filled inlets, as for example in iceberg A-38A, the boundary has to be modified (fig. 3.2). These features are formed in the pre-calving stage and filled by a mixture of sea ice, snow and debris from the iceberg margins (*Rignot et al.*, 1998; *MacAyeal et al.*, 1998). To compute their influence on the velocity field and stress distribution of the iceberg, the inlet filling itself is treated as a layer of consolidated ice, which can transmit longitudinal stresses, but no horizontal shear. This leads to a modified balance of forces at the inlet edge, where part of the freeboard imbalance is absorbed by the filling. The extended boundary condition now reads:

$$\int_{h-H}^h \left( 2\tau_{xx} + \tau_{yy} - g \int_z^h \rho dz' \right) dz - \int_{\hat{h}-\hat{H}}^{\hat{h}} \left( 2\hat{\tau}_{xx} + \hat{\tau}_{yy} - g \int_z^{\hat{h}} \hat{\rho} dz' \right) dz - \int_{h-H}^{\hat{h}-\hat{H}} g \rho_w z dz = 0 \quad (3.17)$$

The numerical implementation of this boundary condition is only appropriate for  $\frac{\hat{H}}{H} \ll 1$ . The ‘^’ indicates the parameters associated with the debris filled inlets.

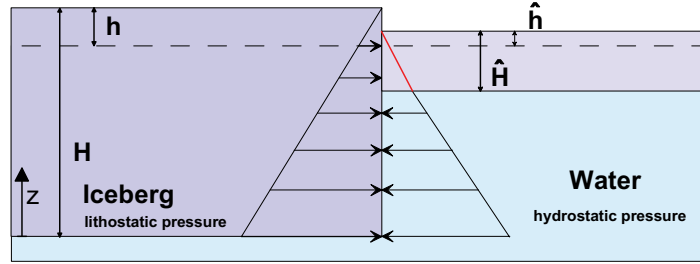


**Figure 3.2:** The imbalance at the iceberg margin is modified by a layer of ice debris. The arrow indicates the positive z-direction. The origin of the z-axis is located at the sea level.

### 3.3 Prognostic model equations: Temperature and ice thickness

To calculate the temporal evolution of an ice body in response to time-dependent boundary conditions, prognostic model equations are required. The change of temperature within time can be calculated by using the simplified heat balance equation (3.6). The boundary conditions for the ice temperature are the time-dependent prescribed temperature of the surface layer, which is set to the surface melting point ( $0^\circ$ ) if the air temperature is positive, and the basal layer temperature which is kept at  $-2^\circ\text{C}$  as an

approximation for the pressure melting point of sea water at the depth of the iceberg draft (Publication I).

The basic equation for calculating the evolution of iceberg geometry is the vertically integrated mass balance equation which describes the temporal change in ice thickness (e.g. *Paterson, 1994*):

$$\frac{\partial H}{\partial t} = \frac{\rho_c}{\bar{\rho}} (a_s + a_b) - \frac{1}{\bar{\rho}} \left( \frac{\partial}{\partial x} (\bar{\rho} H u) + \frac{\partial}{\partial y} (\bar{\rho} H v) \right), \quad (3.16)$$

where  $\bar{\rho}$  is the depth-averaged density and  $a_b$  and  $a_s$  the basal and surface mass balance measured in  $\text{m a}^{-1}$  ice equivalent. Iceberg thickness evolution is accompanied by surface elevation changes according to the hydrostatic relation  $h = (1 - \bar{\rho} / \rho_w) H$ , where  $\rho_w$  is the density of sea water.

### Required input parameters

As this study is focussed on icebergs from the Ronne Ice Shelf, the Filchner Ronne Ice Shelf thickness map (*Sandhäger et al., 2004*) was consulted as a data source for the **initial ice thickness  $H$**  of iceberg A-38A and A-38B. This map represents a compilation of several ground-based and airborne radar echo sounding (RES) data sets. The iceberg was cut out of the grid by means of calving line determination by satellite imagery.

The Atlas of Antarctica (*Herzfeld, 2004*) provided a further data source. This is a compilation of satellite altimetry data from the sensor mounted on ERS-1 between 1991 and 1996 and therefore provides ice shelf elevations during the period shortly before the calving of iceberg A-38B in 1998. This data set proved to be more realistic in representing the downward slope at the ice shelf edge.

As a boundary condition for the calculation of the temperature profile, the **surface temperature  $T_s$**  of the iceberg must also be prescribed, and is set equal to the air temperature if it is below zero degrees. For higher temperatures  $T_s$  is set to  $0^\circ\text{C}$ . ECMWF (European Centre for Medium-Range Weather Forecasts) model data provide a possible source of surface temperatures for simulations of real icebergs (Publication I).

**Surface and basal mass balances** must be prescribed in  $\text{m}_{\text{ice-equivalent}}$ . Surface mass balance can be calculated by means of the Positive Degree Day model on the basis of the surface temperature (*Braithwaite and Olesen, 1989*). Estimations of basal mass balance for the first model application on a real tabular iceberg were based on a model study of the tabular iceberg C-7, which took a similar drift route (*Schodlok et al., 2005*). This melt rates are predominately determined by the latitude of the iceberg's position.

### 3.4 Numerical solution

As described in *Grosfeld and Sandhäger (2004)*, the model grid is composed of block-centred cells. In the x-y plane, which is defined as the plane parallel to the geoid, the cells have an area of  $\Delta x \cdot \Delta y$ . The vertical coordinate  $z$  is transformed into a new coordinate  $\zeta$  by scaling with the total ice thickness  $H$  (*Sandhäger, 2000*):

$$\zeta = \frac{z - (h(x, y) - H(x, y))}{H(x, y)} \quad (3.17)$$

This leads to a vertical model domain  $0 \leq \zeta \leq 1$  independent of the position in the horizontal plane. The grid is divided into ten layers in the vertical, with a height of cells varying between 0.02 and 0.1  $H$ . In the horizontal plane it can be adapted individually to the investigated iceberg.

The model equations for the horizontal flow velocities are solved by a finite difference approach, which is based upon the simple approximation of derivations by differential quotients analogous to Taylor series expansion. A relaxation procedure introduced by *Herterich (1987)* is then applied to calculate iteratively the solution for the horizontal velocities. The temperature evolution as well as the evolution of ice thickness are calculated explicitly in the next step. Due to the different time scales of significant changes of these two processes, the time step for the temperature evolution is a quarter of the geometry evolution time step, following the Courant-Lewy Criterion.

A detailed description of the numerical implementation and the model grid is given in *Grosfeld and Sandhäger (2004)*.



# 4

## Basal melting of tabular icebergs

Antarctic tabular icebergs represent a freshwater source for the Southern Ocean exceeding even the amount of freshwater from ice shelf basal melting (Jacobs *et al.*, 1992). Since tabular icebergs tend to follow certain drift routes (e.g. Schodlok *et al.*, 2006), their melt is not distributed equally across the ocean. However, the relation between the intensity of melting and drift conditions is not yet well understood. To quantify the effects of iceberg melting on water mass formation in the Weddell Sea it is essential to know how much freshwater is exported by icebergs to the Scotia Sea and beyond. The second part of this thesis is therefore focused on the basal melting processes of tabular icebergs.

The disintegration and melting of smaller icebergs, being a severe threat to shipping routes (e.g., Kozian 1994), has been subject to several observational and numerical model studies (Venkatesh 1986; El-Tahan *et al.*, 1987; Robe *et al.*, 1977). Wave erosion, side wall melting and calving are the most significant mechanisms of deterioration of these irregular shaped chunks of floating ice. Tabular icebergs also show these forms of erosion, but compared to their entire mass the loss at the edges is small. Satellite remote sensing data documents that the shape of tabular icebergs does not change significantly during long periods of drift (Scambos *et al.*, 2005). The main mass loss occurs at the basal boundary by melt water release into the ocean.

The thermodynamic processes beneath a tabular iceberg with a length scale of about ten kilometres resemble at first sight those occurring at ice shelf bases, which have been subject to many model studies (Hellmer and Olbers, 1989; Jenkins, 1991; Gerdes *et al.*, 1999), aiming to shed light on the physical processes in ice shelf caverns. As the water column beneath the ice shelf is only studied at few places by means of drilling through the ice (Nicholls and Østerhus, 2004), numerical modelling is a key tool for investigating the circulation pattern and the formation of the cold, low saline Ice Shelf Water (ISW), its abundance, and its impact on the Southern Ocean (Hellmer, 2004).

The driving forces of ice shelf cavern circulation models are the heat and freshwater fluxes connected to melting and freezing processes at the ice ocean interface. The pressure dependence of the freezing temperature leads

to melting at the grounding line of the ice shelf and accumulation of marine ice layers towards the ice shelf edge, inducing a mainly two dimensional circulation known as “ice pump” (*Lewis and Perkin, 1986*). Near to the grounding line, tidal mixing may also contribute to melt water production and is assumed to be a trigger of the convective circulation (*MacAyeal, 1985*).

In contrast to the ice shelf case, the circulation pattern underneath a tabular iceberg is not well understood. The ice pump is induced by the pressure dependence of the freezing point of sea water, and the usual draft difference of a tabular iceberg is small compared to the difference between an ice shelf and the calving front. This indicates that the circulation at the iceberg base is not governed by thermohaline convection. Additionally, the water beneath an iceberg is not encased in a cavern and a stable convection cell is not likely to develop. Hence it is not straight forward to apply a coupled thermodynamic and circulation model to the tabular iceberg case.

However, following the parameterisation of the thermodynamic processes in ice shelf models, given below (e.g. *Holland and Jenkins, 1999*), it becomes obvious that knowledge about the current velocities at the iceberg ocean interface is required to calculate the melt rate. The latter is determined by the amount of turbulent exchange between the melt water plume and the surrounding ocean. In this study we aim to combine the information available from satellite-borne sensors for large icebergs with the more detailed ocean state information offered by modelling, to yield more precise estimates of how much melting occurs in the different oceanographic regimes transited by drifting icebergs (Publication II).

## 4.1 A thermodynamic model for the ice ocean interaction

The processes at the ice ocean interface are constrained by three physical boundary conditions: Heat and salt must be conserved and as the ice ocean interface is a boundary between two phases of the same material, the temperature at the interface must be at the in situ freezing point. The latter is only valid under the assumption that the process of adjustment is sufficiently rapid (e. g. *Williams et al., 1998*).

To parameterise the processes at the iceberg-ocean-boundary we referred to a thermodynamic approach presented by *Hellmer and Olbers (1989)*. The constraints given above lead to three equations. The heat balance represents the turbulent heat exchange across the interface, consumed by melting and the conductive heat flow through the ice:

$$\rho \cdot c_{pw} \cdot \gamma \cdot (T_b - T_w) = \rho_i \cdot L \cdot \dot{h} - \rho_i \cdot c_{pi} \cdot \Delta T \cdot \dot{h} \quad (4.1)$$

where  $\rho$  and  $\rho_i$  are the density of sea water and ice,  $c_{pw}$  and  $c_{pi}$  the heat capacity of seawater and ice,  $L$  the latent heat of fusion.  $\Delta T$  represents the temperature gradient within the ice near to the boundary. *Hellmer and Olbers* (1989) assumed a linear temperature gradient within the ice. This might lead to an underestimation of the steeper temperature gradient at the iceberg base, but the conductive part of the heat transport is small (2 orders of magnitude) in comparison to the absorption of latent heat due to melting. The balance of salt quantifies the dilution caused by the iceberg melt water:

$$\rho \cdot \gamma_s \cdot (S_b - S_w) = \rho_i \cdot S_b \cdot \dot{h} \quad (4.2)$$

where  $\gamma_T$  and  $\gamma_S$  are assumed to be related linearly:  $\gamma_T = 0.00505 \cdot \gamma_S$ .

The third equation is the linearised relation (*Foldvik and Kvinge*, 1974) of the in situ freezing temperature at the iceberg base to salinity and pressure  $p$ :

$$T_b = a - b \cdot S_b + c \cdot p \quad (4.3)$$

with the constants  $a = -0.057$  °C,  $b = 0.0939$  °C and  $c = -7.64 \cdot 10^{-2}$  °C MPa<sup>-1</sup>.

## 4.2 The turbulent exchange velocity at the ice ocean boundary

The transport of heat across the iceberg-ocean interface is parameterised by the turbulent exchange velocity  $\gamma_T$ . Assuming a hydraulically smooth boundary, this parameter can be expressed as (*Kader and Yaglom*, 1972)

$$\gamma_T = \frac{u_*}{2.12 \cdot \ln\left(\frac{u_* \cdot l}{\nu}\right) + 12.5 \cdot \text{Pr}^{\frac{2}{3}} - 9}, \quad (4.4)$$

where Pr represents the molecular Prandtl number of sea water,  $l$  the length scale of mixing and  $u_*$  the so called friction velocity. The latter, which is defined in terms of the shear stress at the ice-ocean boundary, depends on a dimensionless drag coefficient  $c_D$  and the current velocity in the boundary layer  $u$ :

$$u_*^2 = c_D \cdot u^2 \quad (4.5)$$

The values for the exchange velocity deployed in ice shelf cavity models vary widely (*Holland and Jenkins*, 1999), leading to significant differences in the corresponding melt rates. Furthermore, since a tabular iceberg experiences several drift regimes during its life cycle, the choice of a

constant value for the turbulent exchange for the entire drift would lead to considerable errors. The knowledge of the current velocity  $u$  in the boundary layer between iceberg and ocean is therefore essential to calculate realistic iceberg melt rates from salinity and temperature data of the boundary layer.

Modelled current velocities are not available at the required accuracy, because small-scale flow variations and, for example, eddies would have an influence on the erosion of the melt water plume. In the shallow shelf regions or especially for grounded icebergs the tidal currents must also be taken into account.

A possibility to compensate this lack of information is to refer to satellite altimetry data as a means of measuring the freeboard change of a tabular iceberg. The combination of iceberg altimetry profiles at different locations of the drift and the thermodynamic equations then yields an estimate of the amount of turbulent exchange between iceberg and ocean (Publication II).

### **4.3 Iceberg freeboard changes derived from ICESat altimetry**

The GLAS Instrument (Geoscience Laser Altimetry System) on ICESat (Ice, Cloud & Land Elevation Satellite) measures surface elevation averaged over a 60 m diameter footprint spaced at 172 m intervals along-track (Zwally *et al.*, 2002). The instrument was designed to monitor the mass balance of the large ice sheets in the first place, and is therefore on a pole to pole orbit, which yields highest coverage in the polar regions. The GLAS instrument measures the distance to the earth surface by emitting short Laser pulses and recording emitting and receiving time as well as the phase information (e.g. Schutz *et al.*, 2005). The distance from satellite to the earth surface can be calculated from the two way travel time of the laser pulse, the speed of light, the composition of the air column must be considered in form of an atmospheric correction. The laser pulses, which are part of the infrared and visible spectrum (1064 nm, 532 nm), are reflected not only by the earth surface but also by cloud cover, which leads to significant data gaps above the Southern Ocean and the coasts of Antarctica.

ICESat was launched in January 2003, but due to technical problems with one of the instrument's lasers and the high energy consumption data is only available for several selected observation periods, provided by the NSIDC (National Snow and Ice Data Center, Boulder, USA). The relevant time window for Iceberg A-38B comprises the campaigns 1, 2a and 2b, each containing one complete profile measurement of the iceberg A-38B (fig.4.1). At the acquisition time of the iceberg profiles, A-38B already left

the sea ice area behind. Thus, the sea level can be used as a reference height for the freeboard measurements.

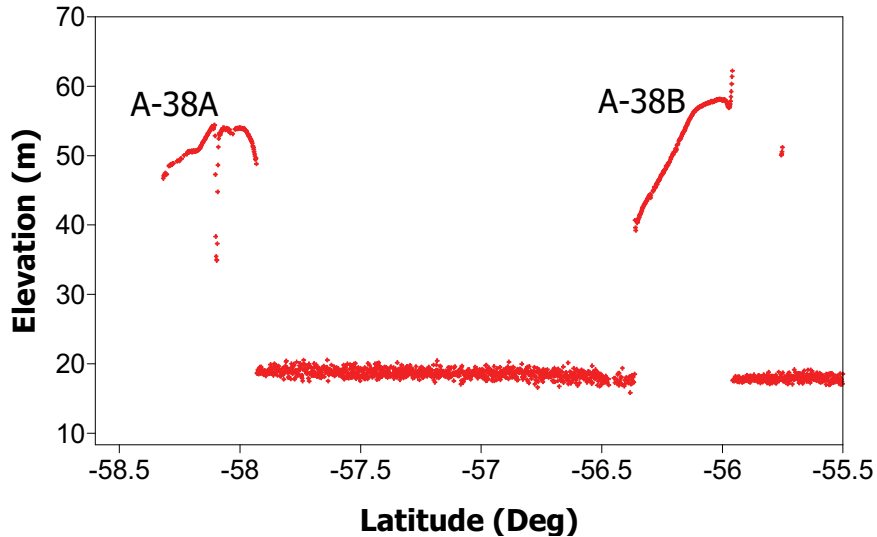


**Figure 4.1:** Raw ICESat data of an iceberg overpass on 31 October 2003 (Zwally *et al.*, 2003). Also the inlet of A-38A is resolved. In comparison to the ocean the iceberg A-38B has a very smooth surface.

MODIS images of the satellites Terra and Aqua recorded with a time difference of 4 hours were used to estimate the iceberg movement, which was then extrapolated to the ICESat acquisition time to determine the location of the profiles on the iceberg (fig. 4.2). This method of monitoring iceberg freeboard was also applied by *Scambos et al.* (2005), who investigated buoyancy driven deformation of the edges of tabular icebergs due to enhanced melting at the sea level.

The MODIS instrument is installed at the platforms Terra and Aqua, two identical satellites on a polar orbit which pass the same spot at the earth surface with a time difference of 4 hours. The instrument records spectral information of the light reflected from the earth surface by receiving the intensity in discrete bands of the electromagnetic spectrum (e.g. *Barnes et al.*, 1998). Two of the MODIS bands (620-670 nm; 841-876 nm) are imaged at a resolution of 250 m and therefore provide the possibility of documenting the icebergs motion in good resolution.

Additional to the MODIS images, ASTER (Advanced Spaceborne Emission and Reflection Radiometer, Resolution 25 m) data recorded during the grounding phase near South Georgia was analysed. The image resolves the small-scale calving events at the iceberg margins and shows a large number of small icebergs at the thinner side of A-38B, indicating an acceleration of decay, whereas very little calving occurs at the thicker iceberg edge (Publication II).

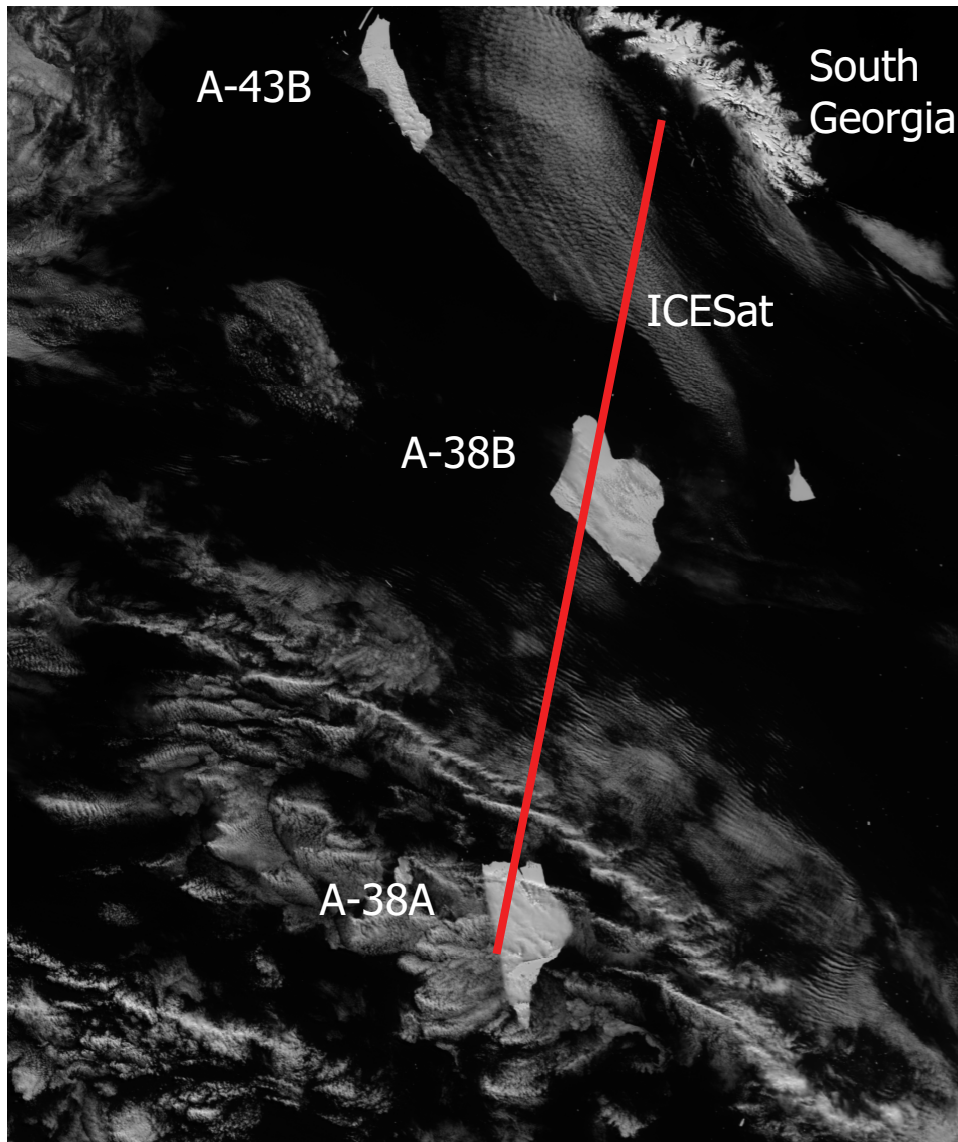


**Figure 4.2:** MODIS image of icebergs A-38A and A-38B south of South Georgia Island. The red line indicates the position of the ICESat profile shown in fig. 4.2. Image data: MODIS Rapid Response Team NASA/GFSC.

# 5

## Seismic events originated from tabular icebergs

Large tabular icebergs can be the source of seismic tremor, which has been recorded by hydrophones at long distances as T phases or by land-based seismometers as seismic waves converted from hydro-acoustic signals at the coastal slopes. The duration of iceberg tremor events ranges from seconds to hours or even days. The spectral signature shows a broad variety including monochromatic as well as harmonic signals with well defined overtones and tremor with diffuse spectral peaks. (*Talandier et al.*, 2006).

By evaluating hydroacoustic data from the Polynesian Seismic Network *Talandier et al.* (2002) first identified a tabular iceberg located in the Ross Sea as the source of tremor events. They attributed the signals, which showed spectral peaks in the range of 3 to 7 Hz, to the iceberg B-15B and proposed collisions or scraping along the sea floor as trigger for these events.

In records of land based seismometers iceberg-related tremor events were also found. *Müller et al.* (2005) presented harmonic tremor including chaotic phases recorded at the seismological network at Neumayer Base (Dronning Maud Land, Antarctica), which they attributed to the tabular iceberg B-9A. Stressing the analogy to volcanic tremor, they proposed that the flow of water through tunnels or crevasses could be the source of the signals, as fluid-flow through irregular channels with elastic walls can induce oscillation if a critical flow speed is reached (*Julian*, 1994; 2000).

To investigate the impact of swell-induced elastic oscillations on iceberg stability, *MacAyeal et al.* (2006) installed seismometers on several tabular icebergs originating from the Ross Ice Shelf. Regarding the lower part of the spectrum, their data showed that the dominant part of the seismic energy of an iceberg is concentrated between 0.01 and 0.1 Hz, which corresponds to the frequency range of ocean swell generated in the Pacific Ocean. They further suggested that ocean swell could be the reason for iceberg failure and initiation of their final decay.

To investigate the grounding process and the break up of the tabular iceberg A-38B north-east of South Georgia Island, records from the HOPE seismic station (King Edward Point) were evaluated in the final part of the iceberg evolution project. The iceberg movements and small-scale drift patterns,

including rotations, were monitored on a day to day basis using MODIS imagery. Together with ETOPO2v2 (NOAA NGDC, 2006) bathymetry this provided information about the time window in which the iceberg was in contact with the island slope. During the observation periods several seismic tremor events occurred, which could be attributed to the iceberg by 2-D particle motion analysis and were all related to collisions with the island slope. An investigation of the lower part of the spectrum in the seismic signals around the time of the failure yielded no indication of swell-induced fracture associated with a particular storm event.

To assess whether other tabular icebergs produce comparable tremor events, a second time period of seismic records was evaluated, comprising the arrival of iceberg A-43G at the island. Several tremor events occurred could be attributed to A-43G, although the iceberg had no ground contact at that time. These signals were probably induced by the flow of water through a major rift structure.

In the following a short introduction to the data processing and to the physical relationships involved in the excitation of iceberg generated tremor is given. Additionally, the response of a tabular iceberg to ocean swell is discussed.

## 5.1 Data and data processing

Seismic records from station HOPE (King Edward Point, South Georgia Island, 54.2836 S, 36.4879 W), located at the north coast of the island (Cumberland East Bay) were evaluated. The data from the stations broadband data stream was recorded with a sample rate of 40 Hz and was provided by the Iris/IDA network, IRIS GSN/University of California, San Diego.

This broadband signal was recorded with a Streckeisen STS-2 seismometer, which measures the ground motion velocity with three identical sensors, whose sensitivity axes are inclined against the vertical like the edges of a cube standing on its corner. These components are later transformed to a Cartesian coordinate system with east-west, north-south and vertical axes (Wielandt, 2002).

As the spectral signature of iceberg-generated tremor is very characteristic, the simplest method for identifying such events is to regard spectrograms of the recorded data. By means of the Matlab signal processing software, moving short-period Fourier transforms of the seismograms were calculated using a Hamming-window (Publication III).

To determine the back-azimuth of a signal, a 2-D particle motion analysis was performed. In the case of longitudinal polarized waves the ground motion is parallel to the signal back-azimuth. If the horizontal velocity components of the seismic record are plotted against each other and show a

linear correlation, the slope of the graph indicates the direction towards the signal source. In combination with MODIS imagery this leads to identification of tabular icebergs as the source of the tremors in most cases. However, during the harmonic tremor events, some parts of the signal showed elliptical polarization. In these cases the azimuth could usually be best determined at the beginning (first arrival) of the tremor. Before applying the particle motion analysis, the data was filtered by means of a butterworth bandpass with cut off frequencies at 2 and 19 Hz. The lower boundary should assure that ocean swell as well as atmospheric pressure disturbances do not affect the determination of the back-azimuth. Nevertheless, the entire frequency range is included in the spectrograms.

## 5.2. Grounded iceberg events: stick-slip induced tremor

At first sight, the seismic events correlated with iceberg grounding or scraping along the island slope resemble signals. The iceberg is coupled to the solid earth and the first shock is usually characterised by longitudinally-polarized P-waves. In the case of a sliding iceberg, horizontal polarised S-waves would be expected. However, a closer look at the spectrogram reveals iceberg tremor characteristics such as the gliding of frequency peaks or the background sound which is structured in frequency bands. This tremor is probably excited by the stick-slip movement of the iceberg relative to the island slope. Seismic signals related to stick-slip motion have been observed before in connection with basal sliding of temperate glaciers (*VanWormer and Berg, 1973; Weaver and Malone, 1979; Wolf and Davies, 1986, Danesi et al., 2007*). The spectra of the reported signals were characterized by monochromatic frequency peaks between 0.5 and 2 Hz.

The stick-slip phenomenon can be explained by changing friction regimes during a relative motion. When the driving force of the motion is strong enough to overcome the static friction, the ice body starts to slide and the accumulated shear stress is reduced. This leads to a decrease in driving force. When the force is too small to overcome the kinetic friction, the ice body stops, until the shear tension is again strong enough to overcome the static friction. The frequency of this cycle depends on the relative velocity between island slope and iceberg, as this velocity governs the rise of the shear tension, and the force component normal to the contact plane. Thus, the frequency drops when the iceberg moves more slowly or if the direction of motion changes towards the island slope. Upward frequency gliding would indicate an acceleration of the iceberg or a change of the drift direction away from the island.

On a large scale, the stick-slip phenomenon is comparable to the movement between the crustal plates at transform faults, on a very small scale to the bowing of a violin string (*Fletcher, 2001*). In the latter case the stick-slip

process excites the natural frequency of the string, which determines the tone pitch. The velocity of the bow only determines the amplitude of the oscillation. In case of an iceberg sliding along the continental slope it remains unclear in which way a resonator is involved, especially in the case of frequency gliding.

One suggestion would be, that a varying stick-slip frequency might excite different natural modes of the iceberg, or multiples of them (Publication III). This assumption is supported by the stepwise changing of the spectral peak during the collision and grounding events of iceberg A-38B.

### **5.3 Floating iceberg events: fluid flow induced tremor**

#### **Oceanic T-phases and conversion to seismic waves**

From analysis of satellite imagery and ETOPO2 bathymetry it became clear that some of the tremor events recorded at the HOPE station are generated by freely floating icebergs. In this case, the vibrating iceberg causes oceanic T-phase waves, which are originally guided hydro-acoustic waves. However, upon arrival at the continental slope they are refracted and converted into a variety of complex seismic waves (e.g. *Talandier and Okal, 1998; De Groot-Hedlin & Orcutt, 2001*). The recorded seismic signal is then a superposition of body and surface waves originated by hydro-acoustic-to-seismic conversion with a composition of wave types depending on the steepness of the continental slope and the orientation of the travelling direction with respect to the slope. This explains the results of the 2-D particle motion analysis for these events (Publication III), as they show two mean directions with an approximate difference of  $90^\circ$ , indicating composition of longitudinal P-waves and transversal polarized S-waves.

#### **Fundamental ideas about fluid flow-induced tremor**

Iceberg-generated tremor shows a striking similarity to tremor events recorded in the vicinity of active volcanoes (*Müller et al., 2005*) which usually occur before and during an eruption. The mechanism which excites this volcanic tremor is not yet fully understood but is attributed to the flow of magma through narrow conduits (e.g. *Konstantinou and Schlindwein, 2002*). Several approaches to explain the physical processes behind this phenomenon have been proposed, which would also apply for water flow in iceberg rifts or cracks. An overview about possible mechanism is given below, following the review of *Rust et al.* (in Press).

##### **1. Hydrodynamic instabilities**

For flow with a high Reynolds number, tremor with the observed frequencies could be explained by hydrodynamic instabilities alone (eddy shedding, *Hellweg, 2000*). If a fluid jet meets an obstacle, eddies may

originate at the downstream side of the obstacle and detach, building a chain of vortices with alternating rotational direction. This phenomenon is known as von Kármán Vortex Street and can often be observed in clouds downstream of islands (fig. 5.1). The frequency  $f$  of the detaching eddies is related to the characteristic dimension of the obstacle  $d$ , and the flow velocity  $u$  of the fluid.

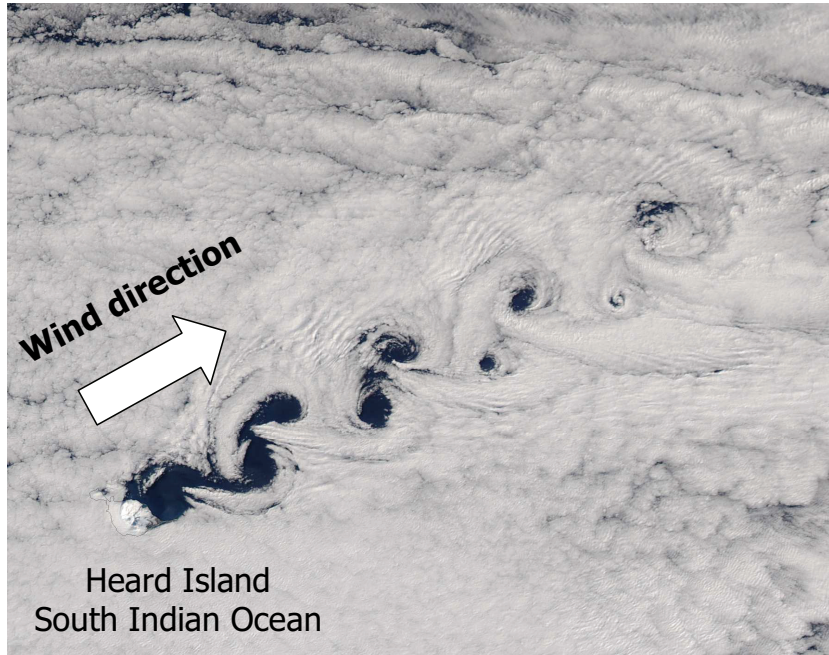


**Figure 5.1:** A von Kármán Vortex Street downwind of Heard Island. The Island represents an obstacle leading to the shedding of eddies with alternating sense of rotation. Image courtesy: MODIS Rapid Response Team, NASA/GSFC

For an idealized geometry where the obstacle is a cylinder with the diameter  $d$  the equation takes the form (e.g. *Hellweg*, 2000):

$$u = \sqrt{\frac{f \cdot \nu \cdot \text{Re}}{\text{St}}} \Leftrightarrow f = \text{St} \cdot \frac{\nu}{d}; \quad (5.1)$$

$$\text{with the Reynolds number } \text{Re} = \frac{u \cdot d}{\nu}$$

St is the so called Strouhal number and can be set to 0.2 (*Faber*, 1995) in the case of a cylinder;  $\nu$  is the kinematic viscosity of water ( $1.95 \times 10^{-6} \text{ m}^2 \text{ s}^{-1}$ ). The pressure oscillation associated with the formation of eddies on either side of the cylinder excites oscillation of the latter and may produce sound pulses in the fluid with frequency  $f$ . Hence, variable peaks in

the spectrograms of iceberg generated tremor could be explained by changes in the velocity of water flow at the opening of a rift at the iceberg edge. This is in good agreement with the observation that the tremor effects seem to be correlated with the tidal currents (Publication III), which influence the direction and the strength of the inflow at the rift opening. However, the processes can only be discussed in a qualitative way in this context, as the settings at the rift opening of a real iceberg are not directly comparable to the simple geometry of a cylindrical obstacle.

## 2. Coupling to a resonating reservoir

Another possibility is, that the initial pressure disturbance, which could be induced by the jet of water that is split at the crack opening, is coupling with standing hydro-acoustic waves in the fluid within the crack. This is comparable to the processes in wind instruments (e.g. the clarinet), where the pressure oscillation at the mouthpiece, which corresponds to the opening of the rift in the iceberg case, couples with the normal modes of the resonator. The resulting sound is the combination of a highly non-linear generator and an attached linear resonator (*Fletcher, 2001*).

## 3. Elastic normal modes on the channel walls

*Julian (1994)* explains flow induced oscillations of pressure driven fluid-flow through narrow channels with elastic channel walls. This non-linear model explains volcanic tremor features as period doubling phenomena, transitions from harmonic to chaotic states, and dependencies between oscillation period and tremor amplitudes. *Balmforth et al. (2005)* elaborated on this model: They expanded Julian's considerations by a stability analysis concluding that the system's stability depends on Rayleigh number, the crack's aspect ratio, fluid speeds, and elastic wave speeds.

In a non-linear system, frequency is not necessarily coupled to the geometry of the vibrating system. Thus, the non-linear generator enables phenomena like frequency gliding without changes in the geometry of the channels. It is not currently possible to decide which of these approaches is responsible for tremor generated by floating icebergs. Probably all processes contribute to the origin of the tremor events, which comprise a broad variety of signals.

## 5.4 Ocean swell as a source of iceberg fracturing?

Floating icebergs are subject to ocean swell, which can also be described as long period surface gravity waves. The period range of these waves, which ranges from about 12 to 18 s, comprises also the natural period  $T$  of a typical tabular iceberg bobbing on water (*Orheim et al.*, 1982; *Wadhams et al.*, 1983).

According to *Okal and MacAyeal* (2006),  $T$  can be calculated by the simple relation:

$$T = 2 \cdot \pi \cdot \sqrt{\left(\frac{\rho_i}{\rho_w}\right) \cdot \left(\frac{H}{g}\right)} \quad (5.2)$$

where  $\rho_i$ ,  $\rho_w$  are the densities of ice and water, their quotient representing the damping factor,  $H$  the ice thickness and  $g$  the gravity acceleration.

A tabular iceberg reacts as an elastic body under the swell-induced oscillations, but higher amplitude swell due to a storm event may cause fracturing of the iceberg. The corresponding bending forces were investigated by *Goodman et al.*, (1980), who measured surface heave response and surface strain on a relatively small tabular iceberg with a diameter of about 300 m. It was concluded that final failure of icebergs is the result of a fatigue process: Small initial cracks at the surface and also the bottom of the iceberg are likely to extend in each oscillation cycle until they become unstable. *Wadhams et al.* (1983) mounted strain meters onto larger tabular icebergs (diameter about 1 km) and found a maximal gain factor at the frequency 0.06 Hz. They also come to the conclusion that ocean swell could induce the failure of a tabular iceberg.

*MacAyeal et al.* (2006) deployed seismometers on large tabular icebergs in the Ross sea (for example B-15) and found the main energy of the recorded signals to be focussed in the range from 0.01 to 0.1 Hz, which they attributed to ocean swell with its origin in the pacific ocean. They were able to identify a particular storm event which appeared to be responsible for the break-up of the iceberg B-15 in October 2005.



**Figure 5.2:** Break-up of tabular iceberg A-38B in April 2004. Image courtesy: MODIS Rapid Response Team, NASA/GSFC.

Iceberg A-38B, which grounded about 100 km off the shore of South Georgia Island, broke apart on 17 April 2004 into two nearly equally sized parts (fig. 5.2). The part located closer to the island was still grounded, while the second part drifted northwards and decayed within several weeks. As no direct information about the iceberg's response to ocean swell is available in this case, data from the HOPE station was evaluated around the fracture event to investigate whether the failure of the iceberg could be due to the arrival of a high-amplitude swell field.

Ocean swell can be recorded as a microseismic signal by stations far away from coasts (e.g. *Friedrich et al.*, 1998), as the pressure oscillation at the sea floor due to the changing height of the overlying water column couples to the solid earth and transforms into seismic body waves. In contrast to the seismometer records on floating icebergs, the land-based stations also register the secondary ocean swell, which is the result of wave refraction along unique coastal geometries, and decreases data quality.

No particular swell event could be identified, but during the entire period the spectrum shows energy content in the relevant interval between 0.04 and 0.08 Hz (fig. 5.3). This supports the hypothesis that the final failure is the result of a fatigue process. Another aspect determining the timing of the failure could be the thinning process of the iceberg due to melting. The natural frequency depends on iceberg thickness. Thus, it rises as the iceberg melts and might approach the predominant frequency of ocean swell with time. Furthermore the rheologic properties of the ice body also changes with time, as it becomes colder and therefore more brittle due to the erosion of the relatively warm ice at the iceberg bottom (Publication II).

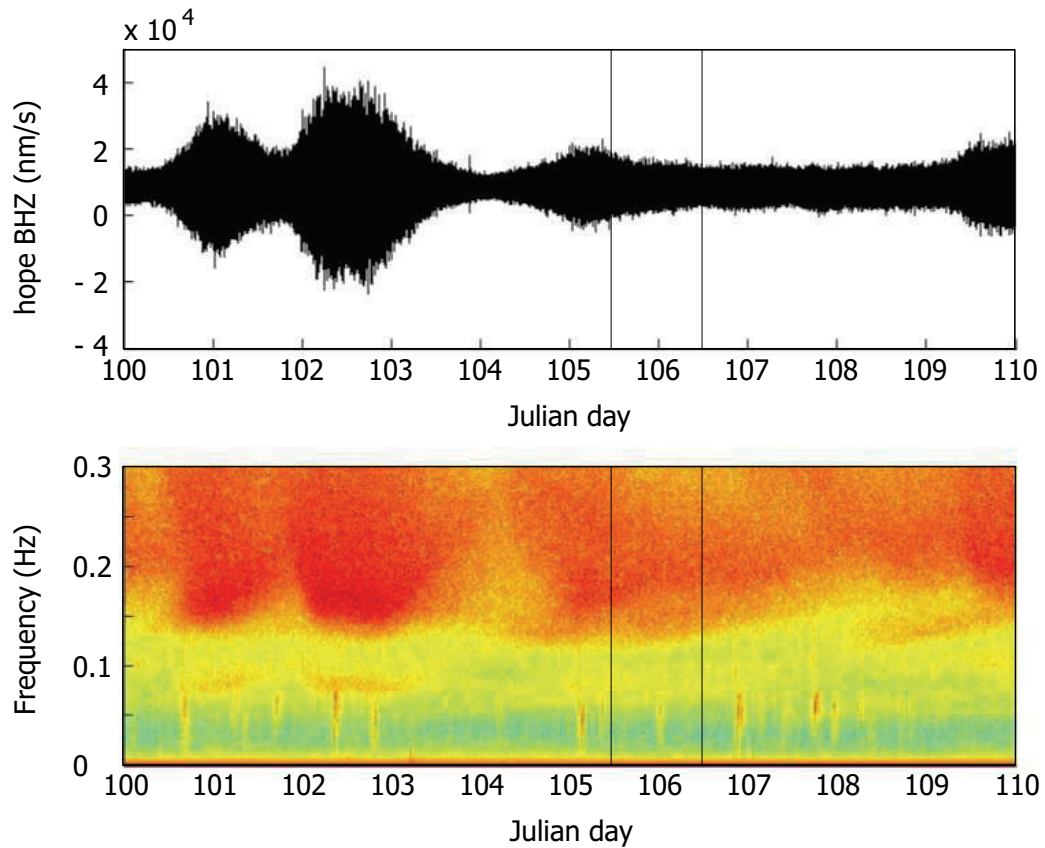


**Figure 5.3:** Seismogram and spectrogram of HOPE Station broadband data from 9 April to 19 April 2004. The break-up of tabular iceberg A-38B happened on 15 April, which corresponds to Julian day 106. The frequency of primary ocean swell is in the range of 0.04 to 0.08 Hz. Most of the energy of the signal is contained in frequencies above 1.2 Hz, which is attributed to the secondary ocean swell. At the time of the break-up no particular swell event can be detected. The short pulses in the lower part of the spectrum probably represent earthquake surface waves.



# 6

## Conclusion and outlook

A combined approach of numerical modelling and analysis of remote sensing data showed that the most significant process in iceberg evolution is melting at the iceberg base. This process causes the main geometric modification of the iceberg during long periods of its drift and also represents the most significant impact of tabular icebergs on their environment. Strain thinning due to horizontal spreading is of minor importance and only comparable to the magnitude of thinning due to melting for icebergs located in direct vicinity of the ice shelf fronts, where the water temperatures are low. The ice-flow velocity field within a tabular iceberg is of a radial shape, as the driving force applies at the entire ice front. Thus, no or very little horizontal shear stress and associated fracturing exists.

The parameter determining the stability of a tabular iceberg and the timing of its final decay appears to be not only ice thickness, but also the related change in the mean temperature. The relatively warm ice layers are eroded and the mean temperature of the iceberg decreases, resulting in less ductile behaviour and decreased fracture toughness of the ice body. The mean density of the iceberg decreases also due to melting, as the part of unconsolidated firm in the upper part of the iceberg increases relatively to the consolidated part. In the case of the iceberg A-38B the failure occurred, when the iceberg base was eroded up to the former transition zone between firm and consolidated ice.

Considering the fact that the inherent ice dynamics do not play a major role in iceberg evolution, it might be problematic to regard tabular icebergs as a model for ice shelves under warming conditions. In ice shelf decay, besides the thinning due to basal melting, the stress distribution within the ice itself, which is related to the coupling to the embayment and eventual pinning points, is a governing factor for the stability of the ice body.

If catastrophic decay of an ice body is induced by enhanced surface melting and percolating melt water, as it is assumed in the case of the Larsen A and B, fracturing related to shear zones provides working surface for the refreezing melt water. Thus, icebergs with the corresponding pre-calving evolution might show decay patterns similar to the Larsen Ice Shelf, if the fractures already exist before calving. This could be observed for the iceberg A-53 very recently during its decay near South Georgia Island.

Shortly after showing melt ponds at the surface, this iceberg deteriorated very fast and left a huge number of small icebergs. This has been also observed for icebergs from glacier tongues with pronounced surface fractures, which already existed before the calving (e.g. icebergs from the Ninnis Glacier Tongue and the tabular iceberg B-10A, which calved from the Twaites Glacier). However, the iceberg A-38B, which calved from the Ronne Ice Shelf, did not show these patterns of decay, indicating that surface and basal melting alone cannot cause a sudden catastrophic deterioration.

During the final decay very large mass of melt water is released into the ocean in short time, as the contact surface of ice and ocean is increased. However, already during its drift the iceberg continuously releases cold freshwater. ICESat altimetry measurements together with a physical melting model approach showed that the melting of icebergs is not only determined by ocean temperature and salinity, but also to some extent by the drift state and the relative velocity between iceberg and ocean. Assuming a constant turbulent exchange parameter during the entire drift leads to an overestimation of iceberg melt water in the Weddell Sea. The results presented in Publication II indicate that a large quantity of melt water is transported into the Scotia Sea or even further north, and helps to understand the relatively long survival of drifting tabular icebergs in these latitudes. As this study was focused on one particular iceberg, it is necessary to confirm the estimations of melt rates and associated turbulent exchange parameters by data from other icebergs, derived by satellite altimetry or, if possible, by radio echo sounding. Also the magnitude of surface melting and its impact on iceberg freeboard could be investigated further in this context.

Considering all aspects of a typical life cycle of an Antarctic tabular iceberg, the grounding and the related seismic events were also investigated as part of this thesis. By the combination of MODIS satellite imagery and ETOPO2 bathymetry data, it was possible to correlate single tremor events recorded at the HOPE seismic Station on South Georgia Island with collisions of the iceberg with the island shelf. The iceberg's grounding or sliding along the continental slope was attributed to diffuse tremor events with a background sound structured into overtones of a fundamental mode. The origin of this mode is not yet known, but the differing values for different icebergs indicate that it represents a natural mode of the iceberg, depending on the iceberg's shape or thickness. Superposed onto this background, gliding spectral peaks occur which are probably related to the stick-slip process between the iceberg and the island.

Harmonic tremor with only a few pronounced, variable frequency maxima occur exclusively for the floating iceberg A-43G, which contains a major rift structure. The excitation of the tremor is probably due to coupling of hydrodynamic instabilities with the reservoir modes of the rift channel or oscillations of the channel walls, in analogy to tremor excitation in volcanic

systems. This assumption is supported by the observation that particular current regimes around the iceberg are necessary to produce the tremor. The final part of the thesis leaves many open questions and might be the subject to further investigations. Especially interesting is the question whether the prominent fundamental modes in the grounding signals could be natural modes of the icebergs and provide information about its thickness or about its stability.



# Bibliography

- ALLEY, R.B. (1992).** Flow law hypotheses for ice sheet modelling. *J. Glaciol.*, **38**, 245-256.
- BALLANTYNE, J. (2002).** A multidecadal study of the number of Antarctic icebergs using scatterometer data. *In Proceedings of IGARSS'02, Toronto, Ontario, Canada, June 24-28, 2002*, **5**, 3029-3031.
- BALMFORTH, N.J., R.V. CRASTER, AND A.C. RUST (2005).** Instability in flow through elastic conduits and volcanic tremor, *J. Fluid Mech.*, **527**, 353-377.
- BARNES, W.L., T.S PAGANO, AND V.V. SALOMONSON (1998).** Prelaunch characteristics of the Moderate Resolution Imaging Spectrometer (MODIS) on EOS-AM1. *IEEE Transactions on Geoscience and Remote Sensing*, **36**(4), 1088-1100.
- BENN, D.I., C.R. WARREN, AND R.H. MOTTRAM (2007).** Calving processes and the dynamics of calving glaciers. *Earth-Sc. Rev.*, **82**, 143-179.
- BRAITHWAITE, R.J. AND O.B. OLESEN. (1989).** Calculation of glacier ablation from air temperature, west Greenland. In: Oerlemans, J. (Ed.), *Glacier Fluctuations and Climatic Change*, Kluwer, Dordrecht, The Netherlands, 219-233.
- CULL, D. (2007).** *Icebergs – The Antarctic comes to town*, Longacre Press, Dunedin, New Zealand.
- DANESI, S., S. BANNISTER, AND A. MORELLI (2006).** Repeating earthquakes from rupture of an asperity under an Antarctic outlet glacier. *Earth Planet. Sci. Lett.*, **253**(1-2), 151-158.
- DEGROOT-HEDLIN, C. AND ORCUTT, J. (2001).** T-phase observations in northern California: acoustic to seismic coupling at a weakly elastic boundary. *Pure Appl. Geophys.*, **158**, 513-530.
- EL-TAHAN, M.S., S. VENKATESH, AND H. EL-TAHAN (1987).** Validation and quantitative assessment of the deterioration mechanisms of Arctic icebergs. *J. Offshore Mech., Arctic. Eng.*, **109**, 102-108.

- FABER, T.E. (1995).** Fluid dynamics for physicists. Cambridge University Press, Cambridge.
- FLETCHER, N.H. (2001).** The nonlinear physics of music instruments, *Rep. Prog. Phys.*, **62**, 723-764.
- FOLDVIK, A. AND T. KVINDE (1974).** Conditional instability of sea water at the freezing point. *Deep-Sea Res.*, **21**, 169-174.
- FRIEDRICH, A., F. KRÜGER, AND K. KLINGE (1998).** Ocean-generated microseismic noise located with the Gräfenberg array. *J. Seismol.*, **2**, 47-64.
- GERDES, R., J. DETERMANN, AND K. GROSFELD (1999).** Ocean circulation beneath Filchner –Ronne-Ice-Shelf from three-dimensional model results. *J. Geophys. Res.*, **104**(C7), 15827-15842.
- GLADSTONE, R.M., G.R. BIGG, AND K.W. NICHOLLS (2001).** Iceberg trajectory modeling and meltwater injection in the Southern Ocean. *J. Geophys. Res.*, **106**(C9), 19903-19915.
- GOODMAN, D.J., P. WADHAMS, AND V.A., SQUIRE (1980).** The flexural response of a tabular ice island to ocean swell. *Ann. Glaciol.*, **1**, 23-27.
- GROSFELD, K., M. SCHRÖDER, E. FAHRBACH, R. GERDES, AND A. MACKENSEN (2001).** How iceberg calving and grounding change the circulation and hydrography in the Filchner Ice Shelf-Ocean System. *J. Geophys. Res.*, **106**(C5), 9039-9055.
- GROSFELD, K. AND H. SANDHÄGER (2004).** The evolution of a coupled ice shelf–ocean system under different climate states. *Glob. Plan. Change*, **42**, 107-132.
- HAMANN A. AND H. SANDHÄGER (2006).** Propagation of cracks through an ice shelf as precondition for calving: numerical experiments with an idealised glacial system. In: L.H. Smedsrud (Ed.), *comp. Forum for Research into Ice Shelf Processes (FRISP)*. Report No.14 (2006). Bergen, Bjerknes Centre for Climate Research, 23-29
- HELLMER, H. H. AND D. OLBERS (1989).** A two-dimensional model for the thermohaline circulation under an ice shelf. *Antarctic Science*, **3**(4), 433-442.
- HELLMER, H.H. (2004).** Impact of Antarctic ice shelf melting on sea ice and deep Ocean properties. *Geophys. Res. Lett.*, **31**(10), doi: 10.1029/2004GL019506.
- HELLWEG, M. (2000).** Physical models for the source of Lascar’s harmonic tremor. *J. Volcanol. Geotherm. Res.*, **101**, 183-198.

- HERTERICH, K. (1987).** On the flow within the transition zone between ice sheets and ice shelf. In: C.J. van der Veen and J. Oerlemans (Eds.), *Dynamics of the West Antarctic Ice Sheet*. D. Reidel, Dordrecht, 185-202.
- HERZFELD, U. C. (2004).** Atlas of Antarctica. Berlin/Heidelberg: Springer.
- HOLLAND, D. AND A. JENKINS (1999).** Modeling thermodynamic ice-ocean interactions at the base of an ice shelf. *J. Phys. Oceanogr.*, **29**(8 Part 1), 1787-1800.
- HUYBRECHTS, P. (1992).** The Antarctic ice sheet and environmental change: a three-dimensional modelling study. *Berichte zur Polarforschung*, **99**, Bremerhaven, Germany.
- JACOBS, S.S., H.H. HELLMER, C.S.M. DOAKE, A. JENKINS, AND R.M. FROLICH (1992).** Melting of ice shelves and the mass balance of Antarctica. *J. Glaciol.*, **38**(130), 375-387.
- JENKINS, A. (1991).** A one dimensional Model of Ice Shelf-Ocean Interaction. *J. Geophys. Res.*, **96**(C11), 20671-20677.
- JOUGHIN I. AND D. R. MACAYEAL (2005).** Calving of large tabular icebergs from ice shelf rift system. *Geophys. Res. Lett.*, **32**, L02501, doi: 10.1029/2004GL020978.
- JULIAN, B.R. (1994).** Volcanic tremor: Nonlinear excitation by fluid flow. *J. Geophys. Res.*, **99**(B6), 11859-11877.
- JULIAN, B.R. (2000).** Period doubling and other nonlinear phenomena in volcanic earthquakes and tremor, *J. Volcanol. Geotherm. Res.*, **101**, 19-26.
- KADER, B. A. AND A. M. YAGLOM (1972).** Heat and mass transfer laws for fully turbulent wall flows. *Int. J. Heat Mass Transfer*, **15**, 2329-2351.
- KONSTANTINOU, K. AND V. SCHLINDWEIN (2002).** Nature, wavefield properties and source mechanism of volcanic tremor: a review. *J. Volcanol. Geotherm. Res.*, **119**, 161-187.
- KOZIAN, W. (1994).** Die großen Eistriften im südwestlichen Teil des Südatlantiks und vor Kap Hoorn. *Deutsches Schifffahrtsarchiv* **17**, 51-92.
- LAZZARA, M.A., K.C. JEZEK, T.A. SCAMBOS, D.R. MACAYEAL, AND C. J. VAN DER VEEN (1999).** On the calving of icebergs from the Ross Ice Shelf. *Polar Geogr.*, **23**, 201-212.

- LEWIS, E.L. AND R.G. PERKIN (1986).** Ice Pumps and their rates. *J. Geophys. Res.*, **100**, 6961-6965.
- LICHEY, C. AND H.H. HELLMER (2001).** Modeling giant-iceberg drift under the influence of sea ice in the Weddell Sea, Antarctica. *J. Glaciol.*, **47**(158), 452-460.
- LONG, D. G., J. BALLANTYNE, AND C. BERTOIA (2002).** Is the Number of Icebergs Really Increasing? *EOS, Transactions of the American Geophysical Union*, **83**(43), 469 + 474.
- MACAYEAL, D.R. (1984).** Thermohaline circulation below the Ross Ice Shelf: a consequence of tidally induced vertical mixing and basal melting. *J. Geophys. Res.*, **89**, 597-606.
- MACAYEAL, D.R., S. SHABTAIE, C.R. BENTLEY, AND S.D. KING (1986).** Formulation of ice shelf dynamic boundary conditions in terms of a Coulomb rheology. *J. Geophys. Res.*, **91**(B8), 8177-8191.
- MACAYEAL, D.R., E. RIGNOT, AND C.L. HULBE (1998).** Ice-shelf dynamics near the front of the Filchner-Ronne Ice Shelf, Antarctica, revealed by SAR interferometry: model/interferogram comparison. *J. Glaciol.*, **44**(147), 419-428.
- MACAYEAL, D.R., OKAL, E.A. AND THE SOUTHBURG TEAM (2004).** An in-situ investigation of the seismic symphony of iceberg C16, Ross Sea, Antarctica. *Eos, Trans. Am. geophys. Un.*, **85**(47), F463 [abstract]
- MACAYEAL, D.R., E.A. OKAL, R.C. ASTER, J.N. BASSIS, K.M. BRUNT, L. MACCATHLES, R. DRUCKER, H.A. FRICKER, Y-J. KIM, S. MARTIN, M.H. OKAL, O.V. SERGIENKO, M.P. SPONSLER, AND J.E. THOM (2006)** Transoceanic wave propagation links iceberg calving margins of Antarctica with storms in tropics and Northern Hemisphere. *Geophys. Res. Let.*, **33**, doi: 10.1029/2006GL027235.
- MARTIN, S., R.S. DRUCKER, AND R. KWOCK (2007).** The areas and ice production of the western and central Ross Sea polynyas, 1992-2002, and their relation to the B-15 and C-19 iceberg events of 2000 and 2002. *J. Mar. Syst.*, doi: 10.1016/j.jmarsys.2006.11.008.
- MASSOM, R.A., K.L. HILL, V.I. LYTLE, A.P. WORBY, M.J. PAGET, AND I. ALLISON (2001).** Effects of regional fast ice and iceberg distributions on the behaviour of the Mertz Glacier polynya, East Antarctica. *Ann. Glaciol.*, **33**, 391-398.
- MASSOM, R.A. (2003).** Recent iceberg calving events in the Ninnis Glacier region, East Antarctica. *Antarctic Science*, **15**(2), 303-313.

- MÜLLER, C., SCHLINDWEIN, V., ECKSTALLER, A., AND MILLER, H. (2005).** Singing icebergs. *Science* **310**, 1299.
- NICHOLLS, K.W. AND S. ØSTERHUS (2004).** Interannual variability and ventilation timescales in the ocean cavity beneath Filcher-Ronne Ice Shelf, Antarctica. *J. Geophys. Res.*, **109**(C04014), doi : 10.1029/2003JC002149.
- NOAA NGDC (2006).** 2-minute Gridded Global Relief Data (ETOPO2v2). <http://www.ngdc.noaa.gov/mgg/fliers/06mgg01.html>.
- OKAL, E.A. AND D.R. MACAYEAL (2006).** Seismic recording on drifting icebergs: catching seismic waves, tsunamis and storms from Sumatra and elsewhere. *Seis. Res. Let.*, **77**(6), 659-671.
- ORHEIM, O., P. WADHAMS, AND M. KRISTENSEN (1982).** Iceberg response to sea state. *Iceberg Res.*, **1**, 10-15.
- PATERSON, W.S.B. (1994).** The Physics of Glaciers. 3rd ed., Pergamon/Elsevier, Oxford.
- RACK, W. AND H. ROTT (2004).** Pattern of retreat and disintegration of the Larsen B ice shelf, Antarctic Peninsula, *Annals of Glaciology*, **39**, 505-510.
- RIGNOT, E. AND D.R. MACAYEAL (1998).** Ice-shelf dynamics near the front of the Filchner-Ronne Ice Shelf, Antarctica, revealed by SAR interferometry. *J. Glaciol.*, **44**(147), 405-418.
- ROTT, H., W. RACK, T. NAGLER, AND P. SKVARCA (1998).** Climatically induced retreat and collapse of northern Larsen Ice Shelf, Antarctic Peninsula, *Annals of Glaciology*, **27**, 86-92.
- ROBE, R.Q., D.C. MAIER, AND R.C. KOLLMEYER (1977).** Iceberg deterioration. *Nature*, **267**, 505-506.
- RUST A.C., BALMFORTH, N.J. AND MANDRE, S. (IN PRESS).** The feasibility of generating low frequency volcano seismicity by flow through a deformable channel. In: *The Physics of Fluid Oscillations in Volcanic Systems*, Special Publication, Geological Society of London
- SANDHÄGER, H. (2000).** Quantifizierung eisdynamischer und massenhaushalts relevanter Basisgrößen eines Antarktischen Inlandeis-Schelfeis-Systems unter Einsatz eines numerischen Fließmodells. *Ph.D. thesis*, Westfälische Wilhelms-Universität Münster, Germany.
- SANDHÄGER, H., D. G. VAUGHAN, AND A. LAMBRECHT (2004).** Meteoric, marine and total ice thickness maps of Filchner-Ronne-Schelfeis, Antarctica. In: Smedsrud, L.H. (Ed.), *comp. Forum for*

*Research into Ice Shelf Processes (FRISP)*. Report No.15 (2004).  
Bergen, Bjerknes Centre for Climate Research, 23-29.

**SCAMBOS, T., C. HULBE, M. FAHNESTOCK, AND J. BOLANDER (2000).**  
The Link between climate warming and break-up of ice shelves in  
the Antarctic Peninsula. *J. Glaciol.*, **46**(154), 516-530.

**SCAMBOS, T., O. SERGIENKO, A. SARGENT, D. MACAYEAL, AND J.  
FASTOOK (2005).** ICESat profiles of tabular iceberg margins and  
iceberg breakup at low latitudes. *Geophys. Res. Lett.*, **32**, L23S09,  
doi: 10.10029/2005GL023802.

**SCHODLOK, M. P., H. H. HELLMER, J. N. SCHWARZ, AND T. BUSCHE  
(2005).** On iceberg behaviour: observations, model results and satellite  
data. In: Smedsrud, L. H. (Ed.), *comp. Forum for Research into Ice  
Shelf Processes (FRISP)*, Report No.16 (2005). Bergen, Bjerknes  
Centre for Climate Research.

**SCHODLOK, M. P., H. H. HELLMER, G. ROHARDT, AND E. FAHRBACH  
(2006).** Weddell Sea iceberg drift: Five years of observations. *J.  
Geophys. Res.*, **111**, C06018, doi:10.1029/2004JC002661.

**SCHUTZ, B.E., H.J. ZWALLY, C.A. SHUMAN, D. HANCOCK, AND J.P.  
DIMARZIO (2005).** Overview of the ICESat Mission. *Geophys. Res.  
Lett.*, **32**, L21S01, doi: 10.1029/2005GL024009.

**STEPHANI, H. AND G. KLUGE (1995).** Theoretische Mechanik. Spektrum  
Akademischer Verlag, Heidelberg.

**TALANDIER, J. AND OKAL, E.A. (1998).** On the mechanism of  
conversion of seismic waves to and from T waves in the vicinity of  
island shores. *Bul. Seismol. Soc. America*, **88**(2), 621-632.

**TALANDIER, J., HYVERNAUD, O., OKAL, E.A., AND PISERCHIA, P.F.  
(2002).** Long-range detection of hydroacoustic signals from large  
icebergs in the Ross Sea, Antarctica. *Earth and Planetary Science  
Letters*, **203**, 519-534.

**TALANDIER, J., HYVERNAUD, O., REYMOND, D., AND OKAL, E.A.  
(2006).** Hydroacoustic signals generated by parked and drifting  
icebergs in the Southern Indian and Pacific Oceans. *Geophys. J. Int.*,  
**165**, 817-834.

**VAN DER VEEN, C.J. AND A.J. PAYNE (2004).** Modelling land-ice  
dynamics. In: J.L. Bamber and A.J. Payne (Eds.), *Mass balance of  
the cryosphere*, Cambridge University Press, Cambridge, UK.

**VANWORMER, D. AND E. BERG (1973).** Seismic evidence for glacier  
motion. *J. Glac.*, **12**(65), 259-265.

- VENKATESH, S. (1986).** On the deterioration of a grounded iceberg. *J. Glaciol.*, **31**(111), 161-167.
- WADHAMS, P., M. KRISTENSEN, AND O. ORHEIM (1983).** The response of Antarctic icebergs to ocean waves. *J. Geophys. Res.*, **88**(C10), 6053-6065.
- WEAVER, C.S. AND S.D. MALONE (1979).** Seismic evidence for discrete glacier motion at the rock-ice interface. *J. Glac.*, **23**(89), 171-184.
- WEERTMAN, J. (1957).** Deformation of floating ice shelves. *J. Glaciol.*, **3**(21), 38-42.
- WIELANDT, E. (2002).** Seismic sensors and their calibration. In: P. Bohrmann and E. Bergmann (Eds.): *New manual of observatory practice*, **1**, Geoforschungszentrum Potsdam.
- WILLIAMS, M.J.M, A. JENKINS, J. DETERMANN (1998).** Physical controls on ocean circulation beneath ice shelves revealed by numerical models. In: *Ocean, ice and atmosphere: Interactions at the Antarctic Continental margin. Antarctic Research Series*, **75**, 285-299.
- WOLF, L.W. AND J.N. DAVIES (1986).** Glacier-generated earthquakes from Price William Sound, Alaska. *Bull. Seism. Soc. Am.*, **76**(2), 367-379.
- YOUNG, N.W. (2001).** An iceberg the size of Jamaica! *Australian Antarctic Magazine*, **1**, 24-25.
- ZWALLY, H. J., B. SCHUTZ, W. ABDALATI, J. ABSHIRE, C. BENTLEY, A. BRENNER, J. BUFTON, J. DEZIO, D. HANCOCK, D. HARDING, T. HERRING, B. MINSTER, K. QUINN, S. PALM, J. SPINHIRNE, AND R. THOMAS (2002).** ICESat's laser measurement of polar ice, atmosphere, ocean, and land. *J. Geodyn.*, **34**, 405-445.
- ZWALLY, H. J., R. SCHUTZ, C. BENTLEY, J. BUFTON, T. HERRING, J. MINSTER, J. SPINHIRNE, AND R. THOMAS (2003).** *GLAS/ICESat L2 Sea Ice Altimetry Data V024 and V026, GLAS/ICESat L1B Global Elevation Data V018*. Boulder, CO: National Snow and Ice Data Center. Digital Media.



# Danksagung

Zunächst gilt mein Dank Herrn Professor Heinrich Miller, der Erstgutachter dieser Arbeit ist. Herrn Professor Michael Schulz danke ich für die Übernahme des zweiten Gutachtens.

Mein spezieller Dank gilt Henner Sandhäger und Wolfgang Rack, auf deren Idee die vorliegende Arbeit beruht. Henner Sandhäger hat mich vor allem in der ersten Phase der Arbeit bei der Einarbeitung in die Modellierung unterstützt. Wolfgang Rack stand mir bei der Beschaffung und Bearbeitung von Fernerkundungsdaten zur Seite.

Bei Michael Schodlok möchte ich mich für die Zusammenarbeit während des zweiten Teils der Arbeit bedanken, die dazu führte, dass der ozeanographische Blickwinkel nicht zu kurz kam. Christian Müller hat mir die Einarbeitung in die Auswertung seismischer Daten für den letzten Teil der Arbeit sehr erleichtert. Bei ihm möchte ich mich für seine Zeit und das Interesse an meiner Arbeit bedanken, sowie für die geduldigen Erklärungen. Viele meiner Kollegen hier am AWI haben mich während dieser Arbeit durch wertvolle Anmerkungen und das Korrekturlesen meiner Texte unterstützt. Klaus Grosfeld und Thomas Kleiner (Uni Münster) danke ich für die Tipps zur Modellbeschreibung, Hartmut Hellmer für die Hinweise zum basalen Schmelzen von Schelfeisen. Bei Ralph Timmermann möchte ich mich ebenfalls für viele gute Ratschläge und sein Interesse an meiner Arbeit bedanken, ebenso wie bei Christine Wesche. Jill Schwarz danke ich für das Korrekturlesen des Einleitungstextes. Ohne Wolfgang Cohrs und seine Hilfe bei allen Rechnerangelegenheiten wäre diese Arbeit wohl niemals fertig geworden. Auch dafür meinen Dank!

Weiterhin möchte ich mich bei allen Kollegen von „Deck 4“ im Haus F für die angenehme Arbeitsatmosphäre bedanken, es war eine schöne Zeit!

Großen Dank schulde ich natürlich meiner Familie: Bei Christa Körner möchte ich mich für die liebevolle Betreuung meiner Kinder und die daraus resultierende zusätzliche Zeit bedanken, die ich für meine Arbeit aufwenden konnte. Meinen Eltern danke ich für die moralische Unterstützung und Ermutigungen während der gesamten Arbeit und die Bereitschaft in (Betreuungs-)Notsituationen immer einzuspringen. Andreas Heckel danke ich für die gute Teamarbeit und Arbeitsteilung, aber auch für das Leben nach der Arbeit, und dies gilt natürlich auch für meine beiden Kinder Malte und Lars.

Diese Arbeit wurde finanziert über die die Deutsche Forschungsgemeinschaft unter der Förderungsnummer SA 1029/1-1.



# Appendix A

## Publication I – Model experiments on large tabular iceberg evolution: ablation and strain thinning

**Daniela Jansen, Henner Sandhäger, and Wolfgang Rack (2005).**  
Final draft, published in: *Journal of Glaciology*, 51(174), 363-372.

### Abstract

Antarctic tabular icebergs are important active components of the ice – ocean system. To investigate the relevance of inherent ice dynamics to iceberg evolution, we developed a numerical model based on the fundamental equations of ice-shelf flow and heat transfer, forced by environmental parameters of the ice-ocean-atmosphere system. Model experiments with idealized icebergs of constant density show that the strain thinning rate for a typical iceberg with a thickness of 250 m and a temperature of  $-15^{\circ}\text{C}$  is about  $1\text{ m a}^{-1}$ . Sensitivity studies for different scenarios of environmental conditions confirmed the reliability of our model. A five year simulation of the evolution of iceberg A-38B yielded a mean decrease of thickness from 220 m to 106.3 m, 95 % of which was caused by basal melting, 1 % by surface melting and 4 % by strain thinning. We found iceberg spreading decelerating by about 75 % and ice temperatures being strongly affected by progressive erosion of the relatively warm basal layers and warming in the uppermost part. According to the model results, basal melting is the primary cause for change of iceberg geometry during drift, whereas strain thinning is only relevant in cold areas where basal melting is low.

## Introduction

Large tabular icebergs calved from ice shelves at the periphery of Antarctica are remarkable glacial features of the earth's southern polar region. Covering thousands of square kilometers, being several hundred meters thick and deteriorating progressively during their drift in the Southern Ocean, they represent active components of the ice sheet–ice shelf–ocean system. The oceanographic relevance of such icebergs consists, above all, in their potential to supply comparatively cold fresh water successively to the ocean during iceberg disintegration (Gladstone and others, 2001). This process influences the stability of the water column and thus affects water mass formation. Furthermore, grounding of large icebergs on shallow continental shelves and associated perturbations in the local bathymetric settings can cause changes in the circulation and affect sea ice conditions (Nøst and Østerhus, 1998; Grosfeld and others, 2001). The particular role of icebergs within the glacial system is evident from the fact that calving at the ice fronts represents the main loss of mass from the Antarctic ice sheet. According to Jacobs and others (1992), iceberg calving ( $\sim 2000 \text{ Gt a}^{-1}$ ) together with melting at the ice shelf bases ( $\sim 550 \text{ Gt a}^{-1}$ ) exceeds even the total annual mass gain of about 2200 Gt due to snow accumulation. However, the calving rate of large icebergs is subject to substantial fluctuations, since it may take the ice shelf decades to advance again up to its previous seaward extension after a major calving event.

Considering a typical lifecycle of a large tabular iceberg from calving to final decay, the different factors governing iceberg evolution can be roughly divided into three classes. The first class includes the various driving forces, which are exerted by ocean currents, wind stress, and sea ice pressure on the iceberg surfaces and cause icebergs to drift. Based on the force balance for iceberg motion in ice-covered seas, Lichey and Hellmer (2001) successfully simulated the drift trajectory of the large Antarctic iceberg C-7. Direct tracking and monitoring of large icebergs are usually done by analyzing satellite image sequences gathered with various sensors (e.g., Ballantyne, 2002).

The second class becomes apparent in a more or less continuous change of iceberg geometry during drift. Of primary importance are mass exchange processes which are part of the iceberg–ocean and iceberg–atmosphere interactions. These processes are basal melting, surface accumulation or melting, and ice front ablation due to wave erosion, melting, and calving of overhanging slabs. The rate of volume reduction is expected to increase significantly when icebergs approach lower latitudes, because the rise in ambient temperature leads to increased melting and reinforced decay of the iceberg margins. A further process contributing to continuous iceberg deformation is the strain thinning associated with ice-shelf-like spreading of the iceberg. To quantify this spreading, which is driven by the stress

imbalance at the ice front and gradients in the ice thickness distribution, the velocity of ice flow, the temperature regime and the iceberg geometry need to be known in detail. However, neither respective measurements nor specific model studies on the inter-relation between inherent iceberg dynamics and climatic boundary conditions are available yet.

The third class of processes relevant to iceberg evolution is fracturing on various scales. Collisions with the ice shelf front or other icebergs as well as grounding can induce bending moments in the iceberg which initiate crack formation and propagation. Fracture processes can also result from unbalanced hydrostatic stresses due to rapid inhomogeneous iceberg ablation. This also might explain the typical occurrence of small-scale calving at ice fronts with local melt enhancement. The knowledge of both the decisive mechanisms of iceberg fracturing and the possible links to the inherent stress distribution is still incomplete.

Since major fracture events usually occur in early and rather late states of large iceberg evolution, there are comparatively long periods where changes in iceberg geometry mainly result from the processes of the above-mentioned second class, i.e., strain thinning and continuous iceberg interaction with ocean and atmosphere. To gain deeper insight into this aspect of iceberg evolution, we have developed a numerical iceberg model and performed a series of basic and advanced simulations. After the model description in the next section, selected results from our experiments are presented, including a time-dependent simulation describing the substantial mass loss of the tabular iceberg A-38B during its 5-year drift from the Ronne Ice Shelf front to near South Georgia located ~2500 km further north.

## Model description

The first version of the new tabular iceberg model simulates the continuous iceberg evolution caused by inherent ice dynamics and variable environmental boundary conditions. Driving forces and stresses associated with this class of influencing factors are implemented, but friction and vertical shear strain due to bending forces are neglected. Thus, the ice body is assumed to be in hydrostatic equilibrium with depth-invariant horizontal flow velocities. However, iceberg temperature and density are allowed to vary with depth. Considering this so-called ice shelf approximation, the continuum-mechanical balance equations for momentum and mass, in combination with Glen's flow law, yield three model equations for the flow regime of tabular icebergs and ice shelves. (e.g., MacAyeal and others, 1986). With regard to a regular Cartesian  $x, y, z$ -coordinate system these governing equations of iceberg flow read:

$$2 \frac{\partial}{\partial x} (F \dot{\epsilon}_{xx}) + \frac{\partial}{\partial x} (F \dot{\epsilon}_{yy}) + \frac{\partial}{\partial y} (F \dot{\epsilon}_{xy}) = \bar{\rho} g H \frac{\partial(h-H)}{\partial x} + g \frac{\partial}{\partial x} \left( \int_{h-H}^h \int_z^h \rho dz' dz'' \right), \quad (1)$$

$$2 \frac{\partial}{\partial y} (F \dot{\epsilon}_{yy}) + \frac{\partial}{\partial y} (F \dot{\epsilon}_{xx}) + \frac{\partial}{\partial x} (F \dot{\epsilon}_{xy}) = \bar{\rho} g H \frac{\partial(h-H)}{\partial y} + g \frac{\partial}{\partial y} \left( \int_{h-H}^h \int_z^h \rho dz' dz'' \right) \quad (2)$$

and

$$\rho w = (\dot{\epsilon}_{xx} + \dot{\epsilon}_{yy}) \int_z^h \rho dz' + u \frac{\partial}{\partial x} \left( \int_z^h \rho dz' \right) + v \frac{\partial}{\partial y} \left( \int_z^h \rho dz' \right) + \frac{\partial}{\partial t} \left( \int_z^h \rho dz' \right) - \rho_c a_s \quad (3)$$

where

$$F = HA \overline{\dot{\epsilon}}^{-\frac{1}{n}} \dot{\epsilon}^{\frac{1}{n}-1}, \quad \dot{\epsilon}_{xx} = \frac{\partial u}{\partial x}, \quad \dot{\epsilon}_{yy} = \frac{\partial v}{\partial y}, \quad \dot{\epsilon}_{xy} = \frac{1}{2} \left( \frac{\partial u}{\partial y} + \frac{\partial v}{\partial x} \right),$$

$$\dot{\epsilon}^2 = \dot{\epsilon}_{xx}^2 + \dot{\epsilon}_{yy}^2 + \dot{\epsilon}_{xx} \dot{\epsilon}_{yy} + \dot{\epsilon}_{xy}^2,$$

where  $u$  and  $v$  are the horizontal velocities of ice flow,  $w$  is the vertical velocity,  $\dot{\epsilon}_{xx}$ ,  $\dot{\epsilon}_{yy}$  and  $\dot{\epsilon}_{xy}$  are the horizontal components of the strain rate tensor,  $\dot{\epsilon}$  is the effective strain rate,  $h$  the surface elevation above sea level,  $H$  the ice thickness,  $g$  the acceleration due to gravity,  $\rho_c$  the density of completely consolidated ice ( $915 \text{ kg m}^{-3}$ ),  $a_s$  the surface accumulation rate measured in  $\text{m a}^{-1}$  ice equivalent, and  $t$  the time. The parameters  $A$  and  $n$  of Glen's flow law are predetermined as follows: the flow factor  $A$  depends on ice temperature  $T$  as indicated in Figure 1 a; the exponent  $n$  is equal to 3. The ice density  $\rho$  is specified by means of an appropriate constitutive relation, such as that shown in Figure 1 b. The bar indicates the depth averaged value of the respective parameter.

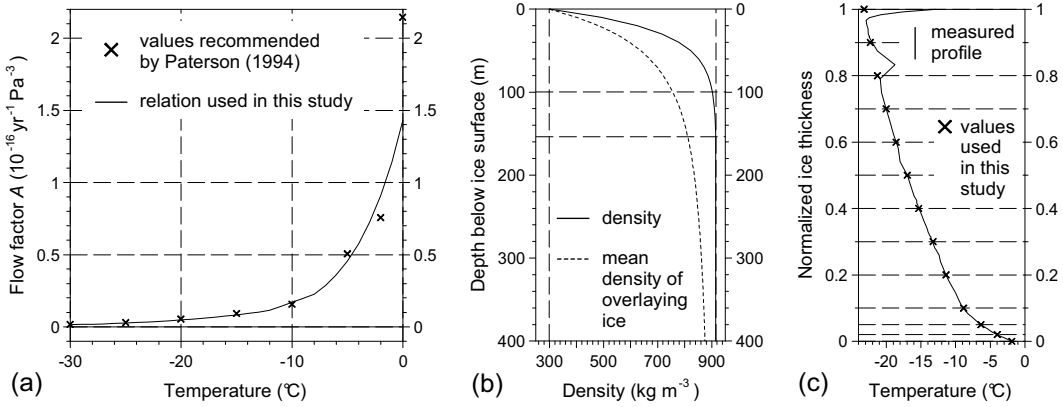


**Fig. 1.** (a) Temperature dependency of factor  $A$  of Glen's flow law; (b) prescribed depth profiles of ice density  $\rho$  and mean density of overlaying ice  $\bar{\rho}$ ; (c) temperature-depth profile based on borehole measurements near the Ronne Ice Shelf front (ice thickness at drill site was 240 m). Marked temperature values were used to initialize time-dependent iceberg simulations.

The heat transfer equation completes the basic model equation set:

$$\rho c_p \frac{\partial T}{\partial t} = K \operatorname{div}(\operatorname{grad} T) + \frac{\partial K}{\partial T} (\operatorname{grad} T)^2 - \rho c_p \bar{u} (\operatorname{grad} T) + 2A^{-\frac{1}{n}} \dot{\epsilon}^{\frac{1}{n}+1}, \quad (4)$$

where  $T$  is the ice temperature,  $\bar{u} = (u, v, w)^T$  the velocity vector,  $c_p$  is the specific heat capacity, and  $K$  the thermal conductivity. To compute ice velocities and temperatures for the respective iceberg geometry and density distribution, several boundary conditions have to be specified.

While boundary values are prescribed for the mean annual surface temperature  $T_s$  and the temperature  $T_b$  at the iceberg base, the iceberg front is treated as a perfectly heat isolating interface. The only boundary condition required for the ice velocity is based on the balance of forces formulated for an ice edge of idealized rectangular shape (Weertman, 1957). If the ice flow takes place in the  $x$ -direction, perpendicular to the iceberg front, the condition reads:

$$\frac{\partial u}{\partial x} = A^{-\frac{1}{n}} \dot{\epsilon}^{1-\frac{1}{n}} \frac{g}{2H} \left( \int_{h-H}^h \int_z^h \rho dz' dz'' - \rho_w \frac{(h-H)^2}{2} \right) - \frac{1}{2} \frac{\partial v}{\partial y}; \quad \frac{\partial v}{\partial x} = -\frac{\partial u}{\partial y}. \quad (5)$$

As this boundary condition is not unique, each velocity field  $\vec{u}_{tot}$  of the form

$$\vec{u}_{tot} = \vec{u} + \sum_l \vec{u}_{rot|l} + \vec{u}_{trans} = \begin{pmatrix} u \\ v \end{pmatrix} + \sum_l b_l \begin{pmatrix} y - y_l \\ -x + x_l \end{pmatrix} + \begin{pmatrix} u_0 \\ v_0 \end{pmatrix}, \quad (6)$$

where rigid body rotations  $\vec{u}_{rot}$  and a translation  $\vec{u}_{trans}$  are superimposed to the velocity of ice flow  $\vec{u}$ , is still a solution of the set of Equations (1), (2), and (5). However, the superimposed velocity fields lead to spurious contributions to the advection in calculating temperature distribution or to the calculated thickness evolution (cf., Equations (4) and (7)) and may even cause divergences in the numerical solution of the model equations. Therefore, they are reduced instantaneously by the constraint of minimal kinetic energy.

The basic equation for calculating the evolution of iceberg geometry is the vertically integrated mass balance equation which describes the temporal change in ice thickness (e.g., Paterson, 1994):

$$\frac{\partial H}{\partial t} = \frac{\rho_c}{\bar{\rho}} (a_s + a_b) - \frac{1}{\bar{\rho}} \left( \frac{\partial}{\partial x} (\bar{\rho} H u) + \frac{\partial}{\partial y} (\bar{\rho} H v) \right) - \frac{H}{\bar{\rho}} \frac{\partial \bar{\rho}}{\partial t}, \quad (7)$$

where  $\bar{\rho}$  is the depth-averaged density and  $a_b$  the basal mass balance measured in  $\text{m a}^{-1}$  ice equivalent. Iceberg thickness evolution is accompanied by surface elevation changes according to the hydrostatic relation  $h = (1 - \bar{\rho} / \rho_w) H$ , where  $\rho_w$  is the density of sea water.

A detailed description of the numerical implementation and the model grid is given in Grosfeld and Sandhäger (2004).

## Strain thinning of idealized icebergs

We performed a first series of numerical experiments to test main modules of the iceberg model and to gain insight into basic ice dynamical characteristics of large tabular icebergs. The model was applied to strongly idealized icebergs, each with constant density ( $915 \text{ kg m}^{-3}$ ) and temperature (i.e., the flow factor  $A$  is also constant) and a rectangular shape with side lengths of 40 km and 72 km. The chosen iceberg surface area of  $2880 \text{ km}^2$  is consistent with typical values observed for large icebergs.

Assuming that the idealized iceberg with a thickness of 250 m and a temperature of  $-20^\circ\text{C}$  is in steady state ( $\partial H / \partial t = 0$ ), a diagnostic model run yields a radial horizontal flow velocity field symmetric to the center of gravity (Fig. 2):

$$\vec{u} = \begin{pmatrix} u \\ v \end{pmatrix} = a \begin{pmatrix} x - x_0 \\ y - y_0 \end{pmatrix} \text{ with } a \approx 9.84 \times 10^{-4} \text{ a}^{-1}, x_0 = 44 \text{ km}, \text{ and } y_0 = 28 \text{ km},$$

(8)

complying with Equations (1) and (2). The value for  $a$  derived analytically by inserting Equation (8) in the boundary condition given by Equation (5) agrees well with the model results:

$$a = 3A \left( \frac{gh\rho_c}{6} \right)^3 = 9.89 \times 10^{-4} \text{ a}^{-1}. \quad (9)$$

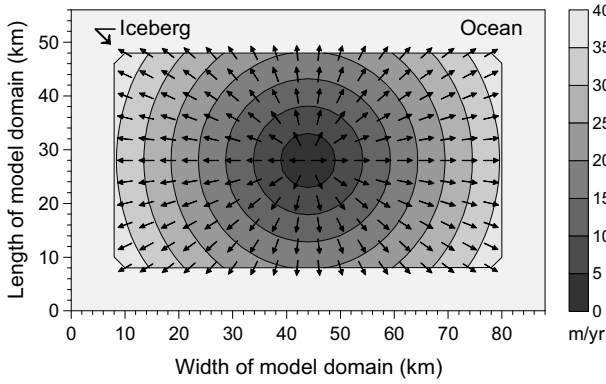


**Fig. 2.** Modeled radial distribution of the horizontal velocity of an idealized iceberg with constant temperature ( $-20^\circ\text{C}$ ), density ( $915 \text{ kg m}^{-3}$ ), and thickness (250 m). Arrows indicate the direction of ice flow.

Next we performed a time-dependent model run for an idealized iceberg with an initial thickness of 500 m, a temperature of  $-20^\circ\text{C}$ , and no vertical mass exchange ( $a_s = a_b = 0$ ). Ice front erosion and migration were ignored. During the simulation period of 250 a, the iceberg thickness decreased to 213 m due to strain thinning. Figure 3 a shows strain thinning rates with respect to iceberg thickness derived from model results. Additionally, thinning rates for different ice temperatures and flow factors respectively, were calculated as follows:

$$\frac{\partial H}{\partial t} = -2Ha = -6HA \left( \frac{gh\rho_c}{6} \right)^3 = -6A \left( \frac{g\rho_c}{6} \left( 1 - \frac{\rho_c}{\rho_w} \right) \right)^3 H^4, \quad (10)$$

which results directly from insertion of the velocity distribution described by Equation (8) into the continuity equation for ice thickness (Equation (7)) for an idealized iceberg with constant density. Model results agree well with the analytical solution (10). This is also clear in Figure 3 b, where the norm of the horizontal velocity vector at 20 km distance to the center of gravity is plotted vs. iceberg thickness. Analytical curves of flow velocity in Figure 3 b are based on the equation

$$|\bar{u}| = a\sqrt{(x-x_0)^2 + (y-y_0)^2} = 3A \left( \frac{g\rho_c}{6} \left( 1 - \frac{\rho_c}{\rho_w} \right) \right)^3 H^3 \sqrt{(x-x_0)^2 + (y-y_0)^2}. \quad (11)$$

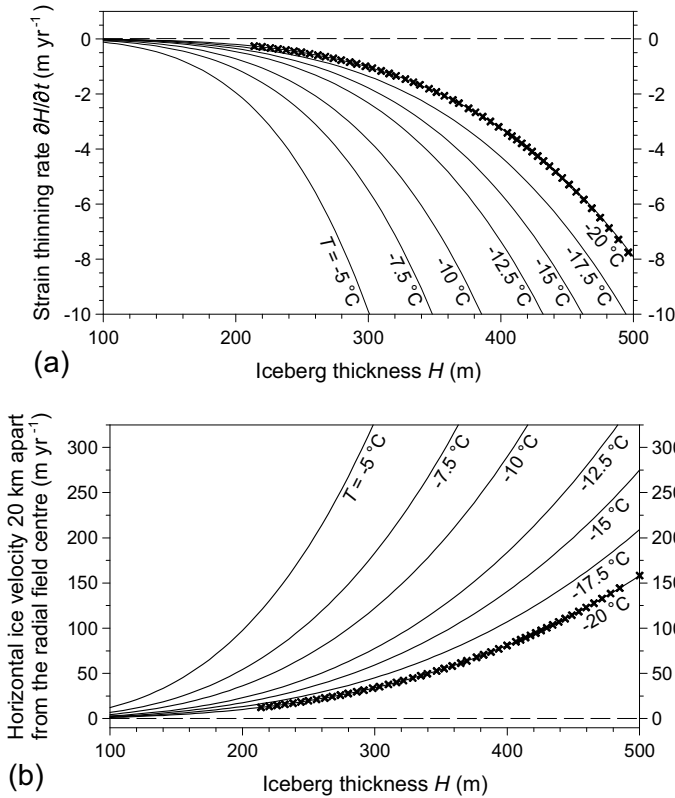


**Fig. 3.** (a) Variation of strain thinning rate  $\partial H / \partial t$  with thickness  $H$  and temperature  $T$  of a rectangular isothermal iceberg with constant density ( $915 \text{ kg m}^{-3}$ ), based on analytical calculations of Equation (10); crosses indicate results from a time-dependent application of the iceberg model. (b) Corresponding diagram of horizontal ice velocity 20 km apart from the radial field centre versus iceberg thickness and temperature, based on Equation (11).

As real Antarctic tabular icebergs often comprise thickness gradients in the order of a few meters per kilometer, which developed in their pre-calving states as a result of the characteristic seaward ice shelf spreading, we performed further model runs with icebergs still strongly idealized but containing a thickness gradient. The model results shown in Figure 4 indicate that the influence of typical ice thickness gradients on strain thinning is negligible. Thus, the findings in Figure 3 a provide a basis for pre-estimating strain thinning of real tabular icebergs with a roughly known thickness and mean temperature. According to the model results, an average iceberg with a thickness of 250 m and a mean temperature of  $-15^\circ\text{C}$  is subject to a strain thinning rate of about  $1 \text{ m a}^{-1}$ . This contribution to thickness decrease is probably of the same order of magnitude as basal melting in the Southern Weddell Sea (Schodlok and others, 2005). However, in lower latitudes, where basal melting enhances significantly, strain thinning becomes less important to iceberg evolution.

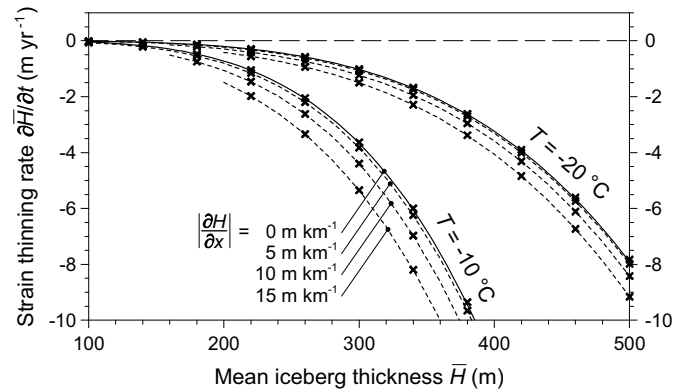


**Fig. 4. (a)** Variation of strain thinning rate  $\partial\bar{H}/\partial t$  with mean iceberg thickness  $\bar{H}$  for different ice temperatures and longitudinal thickness gradients  $\partial H/\partial x$ . Model results (broken lines and crosses) obtained for an idealized isothermal iceberg of constant density ( $915 \text{ kg m}^{-3}$ ) match the curves for  $\partial H/\partial x=0$  which are derived from analytical calculations of Equation (10).

## Experiments for icebergs interacting with ocean and atmosphere

Approaching more realistic simulations of the evolution of tabular icebergs, we carried out a second series of model studies with essentially reduced simplifications compared with the strongly idealized basic experiments. In particular, we included the impact of ocean and atmosphere on iceberg evolution and considered variable density and temperature distributions.

An equation of state established for the Ronne Ice Shelf determines the density profile, which comprises a gradual change from snow to firn and finally to completely consolidated ice within about the uppermost 100 m of the iceberg (Fig. 1 b). The initial temperature distribution is based on borehole measurements at a drilling site near the Ronne Ice Shelf front (Figs. 1 c and 5 a; Grosfeld and Thyssen, 1994), which delivered a temperature-depth profile indicating approximate thermal equilibrium with moderate basal melting. However, the heat transfer relation, Equation (4), determines the time-dependent variation of the temperature distribution during iceberg evolution. The dimensions of the tabular iceberg are set to  $56 \text{ km} \times 136 \text{ km}$  with a thickness of 230 m, i.e., similar to the geometry of iceberg A-38. Possible ice front migration during the simulation time of 5 years is neglected, and temporal resolution of the simulation is 0.25 a.

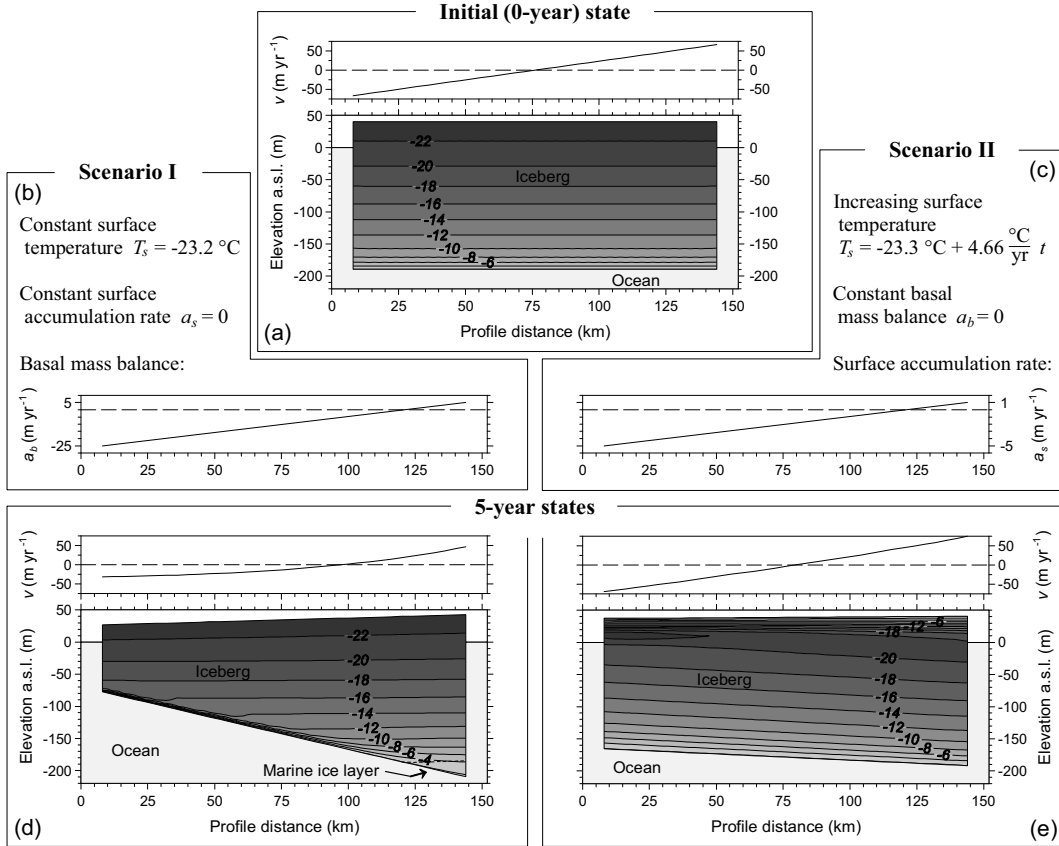


**Fig. 5.** Simulated evolution of a tabular iceberg interacting with ocean and atmosphere for a constant surface area of  $56 \text{ km} \times 136 \text{ km}$ . (a) Initial horizontal velocity  $v$  and vertical distribution of temperature  $T$  (in  $^\circ\text{C}$ ) along the longitudinal iceberg axis; (b), (c) prescribed climatic boundary conditions for scenarios I and II; (d), (e) distributions of  $v$  and  $T$  along the longitudinal iceberg axis after 5 years of integration under environmental conditions I and II, respectively. Spatial variations of forcing parameters only occur in profile direction.

To investigate separately the impact of interactions with ocean and atmosphere on iceberg evolution, we performed model applications for two scenarios of environmental conditions (Fig. 5 a,c). The first scenario focused on iceberg-ocean-interaction, the second on changes in atmospheric conditions. In the ocean experiment, the basal mass balance  $a_b$  was specified to change from pronounced melting to accumulation of marine ice along the longitudinal axis of the iceberg, but was constant with time. No mass exchange was allowed at the iceberg surface ( $a_s=0$ ), and mean annual surface temperature was set constant with time at  $T_s=-23.2 \text{ }^\circ\text{C}$ . In the second scenario, the surface mass balance was specified to change linearly from ablation of  $a_s=-5 \text{ m a}^{-1}$  ice equivalent to an accumulation of  $a_s=1 \text{ m a}^{-1}$  ice equivalent along the longitudinal axis of the iceberg. There was no basal melting for the entire iceberg. The surface temperature increased with time.

Compared to the initial configuration of the iceberg, which showed a radial symmetric distribution of the horizontal flow velocity, the resulting evolution of the iceberg scenarios show obvious differences marked by the influence of the prevailing environmental conditions (Fig. 5 d, e). In Scenario I, the enhanced basal melting causes erosion of the relatively warm ice in the lower part of the iceberg, leading to strong vertical temperature gradients above the iceberg base. In contrast, basal accumulation processes at the other end of the profile result in an increase in thickness due to the formation of marine ice with temperatures just below the freezing point. Using the numerical approach presented by Grosfeld and Sandhäger (2004), the maximum thickness of marine ice after 5 years was calculated to be about 24.7 m. Furthermore, the temperature distribution for Scenario I presented in Figure 5 d shows the minor importance of heat conduction within the ice body. The center of the horizontal radial velocity field shifted towards the section with greater thickness and higher temperatures.

The boundary conditions of Scenario II induced the migration of the temperature minimum to the inner part of the iceberg. A negative mass balance caused a steep temperature gradient (Fig. 5 e) related to a temperature minimum close to the iceberg surface. Accumulation shifted this minimum to deeper layers. However, the temperature distribution in the central and lower part of the iceberg was not influenced significantly during the five year period. Strain thinning amounted to about  $0.5 \text{ m a}^{-1}$  (Fig. 3 a) for both environmental settings, and is therefore a minor effect compared to mass exchanges with ocean and atmosphere.

## Iceberg A-38

### Observed evolution

Considering the results of these numerical studies, we are confident that the model provides realistic time-dependent simulations of the development of idealized tabular icebergs with respect to inherent ice dynamics and fundamental exterior parameters. As a next step we applied the model to a real Antarctic tabular iceberg, which was selected using the following criteria: the initial iceberg geometry and its temperature profile are well-known; the iceberg has been subject to a long-distance drift associated with significant changes in environmental conditions; observations and supplementary data are sufficient to provide a reliable description of the iceberg evolution. All these demands are met by iceberg A-38, whose evolution will be briefly described and documented by satellite images (NOAA DMSP, MODIS, Radarsat, Envisat) in the following. The Antarctic Iceberg Database (Brigham Young University), which is based on satellite-borne scatterometer data, provided the drift track.

In October 1998 the giant tabular iceberg A-38 calved off the Ronne Ice Shelf west of Berkner Island, where several pronounced slow growing inlets characterized the structure of the ice shelf. The crack which led to this calving event followed the connecting line between two inlet tips, forming a tabular iceberg with an approximate size of  $150 \text{ km} \times 50 \text{ km}$ . The calving process probably occurred on a very short time-scale.

Iceberg A-38 was first detected on October 15<sup>th</sup>, 1998, by NOAA DMSP satellite. Following a collision with the ice shelf front shortly after calving, A-38 broke into two halves of about equal size: A-38A, the formerly eastern part, still containing two major inlets of 40 km length, and A-38B, the western part, on which we focus in this study (Fig. 6 a). A-38B drifted within the Weddell Gyre towards the Antarctic Peninsula and then followed the coastline northwards (Fig. 6 b). The drift velocity varied strongly with sea ice coverage and thickness, including periods of stagnation. In February 2003, the iceberg reached the tip of the Antarctic Peninsula and proceeded further north, leaving the area of permanent sea ice coverage. An optical satellite image (MODIS) shows the iceberg A-38B on February 17<sup>th</sup>, 2003, (Fig. 6 c).

In the Scotia Sea, the iceberg accelerated considerably and reached South Georgia by December 2003. A-38B passed the island to the east and grounded in January 2004 north east of South Georgia. During the drift the iceberg shape changed insignificantly, except for small-scale calving at its margins (Fig. 6 d). On April 15<sup>th</sup>, 2004, A-38B broke into two nearly equal-sized halves (Fig. 6 e). The part located closer to the island was still grounded, while the other part was drifting northwards again. The grounded iceberg fragment broke into several pieces during August and September 2004 (Jansen and others, 2005).

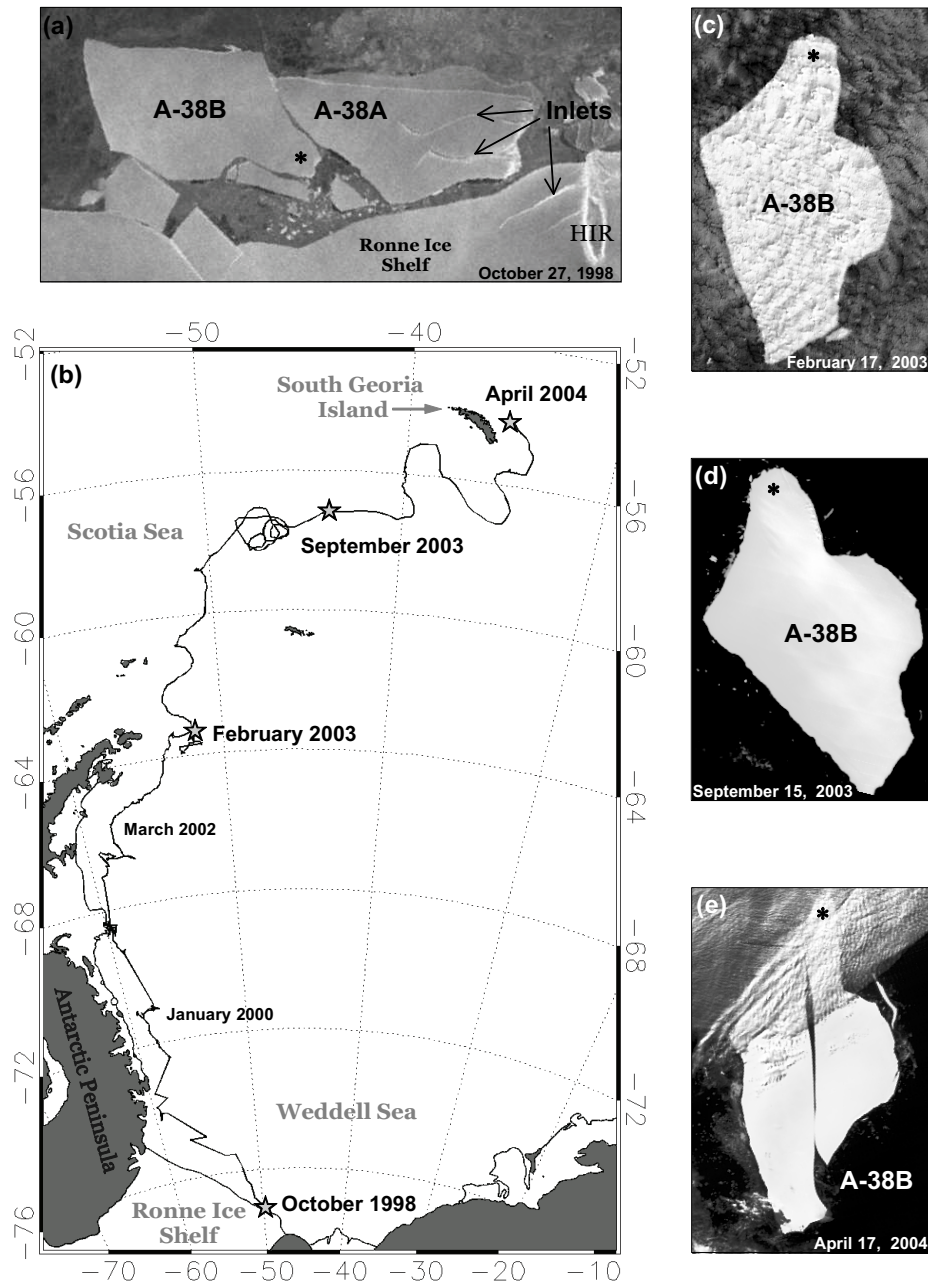


**Fig. 6.** (a) Major fracture events occurred in October 1998, when A-38 calved and broke into parts A and B (RADARSAT ScanSAR image © Canadian Space Agency, 1998); HIR: Hemmen Ice Rise (b) Map of Weddell Sea and Scotia Sea with drift trajectory of large tabular iceberg A-38B. (c)-(e) Satellite images showing different stages of the A-38B evolution (MODIS images partly with clouds, image courtesy MODIS Rapid Response Team, NASA/GSFC). In austral autumn 2004 A-38B broke-up into several pieces during a phase of grounding near South Georgia. The stars on A-38B images serve for orientation.

### Diagnostic model run

We first performed a diagnostic simulation of ice dynamics of A-38 immediately after calving to examine the velocity and the corresponding stress field for an anomaly which could have supported the later crack formation. The shape of the iceberg was obtained from Radarsat images and the corresponding ice thickness distribution derived from a digital ice thickness model of the Filchner-Ronne Ice Shelf (Sandhäger and others, 2004) as shown in Figure 7 a. The thickness varies from about 300 m at the crack line to about 150 m at the former ice shelf front, yielding a gradient of about  $3 \text{ m km}^{-1}$  along the shorter axis of the iceberg. Surface height above sea level is determined by the hydrostatic relation,  $h = 0.108 \times H + 15.5 \text{ m}$  according to the density distribution shown in Figure 1 b.

The initial vertical temperature distribution was derived from borehole measurements at the drilling site near the Ronne Ice Shelf front (Fig. 1 c; the position of this site is marked in Fig. 7 a; Grosfeld and Thyssen, 1994). Results of radio-echo sounding surveys indicated marine ice beneath A-38 or later A-38B, reaching a maximum thickness of more than 75 m (Thyssen and others, 1992; Fig. 7 a). As the temperature profile does not show any anomalies, and the density difference between marine and meteoric ice is small (Oerter and others, 1992), no differentiation between marine and meteoric ice was included in the model calculations.

The model grid had a horizontal resolution of 750 m; the vertical resolution is analogous to the model settings described above. The resulting velocity field of the diagnostic run for iceberg A-38 is presented in Figure 7 b. It shows radial symmetry, although the influence of thickness distribution can be seen in some areas of the iceberg: for example, the position of zero velocity was shifted towards maximum thickness. According to Figure 4, an initial strain thinning of about  $0.5 \text{ m a}^{-1}$  should be expected. The estimation of flow velocity 20 km from the position of zero velocity (Fig. 3 b) gave about  $25 \text{ m a}^{-1}$ , which fits well with the model results.

The corresponding stress field for the iceberg does not show pronounced anomalies which might be regarded as potential areas for spontaneous crack formation. However, the effective deviatoric stress near the ice surface  $\tau_s$  (Fig. 7 c) is closely correlated with the thickness distribution, reaching its maximum of about 100 kPa at the position of greatest thickness. This is also the position where the crack initiated, which split A-38 into two halves (cf., Fig. 6 a). According to Vaughan (1993), the surface tensile strength  $\sigma_{crit}$  for the Ronne Ice Shelf is in the range of 190 - 250 kPa, corresponding to a critical deviatoric stress of 110 - 144 kPa. This may explain why the crack started at the position of maximum iceberg thickness.

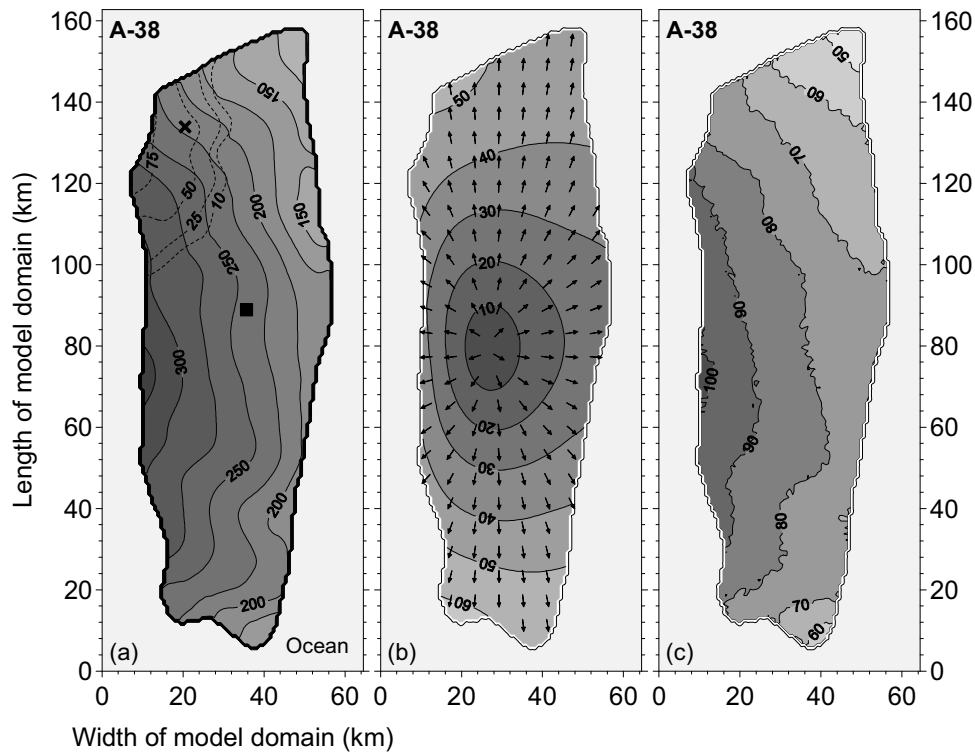


**Fig. 7.** Diagnostic model results for the large Antarctic iceberg A-38. (a) Prescribed distribution of total ice thickness  $H$  (in m). The locations of the former Filchner-Station and the drill site which provided the temperature-depth profile shown in Figure 1 are marked with a square and cross, respectively. Dashed contours indicate the thickness  $H_{mar}$  of a basal marine ice layer formed prior to the separation of A-38 from Ronne Ice Shelf. (b) Horizontal velocity field describing the direction and magnitude (in  $\text{m a}^{-1}$ ) of iceberg spreading. (c) Distribution of effective deviatoric stress  $\tau$  (in  $\text{kPa}$ ) near the iceberg surface.

### Simulated evolution

For the simulation over five years, starting in October 1998, we chose iceberg A-38B, since A-38A contained pronounced inlets representing significant anomalies of geometry, and their probable influence on ice dynamics is not yet implemented in the model. The simulation period from October 1998 until October 2003 comprises the iceberg's drift from its origin at the Ronne Ice Shelf front west of Berkner Island to its grounding position north east of South Georgia. The forces affecting the iceberg during the grounding phase are not yet considered in the model, therefore, the grounding of the iceberg defines the end of the simulation period. To provide for reliable temporal and spatial resolution, we chose a simulation time step of 0.25 a and a horizontal grid spacing of 2.25 km.

The interaction with ocean and atmosphere under changing environmental conditions during the drift determines the model boundary conditions. Fig 8 a shows the prescribed basal and surface mass balances, which are the

dominant forcing terms of the evolution model, as well as surface temperature as a function of simulation time.

Annual mean surface temperature at the beginning of the drift was set to  $-23.2^{\circ}\text{C}$ , according to measurements at the Filchner-Station (Grosfeld and Thyssen, 1994). As the iceberg reached the latitude of the northern Larsen Ice Shelf section in June 2002, the surface temperature was assumed to be  $-10^{\circ}\text{C}$  based on local measurements (Morris and Vaughan, 2003), and interpolated linearly to the starting temperature. For the following transition from the Weddell Sea to the Scotia Sea, the mean surface temperature of the iceberg rose rapidly up to the melting point, as suggested by ECMWF model data.

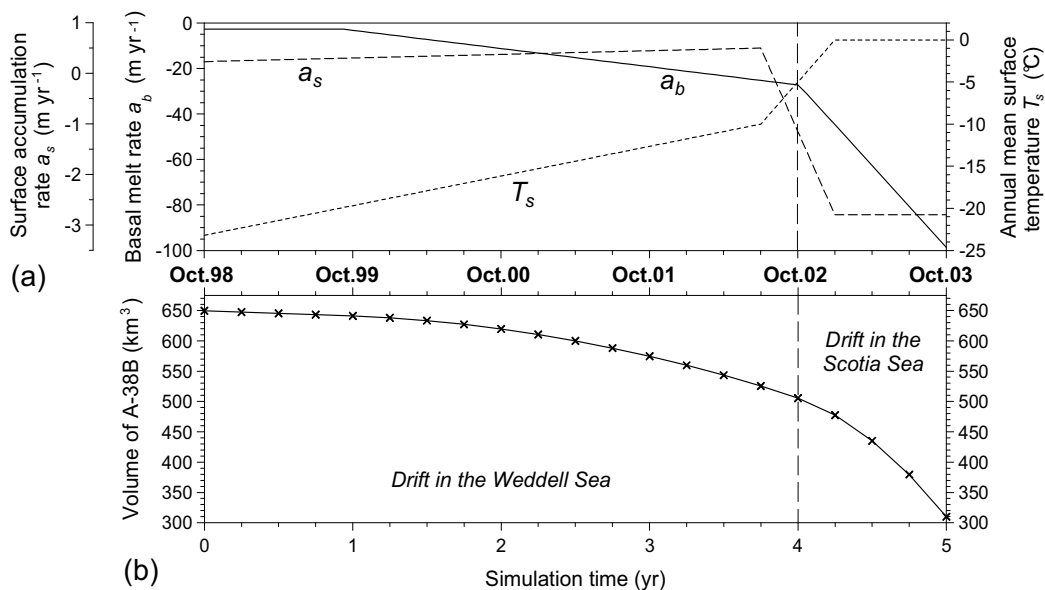


**Fig. 8.** Simulated evolution of large iceberg A-38B between October 1998 and October 2003. (a) Prescribed climate forcing due to temporal variations in surface accumulation, surface temperature, and basal melting. (b) Modeled decrease in iceberg volume. As of austral spring 2002, when A-38B entered the Scotia Sea, the iceberg has been subject to a strong warming and, hence, reinforced decay.

Surface mass balance at the beginning of the drift was set to  $0.233 \text{ m a}^{-1}$  ice equivalent (Graf and others, 1988) and increased to  $0.5 \text{ m a}^{-1}$  ice equivalent by the time the iceberg reached the northern Larsen Ice Shelf in June 2002 (Vaughan and others, 1999). In the Scotia Sea it was estimated by means of the positive degree model (Braithwaite and Olesen, 1989) at  $-2.8 \text{ m a}^{-1}$  ice equivalent. For simplicity we assume that surface ablation processes only cause a mass loss of the iceberg. Melt water formation and associated impact on iceberg evolution from percolation, refreezing or changes of the overall albedo are neglected.

The basal melt rate was based on model data (Lichey and Hellmer, 2001) and estimated at  $2.7 \text{ m a}^{-1}$  for the first year of iceberg drift. During the

following three years basal melting was specified to increase linearly to  $27.2 \text{ m a}^{-1}$ . From October 2002 to October 2003 the basal melt rate was increased dramatically to  $98.6 \text{ m a}^{-1}$  due to stronger currents and warmer ocean water in the Scotia Sea (Schodlok and others, 2005).

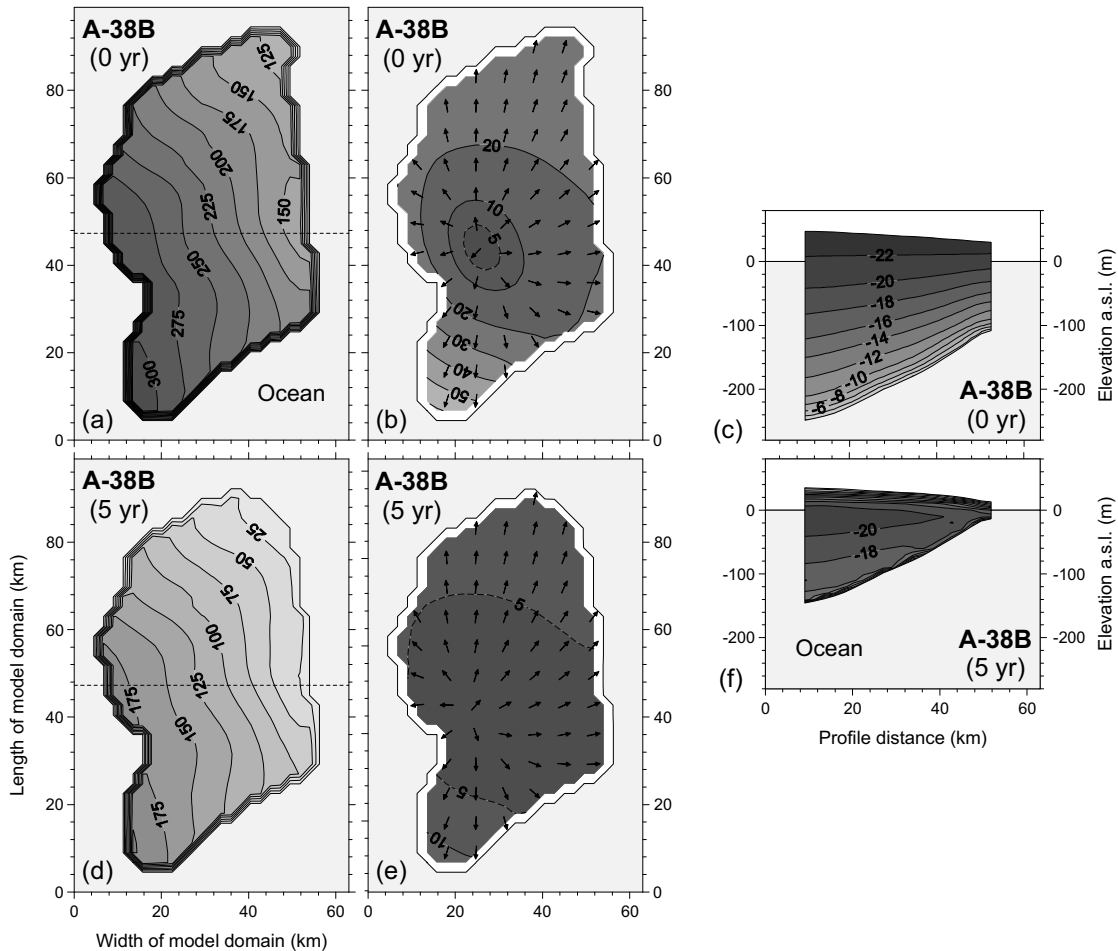


**Fig. 9.** Comparison between the initial and 5-year states of the simulated evolution of large iceberg A-38B: (a), (d) distributions of total ice thickness  $H$  (in m); (b), (e) horizontal velocity fields describing the direction and magnitude (in  $\text{m a}^{-1}$ ) of iceberg spreading; (c), (f) selected vertical cross sections with iceberg temperatures (in  $^{\circ}\text{C}$ ). The profiles are marked with dashed lines in the ice thickness maps. The decrease in iceberg surface area of about  $30 \text{ km}^2$  was imposed by defining a threshold of 10 m for minimum iceberg thickness.

Figure 8 b shows the iceberg volume with respect to simulation time. Owing to the increasing basal mass loss, the iceberg volume decreased continuously with time, leading to a change of volume from  $650 \text{ km}^3$  to  $525 \text{ km}^3$  after 3.75 a. In the following period the erosion accelerated because of the dramatically rising basal melt rates, so that after five years only  $310 \text{ km}^3$  or 48 % of the iceberg still exists. A slight reduction of the surface area occurred only during the last modelled evolution stage. The overall decrease in iceberg thickness from 220 m to 106.3 m was to 95 % (108.0 m) caused by basal melting, 1 % (1.2 m) by surface melting and 4 % (4.5 m) by strain thinning. The mean strain thinning rate of  $0.9 \text{ m a}^{-1}$  is of the same order of magnitude as the estimation of  $0.3 \text{ m a}^{-1}$ , derived from the diagrams shown in Figures 3 a and 4. Model results, therefore, indicate that mass exchange with the ocean is the decisive process in the evolution of the geometry of iceberg A-38B.

Essential iceberg characteristics of the initial and final states are compared in Figure 9. The significant and homogenous decrease of iceberg thickness lead to a slight surface area reduction of  $30 \text{ km}^2$ . Grid cells in which the thickness fell below a threshold of 10 m were neglected, representing a kind of calving criterion. The break-up of A-38B shortly after grounding indicates that the thickness of the observed iceberg may indeed have approached a critical value, at least in some parts (Fig. 6 e). Assuming a basal melt rate of several  $10 \text{ m a}^{-1}$  further on, the final decay of the iceberg A-38B can be expected soon.

A comparison between Figures 9 b and 9 e reveals the sensitivity of horizontal flow to iceberg thickness, not affecting the radial symmetry of the velocity field. The mean velocity of  $4 \text{ m a}^{-1}$  at the end of the simulation is much lower than the initial velocity of about  $20 \text{ m a}^{-1}$ , leading to a negligible strain thinning rate.

Vertical cross sections along the shorter iceberg axis for the initial and final stages (Fig. 9 c, f) demonstrate the considerable impact of environmental conditions on the temperature distribution. Increasing temperatures along the drift track in combination with enhanced melting cause the erosion of the relatively warm basal ice layers and the occurrence of extreme temperature gradients at the top and the bottom of the iceberg. In contrast, temperatures in the inner part remain nearly constant. This special temperature regime of a temperature minimum shifted to the inner part and strong gradients at the boundaries may be important for possible fracture mechanics during the final decay.

## Conclusions

The newly developed iceberg model can be considered as an appropriate tool for investigating large tabular iceberg evolution. Although the current model version considers only one class of elementary influencing processes, a series of basic and advanced simulations yielded important findings on the relative significance of these processes. The model results indicate that mass release to the ocean due to basal melting is the primary cause of change in iceberg geometry during drift, whereas strain thinning associated with iceberg spreading is largely negligible. Effects of iceberg–atmosphere interaction seem to be significant mainly in the late stages of the evolution when the iceberg has approached lower latitudes and strong surface ablation occurs. Thus, it appears that the reliability of our model depends strongly on the accuracy of the forcing data determining basal melting along the drift trajectories. Whether melt rate estimates from ocean models, which currently provide the only available comprehensive datasets, meet these accuracy requirements will remain unclear until suitable observations have been conducted. In particular, we need thickness data from tabular icebergs in the mid- and late stages of evolution to enable detailed validation of model results crucial for changes in iceberg geometry. Satellite image sequences of many large Antarctic icebergs reveal that surface area alteration is typically small over long periods, but they conceal the significant reduction in iceberg volume due to basal erosion.

To include other important processes in iceberg evolution, extension and modification of the model is necessary. A decisive task will be to investigate the role of local geometric anomalies, such as the *mélange*-filled inlets of iceberg A-38A, which had a significant influence on ice dynamics in the pre-calving stage (MacAyeal and others, 1998). Including fracturing on various scales could be a further advancement of the model. This complex problem requires detailed studies of possible fracture mechanisms and an adequate parameterization of the relevant mechanical processes. However, existing studies on fracture formation and propagation in ice shelves already provide a basis for this part of the model adaptations (e.g., Rist and others, 2002; Scambos and others, 2000).

Observations indicate that external forces due to ocean waves, currents and iceberg grounding also affect the evolution and decay of tabular icebergs and therefore will be considered in subsequent model versions.

An extended model version may yield important insights especially for the later stages of iceberg evolution and for the final decay. As drifting large tabular icebergs represent large natural ice bodies under the influence of rapidly changing climatic boundary conditions, such as atmospheric and/or ocean warming, we assume that findings from iceberg evolution simulations will be of interest to the broader community.

## Acknowledgements

The authors would like to express their thanks to M. Puff and J. Schicker of the GKSS Forschungszentrum, Geesthacht, for helpful discussion on potential fracture processes in ice shelves and icebergs. We further thank the reviewers D. R. MacAyeal and J.-B. Minster for valuable comments and suggestions. M. Schodlok supplied the melt rate estimates for iceberg A-38B. The Canadian Space Agency provided the image of Radarsat data of tabular icebergs A-38A and A-38B. The MODIS images were made available by the MODIS Rapid Response Project at NASA/GSFC. ECMWF data used in this project have been obtained by the ECMWF data server. This work was supported by the Deutsche Forschungsgemeinschaft under grant SA 1029/1-1.

## References

- Ballantyne, J. 2002. *A multidecadal study of the number of Antarctic icebergs using scatterometer data*. Report, Brigham Young University, Provo.
- Braithwaite, R.J. and O.B. Olesen. 1989. Calculation of glacier ablation from air temperature, west Greenland. In Oerlemans, J., ed. *Glacier Fluctuations and Climatic Change*, Kluwer, Dordrecht, The Netherlands, 219-233.
- Gladstone, R.M., G.R. Biggs and K.W. Nicholls. 2001. Iceberg trajectory modeling and meltwater injection in the Southern Ocean. *J. Geophys. Res.*, **106**(C9), 19903-19915.
- Graf, W., H. Moser, H. Oerter, O. Reinwarth and W. Stichler. 1988. Accumulation and ice-core studies on Filchner-Ronne Ice Shelf, Antarctica. *Ann. Glaciol.*, **11**, 23-31.
- Grosfeld, K. and F. Thyssen. 1994. Temperature investigation and modeling on the Filchner-Ronne Ice Shelf, Antarctica. *Ann. Glaciol.*, **20**, 377-385.
- Grosfeld, K., M. Schröder, E. Fahrbach, R. Gerdes, and A. Mackensen. 2001. How iceberg calving and grounding change the circulation and hydrography in the Filchner Ice Shelf-Ocean System. *J. Geophys. Res.*, **106**(C5), 9039-9055.
- Grosfeld, K. and H. Sandhäger. 2004. The evolution of a coupled ice shelf-ocean system under different climate states. *Glob. Plan. Change*, **42**, 107-132.
- Jacobs, S.S., H.H. Hellmer, C.S.M. Doake, A. Jenkins and R.M. Frolich. 1992. Melting of ice shelves and the mass balance of Antarctica. *J. Glaciol.*, **38**(130), 375-387.
- Jansen, D., H. Sandhäger and W. Rack. 2005. Evolution of tabular iceberg A-38B, observation and simulation. *Forum for Research into Ice Shelf Processes (FRISP)*, Report, **16**

- Lichey, C. and H.H. Hellmer. 2001. Modeling giant-iceberg drift under the influence of sea ice in the Weddell Sea, Antarctica. *J. Glaciol.*, **47**(158), 452-460.
- MacAyeal, D.R., S. Shabtaie, C.R. Bentley, and S.D. King. 1986. Formulation of ice shelf dynamic boundary conditions in terms of a Coulomb rheology. *J. Geophys. Res.*, **91**(B8), 8177-8191.
- MacAyeal, D.R., E. Rignot and C.L. Hulbe. 1998. Ice-shelf dynamics near the front of the Filchner-Ronne Ice Shelf, Antarctica, revealed by SAR interferometry: model/interferogram comparison. *J. Glaciol.*, **44**(147), 419-428.
- Morris, E.M. and D.G. Vaughan. 2003. Spatial and temporal variation of surface temperature on the Antarctic Peninsula and the limit of viability of ice shelves. In Domack, E., A. Leventer, A. Burnett, R. Bindshadler, P. Convey and M. Kirby, eds. *Antarctic Peninsula Climate Variability – Historical and Paleoenvironmental Perspectives. Ant. Res. Ser.*, **79** (2003). Washington, D.C., American Geophysical Union, 61-68.
- Nøst, O.A. and S. Østerhus. 1998. Impact of grounded icebergs on the hydrographic conditions near the Filchner Ice Shelf, Antarctica. In Jacobs, S.S. and R.F. Weiss, eds. *Ocean, Ice, and Atmosphere: Interactions at the Antarctic Continental Margin. Ant. Res. Ser.*, **75** (1998). Washington, D.C., American Geophysical Union, 269-286.
- Oerter, H., C. Drücker, J. Kipfstuhl, U. Nixdorf and W. Graf. 1992. The Filchner IV campaign and the 320 m deep ice core B15. In Oerter, H., ed. *Filchner Ronne Ice Shelf Programme (FRISP). Report No.6* (1992). Bremerhaven, Alfred Wegener Institute for Polar and Marine Research, 47-53.
- Paterson, W.S.B. 1994. *The Physics of Glaciers*. 3rd ed., Pergamon/Elsevier, Oxford.
- Rignot, E. and D.R. MacAyeal. 1998. Ice-shelf dynamics near the front of the Filchner-Ronne Ice Shelf, Antarctica, revealed by SAR interferometry. *J. Glaciol.*, **44**(147), 405-418.
- Rist, M.A., P.R. Sammonds, H. Oerter and C.S.M. Doake. 2002. Fracture of Antarctic shelf ice. *J. Geophys. Res.*, **107**(0), 10.1029/2000JB000058.
- Sandhäger, H., D.G. Vaughan and A. Lambrecht. 2004. Meteoric, marine and total ice thickness maps of Filchner-Ronne-Schelfeis, Antarctica. In Smedsrud, L.H., comp. *Forum for Research into Ice Shelf Processes (FRISP). Report No.15* (2004). Bergen, Bjerknes Centre for Climate Research, 23-29.
- Scambos, T.A., C. Hulbe, M. Fahnestock and J. Bohlander. 2000. The link between climate warming and break-up of ice shelves in the Antarctic Peninsula. *J. Glaciol.*, **46**(154), 516-530.
- Schodlok, M., H.H. Hellmer, J.N. Schwarz, T. Busche. 2005. On iceberg behaviour: observations, model results and satellite data. *Forum for Research into Ice Shelf Processes (FRISP)*, Report, **16**.
- Thyssen, F., A. Bombosch and H. Sandhäger. 1992. Elevation, ice thickness and structure mark maps of the central part of Filchner-Ronne Ice Shelf. *Polarforsch.*, **62**(1), 17-26, (published in 1993).

- Vaughan, D.G. 1993. Relating the occurrence of crevasses to surface strain rates. *J. Glaciol.*, **39**(132), 255-266.
- Vaughan, D.G., J.L. Bamber, M. Giovinetto, J. Russell and A.P.R. Cooper. 1999. Reassessment of net surface mass balance in Antarctica. *J. Climate*, **12**, 933-946.
- Weertman, J. 1957. Deformation of floating ice shelves. *J. Glaciol.*, **3**(21), 38-42.

# Appendix B

## Poster – Influence of inlets on tabular iceberg evolution

**Daniela Jansen, Henner Sandhäger, W. Rack (2005).**

Abstract is published in: Geophysical research abstracts, Vol. 7, 08174.

### Abstract

Antarctic tabular icebergs contribute significantly to the fresh water input to the Southern Ocean, as they release considerable amounts of melt water during their drift and especially during their final decay. The shape of large Antarctic tabular icebergs is often predetermined by major inlets, which grow at the ice shelf front during decades and can be several tens of kilometres long. Regarding iceberg A-38A, formerly part of iceberg A-38, which calved off the Ronne Ice Shelf in October 1998, its geometry is dominated by two inlets, which are filled by a melange of sea ice, snow and debris from the iceberg margins. We investigated the role of prominent geometry anomalies on tabular iceberg evolution and evaluated the influence of major inlets and inlet filling on iceberg stability by numerical modelling. The finite difference model COMBATIS (Computer-based Antarctic tabular iceberg simulator) is based on the fundamental equation of ice shelf flow and is forced by environmental parameters of the ice-ocean-atmosphere system. The evolution of A-38A has been documented by medium resolution (250 m) optical images from MODIS. The iceberg geometry determined by such images provided the basis for specifying geometrical input data for the model. The simulation of the evolution of iceberg A-38A indicates, that the iceberg thickness decreases by about 100 m mainly due to basal melting during the five year drift period. The temperature profile of the floating ice body is strongly affected by erosion of the relatively warm base and simultaneous warming in the uppermost part. The inlets have only minor effects on iceberg evolution during its drift. However, when iceberg A-38A broke into three fragments in March 2004 during a grounding period near South Georgia Island, their shapes were determined by the positions of the former inlets.

## Introduction

Antarctic tabular icebergs are important active components of the ice-ocean system. They contribute, e.g., significantly to the fresh water input to the Southern Ocean. To investigate the relevance of inherent ice dynamics to iceberg evolution, we developed a numerical model based on the fundamental equations of ice-shelf flow. We found that the change of iceberg geometry during drift is primarily caused by basal melting, whereas strain thinning is largely negligible (Jansen et al., submitted). In the following we present model studies concentrating on the role of iceberg features, which formed in the pre-calving stage. Such features are the inlets in tabular iceberg A-38A. The simulation of its 5-year evolution is also shown.

The tabular iceberg A-38A (Fig. 1), formerly part of A-38, which calved off the Ronne Ice Shelf in October 1998, included two major inlets. They were filled by a melange of sea ice, snow and debris from the iceberg margins. To compute the influence of melange filled inlets we implemented an adequate approach in our model.

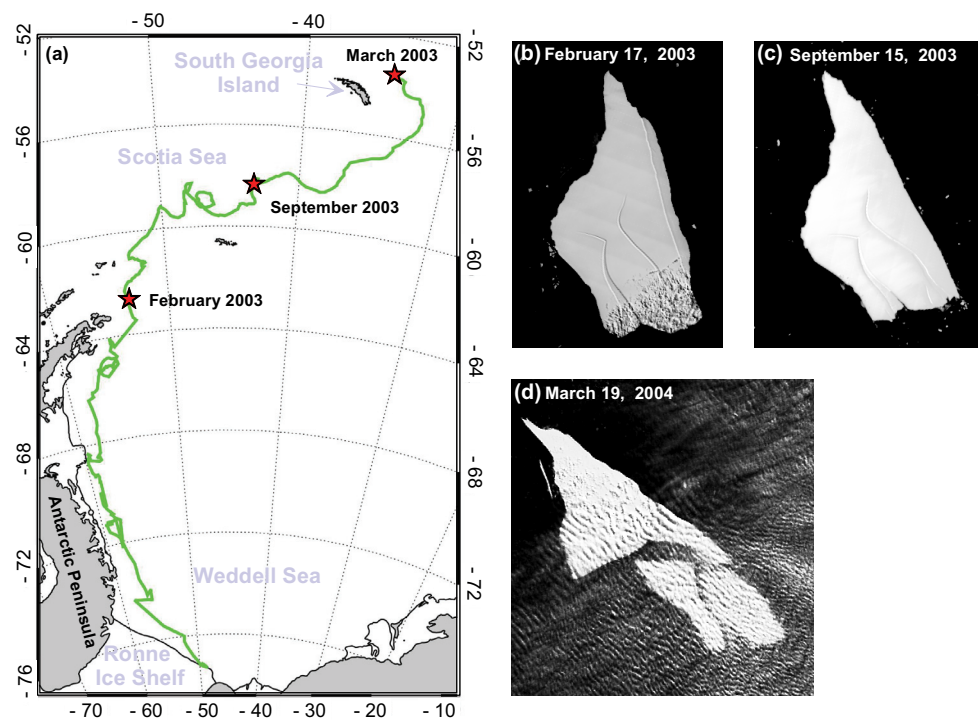


**Figure 1:** (a) Map of Weddell Sea and Scotia Sea with drift trajectory of iceberg A-38A. (b)-(d) Satellite images showing different stages of the A38A evolution (image courtesy MODIS Rapid Response Team, NASA/GSFC). The break up shown in (d) occurred during a grounding period.

## Results

Figure 3 shows the iceberg spreading as derived from three model runs:

- (a) A-38A without inlets (compact iceberg)
- (b) A-38A with water filled inlets
- (c) A-38A with melange filled inlets (thickness 10 m, temperature  $-2\text{ }^{\circ}\text{C}$ )

As expected the spreading of the compact iceberg is associated with radial ice flow, slightly disturbed by the thickness distribution. Velocities are comparatively small. Open inlets lead to a dynamical decoupling of adjacent iceberg parts. Flow directions and ice velocities differ on opposite inlet margins, but changes are rather small compared to the reference run (a). Inlet filling damps the decoupling effect, so that the velocities of iceberg parts separated by inlets now differ primarily due to the non-uniform thickness distribution. Thus, modeled iceberg flow (c) is between solutions (a) and (b).

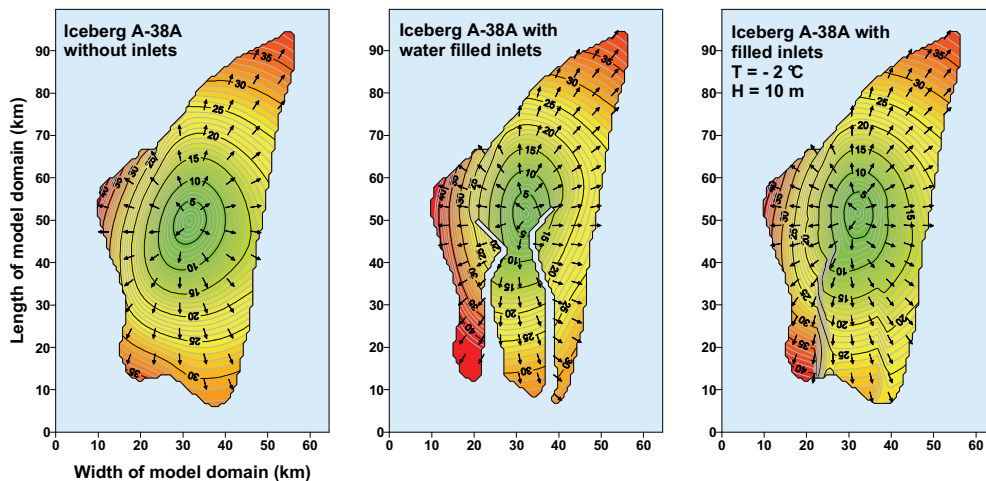


**Figure 3:** Horizontal flow velocities in  $\text{m a}^{-1}$  for different geometries. (a) Compact Iceberg A-38; (b) A-38A with water filled inlets; (c) A-38A with melange filled inlets.

Varying thickness and temperature of the inlet filling has no significant influence on the spreading rate of the iceberg (Fig. 4). A lower temperature increases the damping effect (Fig. 4 a). The results for extremely thick melange layers (Fig. 4 b,c) might be slightly distorted because the numerical restriction  $\hat{H}/H \ll 1$  is no longer fulfilled.

Both, observation and model studies indicate that the evolution of a drifting iceberg is not affected by inlets, although they have significant influence on the ice dynamics in the pre-calving stage (MacAyeal et al., 1998).

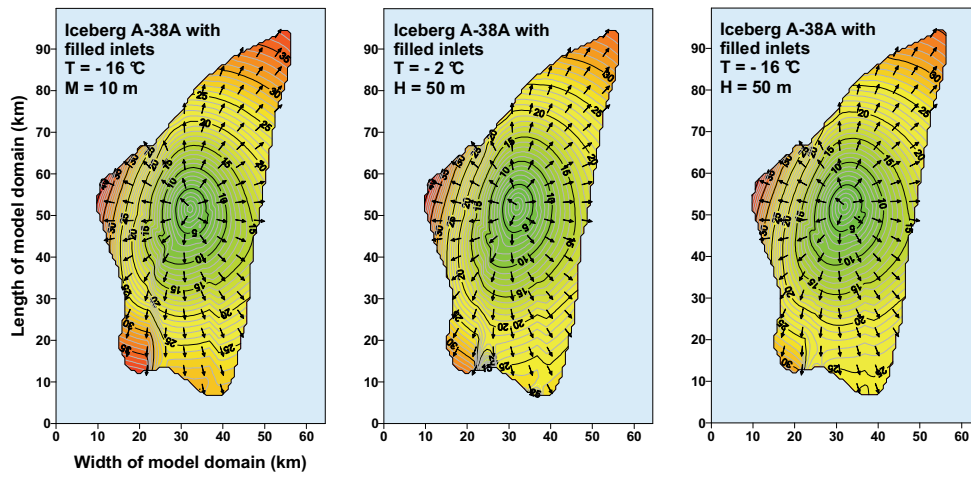


**Figure 4:** Comparison of flow velocity results ( $\text{m a}^{-1}$ ) of model studies with different inlet fillings

## Thickness evolution of A-38A during drift

Figure 5 shows a time dependent simulation of the A-38A evolution during its drift from the Ronne Ice Shelf to its grounding position near South Georgia Island. According to our findings, inlets are ignored. The change in environmental conditions was strongest as of October 2002, when A-38A left the Weddell Sea. Basal melting and surface temperatures increased from  $-20$  to about  $-100 \text{ m a}^{-1}$  and from  $-10$  to  $0 \text{ }^\circ\text{C}$ , respectively. For the entire 5-year period we computed a decrease in mean iceberg thickness of  $113 \text{ m}$ , mainly due to basal melting. The comparison of the initial and the final iceberg configuration reveals the sensitivity of iceberg spreading to iceberg thickness, not affecting the radial symmetry of the velocity field. Strain thinning is negligible in the final evolution stage, when the mean velocity only amounts to about  $4 \text{ m a}^{-1}$ .

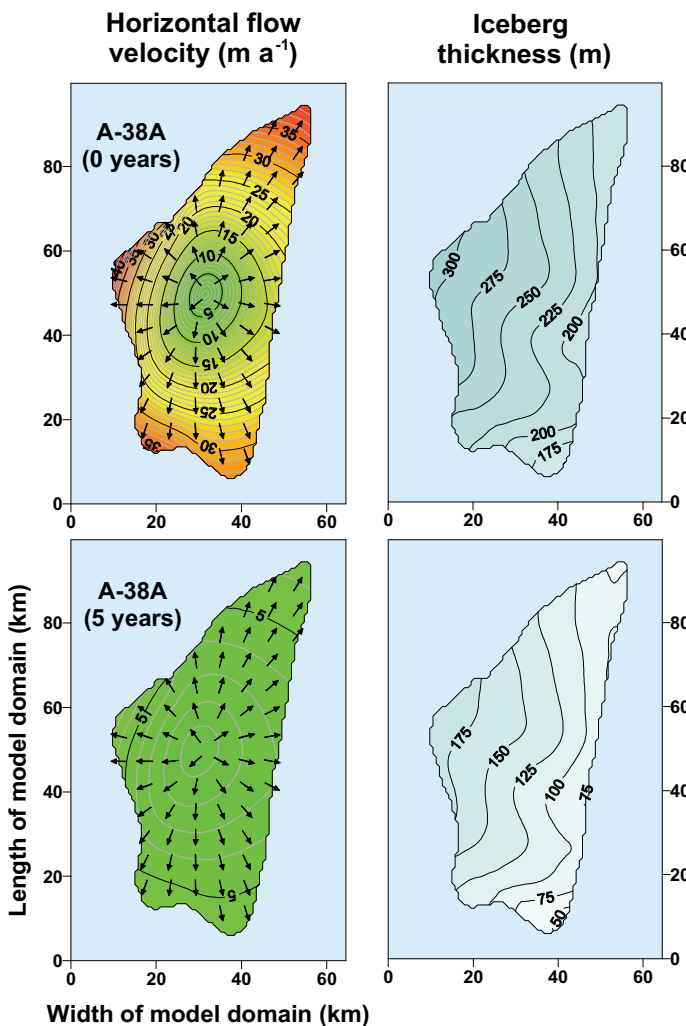


**Figure 5:** Comparison between the initial and 5-year states of the simulated evolution of gigantic iceberg A38A: (a), (c) horizontal flow fields describing the direction and magnitude (in  $\text{m a}^{-1}$ ) of iceberg spreading. (b), (d) distributions of total ice thickness  $H$  (in m).

## Conclusion

- Inlets are irrelevant to dynamics and evolution of iceberg A-38A during drift.
- If external forces affect the iceberg (grounding), inlets govern its break up. Inlet filling seems to be very stable towards warming. The filling can still be detected on satellite imagery of the final grounding stage, when A-38A has thinned by about 48%.
- Regarding the early stage after calving and the final decay, the iceberg evolution is dominated by fracturing on different scales. This will be considered in the forthcoming model version to simulate the entire life cycles of gigantic tabular icebergs like A-38A.

## Acknowledgements

The MODIS data were made available by the MODIS Rapid Response Project at NASA/GSFC. ECMWF data used in this project have been obtained by the ECMWF data server. This work was supported by the Deutsche Forschungsgemeinschaft under grant SA 1029/1-1.

**References** Jansen, D., H. Sandhäger, W. Rack, submitted. Model experiments on large tabular iceberg evolution: ablation and strain thinning. Submitted to Journal of Glaciology.

MacAyeal, D. R., E. Rignot and C. L. Hulbe, 1998. Ice-shelf dynamics near the front of the Filchner-Ronne Ice Shelf, Antarctica, revealed by SAR interferometry: model/interferogram comparison. Journal of Glaciology, 44(147), 419-428.

Weertman, J., 1957. Deformation of floating ice shelves. Journal of Glaciology, 3(21), 38-42.

# Appendix C

## Publication II – Basal melting of A-38B: A physical model constrained by satellite observations

**Daniela Jansen, Michael Schodlok, and Wolfgang Rack (2007).**

Final draft, published in: Remote sensing of Environment, 111(2-3), 195-203.

### Abstract

We observed the large tabular iceberg A-38B in the time period between the calving event at the Ronne Ice Shelf in 1998 until its grounding near South Georgia in 2004 by means of various space-borne sensors. The initial ice thickness was determined by radar altimetry, the iceberg shape from radar imaging and optical instruments. The freeboard change at different stages of the drift was derived from ICESat Laser altimeter profiles. The analysis of the satellite data confirms that the decay of A-38B is governed mainly by basal erosion. We then used a numerical model for simulating iceberg melting and fitted the melt rate by varying the turbulent exchange parameters for temperature ( $\gamma_T$ ) and salt ( $\gamma_S$ ) to match the results obtained by ICESat data. Our results show that the iceberg passed through three melting regimes characterized by iceberg drift velocity: (1) In the Weddell Sea melting conditions are similar to the situation under an ice shelf with strong tidal currents which corresponds to a  $\gamma_T$  of  $1.0 \cdot 10^{-4} \text{ m s}^{-1}$  (2) In the Scotia Sea, where the iceberg drifts unhindered with the ocean current and is surrounded by its own melt water  $\gamma_T$  is  $0.4 \cdot 10^{-4} \text{ m s}^{-1}$ . (3) At the grounding position friction velocity is again high due to tidal currents and  $\gamma_T$  is  $1.8 \cdot 10^{-4} \text{ m s}^{-1}$ .  $\gamma_S$  is set to  $0.00505 \gamma_T$  in all cases. The analysis shows that ICESat GLAS data together with satellite imagery can provide better estimates of turbulent exchange parameters, which is a step forward in improving the knowledge of fresh water input from melting icebergs into the Southern Ocean.

## Introduction

Iceberg calving represents a significant negative term of the mass balance of the Antarctic ice sheet. About 2000 Gt of ice per year, half of this due to large tabular icebergs with a major axis greater than 28 km, serve as a supply of comparatively cold freshwater for the upper Southern Ocean (Jacobs et al., 1992). This exceeds the freshwater flux of about 500 Gt due to basal melting beneath the ice shelves (Jacobs et al., 1992, Gladstone et al., 2001). However, a paucity of information about the amount and the intensity of iceberg melting during their drift means that the precise role of icebergs in the freshwater balance of the Southern Ocean is still poorly understood. Depending on environmental conditions these freshwater reservoirs can be transported far north. In the Weddell Sea, for example, tabular icebergs tend to follow the coastal current along the Antarctic Peninsula into the Antarctic Circumpolar Current (Schodlok et al. 2006, Silva et al. 2006, Gladstone and Bigg, 2002).

Large icebergs can be tracked and/or monitored directly by analysing satellite image sequences gathered with various sensors (e.g., Ballantyne, 2002). The National Ice Center (NIC; Washington D.C., USA) provides an iceberg drift data base for tabular icebergs with a major axis greater than 18.5 km (<http://www.natice.noaa.gov/products/iceberg/index.htm>). The records began in 1976 and were initially based on visible and infrared satellite data, supplemented with ship or aircraft reconnaissance (Long et al., 2002). In the last two decades radar data became more important, as they are also available during polar night and are unaffected by clouds. The Brigham Young University (Provo, UT, USA) provides a complementary data set based exclusively on radar data (Quikscat, NSCAT, SeaWinds, and ERS 1/2; <http://www.scp.byu.edu/data/iceberg/database1.htm>).

Studies for small- to medium-sized icebergs exist on a regional scale. Gladstone and Bigg (2002), tracked this iceberg class by means of ERS SAR (European Remote Sensing Synthetic Aperture Radar) images at the eastern entrance of the Weddell Sea as well as in the south-western Weddell Sea, analysing the drift pattern and iceberg fluxes in these regions. Ground-based studies of iceberg drift by means of GPS buoys for small to medium sized icebergs revealed main drift routes and export patterns out of the Weddell Sea and their dependence on sea-ice concentration (Schodlok et al., 2006).

Lichey and Hellmer (2001) successfully simulated the drift trajectory of giant Antarctic iceberg C-7 and showed the dependence of the iceberg drift on sea-ice cover. Above a threshold of 90 % sea-ice concentration the movement was found to be governed by sea-ice movement while in open water wind and ocean drag as well as Coriolis force were the driving forces. Other iceberg drift models included iceberg thermodynamics and melting: While Gladstone et al. (2001) modelled small iceberg drift trajectories and

the associated freshwater input for the Southern Ocean, Silva et al. (2006) estimated the melt of tabular icebergs assuming idealized iceberg geometry and estimated mean thickness and density. Schodlok et al. (2005) modelled the freshwater input of an idealized iceberg C-7 along its drift path and possible impact on the ecosystem.

Iceberg melting and disintegration is a complex function of iceberg dimension and geometry, ambient water temperature and salinity. At lower latitudes, the freshwater input is expected to increase significantly as the rise in water temperature leads to increased melting and reinforced decay of the iceberg margins. Iceberg drift velocity or the relative velocity of iceberg and ocean is also relevant for the melting intensity as it determines the turbulent exchange between ice and ocean (Jenkins, 1991). The melting is characterized by the turbulent exchange parameters for temperature ( $\gamma_T$ ) and salt ( $\gamma_S$ ) which are functions of the friction velocity (Kader and Yanglom, 1972). In the iceberg melting studies mentioned above a constant value for the turbulent exchange parameters was used for the entire drift. However, the model studies of Jansen et al. (2005) with a basal melting boundary condition based on the work of Schodlok et al. (2005) overestimated the reduction of freeboard height as the comparison with ICESat altimetry available after the study revealed. In this study we aim to combine the information available from satellite-borne sensors for large icebergs with the more detailed ocean stat information offered by modelling, to yield more precise estimates of how much melting occurs in the different oceanographic regimes transited by drifting icebergs. We used ICESat surface height data to obtain realistic estimates for the turbulent exchange between iceberg melt-water and the ocean. For our experiment we chose tabular iceberg A-38B, which calved from the Ronne Ice Shelf in 1998. Melt rates are calculated following the model approach for the basal melting of ice shelves by Hellmer and Olbers (1989). The corresponding freeboard heights are then fitted to the measured ICESat-profiles by varying the turbulent exchange parameters separately for different iceberg drift regimes.

## Boundary settings

### Iceberg drift:

The subject of our investigations is the tabular iceberg A-38B, which calved off the Ronne Ice Shelf in October 1998. During the course of its drift it was exposed to significant changes in environmental conditions such as surface air and water temperature, salinity and sea-ice conditions. Observations and supplementary data are sufficient to provide a reliable description of the iceberg development. The drift track (Fig. 1) consists of NIC Data for the time span between calving and June 1999 and BYU data for the remaining part until 2005.

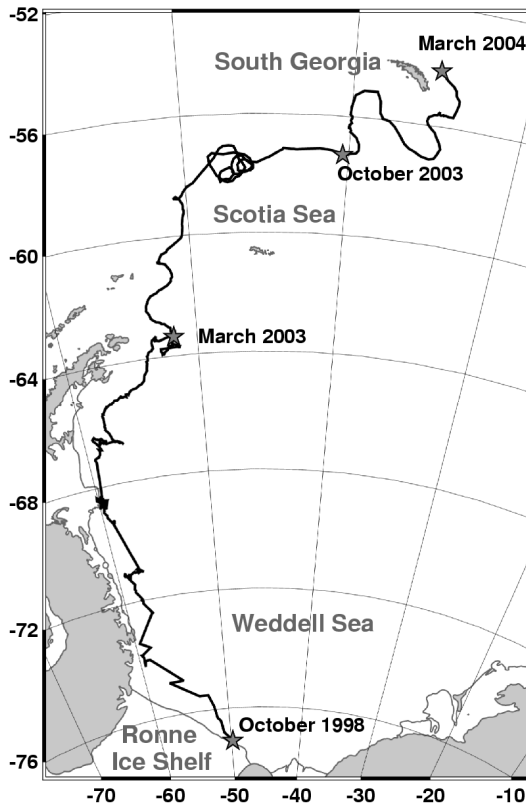


**Figure 1:** Map of the Weddell Sea and the Scotia Sea with drift path of tabular iceberg A-38B. The iceberg positions are derived from the iceberg data base (BYU; NIC).

part drifted with the Antarctic Circumpolar Current (ACC) and was lost to satellite detection in January 2005.

**Iceberg geometry:**

The initial shape of iceberg A-38B was determined from a geocoded RADARSAT (Canadian Space Agency - CSA, 1998) ScanSAR image, which shows the iceberg shortly after calving.

To determine melt rates from satellite altimetry, information about the thickness distribution of the iceberg is needed, as the available profiles are randomly spaced across the iceberg surface. Freeboard changes and the corresponding melt rates can then be derived by comparing the altimetry profiles with the respective sections through the iceberg. We determined the initial iceberg freeboard from Ronne Ice Shelf elevation data (Herzfeld, 2004) recorded prior to the calving event in 1998. This elevation data set is based on ERS-1 radar altimetry between 1991 and 1996. The elevation (above WGS-84) was converted to freeboard by using local minima in front of the ice shelf as a reference assuming these minima to be open water (coastal polynya). An equation of state established for the Ronne Ice Shelf

A-38B drifted with the Weddell Gyre, first westwards towards the Antarctic Peninsula, then along a northward path along the coastline. The drift velocity varied strongly including periods of stagnation. In February 2003, the iceberg reached the tip of the Antarctic Peninsula and proceeded further north, leaving the area of permanent sea ice coverage. In the Scotia Sea, the iceberg accelerated considerably and reached South Georgia in December 2003. It passed the island to the east and grounded in January 2004 northeast of South Georgia. After a few months of grounding the iceberg broke into two nearly equally sized pieces. One part remained grounded and broke into several pieces in August and September 2004. The other

describes the relation between freeboard  $h$  and total ice thickness  $H$  (Sandhäger et al., 2004) for  $H$  greater than 100 m:

$$H = 9.26(h - 15.5 \text{ m}) \quad (1)$$

To represent the gradual change of ice density in the uppermost 100 m we assume an exponential decrease from fully consolidated ice ( $\rho = 917 \text{ kg m}^{-3}$ ) to snow ( $\rho = 300 \text{ kg m}^{-3}$ ) resulting in a correction factor for  $H$  for the thinner parts of the iceberg. We consulted the Filchner Ronne thickness map (Sandhäger et al., 2004) as verification for the resulting ice thickness. This map is derived from direct ice thickness measurements by means of ground-based and airborne radio echo sounding. As it is of lower resolution than the altimetry data it does not show the comparatively steep thickness gradient near the ice shelf edge, but confirms the ice thickness derived from altimetry for the thicker part of A-38B.

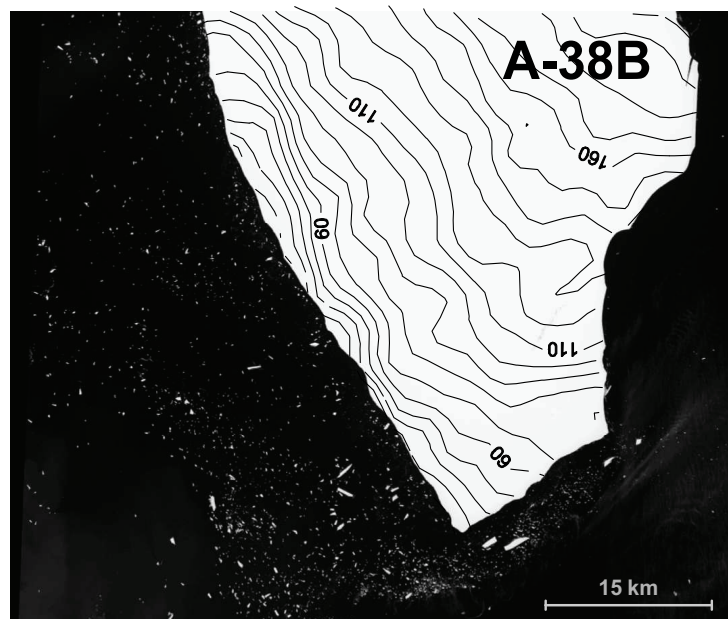


**Figure 2:** ASTER image (ASTER VNIR Band 1) of A-38B during the grounding period near South Georgia together with the ice thickness (m) derived in this study (see text) for the date of image acquisition (January 27, 2004). Many small icebergs show strong calving at the thinner part of the iceberg, whereas little calving is observed at the thicker edge.

Satellite imagery provides information about small-scale calving at the iceberg edges or surface morphology such as melting patterns. Scambos et al. (2005) investigated the edge wasting of several tabular icebergs by means of MODIS (Moderate Resolution Imaging Spectroradiometer) imagery. MODIS images with a resolution of 250 m (Bands 1 and 2) were also used here to provide information about the changes of the shape of A-38B (Table 1). An ASTER (Advanced Spaceborne Emission and Reflection Radiometer, Resolution 25 m) image recorded after the break up during the grounding phase near South Georgia resolves the small-scale calving events at the iceberg margins (Fig. 2). A large number of small icebergs at the thinner side of A-38B indicates an acceleration of decay, whereas very little calving occurs at the thicker iceberg edge. All images were geocoded and the contrast enhanced using automatic procedures of the ENVI Software Package.

**Iceberg freeboard from ICESat data:**

Satellite imagery provides information about the icebergs shape and surface morphology, but altimetry data is necessary to derive thickness changes during its drift. The GLAS Instrument on ICESat measures surface elevation averaged over a 60 m diameter footprint spaced at 172 m intervals along-track with a relative accuracy of  $\pm 15$  cm based on crossover differences (Zwally, 2002). We convert the GLAS elevation into iceberg freeboard by using the water surface of the same track as a reference height. Thus we can consider the relative precision which is 2.1 cm (Shuman et al., 2006) as accuracy for our freeboard measurement. MODIS images of the satellites Terra and Aqua recorded with a time difference of 4 hours were used to estimate the iceberg movement, which was then extrapolated to the ICESat acquisition time to determine the location of the profiles on the iceberg (Scambos et al., 2005). Several elevation profiles of the iceberg A-38B during its drift through Scotia Sea were available, but only three ICESat tracks covered the entire iceberg without data gaps (Table 1). The transition from iceberg to ocean is especially important, as the sea level and the iceberg section length are essential for converting elevation into freeboard and to determine the position of the profile relative to the iceberg. The earliest altimetry data profile was taken in March 2003, which is 4.5 years into the drift and shortly after the iceberg left the Weddell Sea (GLAS06, release 18, Zwally et al., 2003). The next complete profile was recorded in October 2003 during its drift through the Scotia Sea (GLAS13, release 24, Zwally et al., 2003) and the last one during the grounding phase near South Georgia in March 2004, prior to its break up (GLAS13, release 26, Zwally et al., 2004).

**Table 1:** MODIS and GLAS acquisition times and positions of iceberg A-38B.

<b>Date</b>	<b>March 2003 JD 067</b>	<b>October 2003 JD 304</b>	<b>March 2004 JD 079</b>
<b>MODIS Terra acquisition time</b>	<b>11 :40</b>	<b>12 :45</b>	<b>11 :30</b>
<b>MODIS Aqua acquisition Time</b>	<b>17 :15</b>	<b>16 :45</b>	<b>17 :30</b>
<b>GLAS product</b>	<b>Release 18 GLA06</b>	<b>Release 24 GLA13</b>	<b>Release26 GLA13</b>
<b>GLAS acquisition time</b>	<b>17 :46</b>	<b>9 :25</b>	<b>4 :51</b>
<b>Iceberg position</b>	<b>63.0275° S 52.0172° W</b>	<b>56.2172° S 37.4275° W</b>	<b>54.2138° S 35.3061° W</b>

## Melting approach and ocean forcing data

Our previous model studies (Jansen et al., 2005) indicated that strain thinning can be neglected in comparison to melt processes. During the entire drift the strain thinning amounts to 4.5 m, which would correspond to a monthly freeboard change of about 1 cm. The surface ablation was estimated by means of the positive degree model (Braithwaite and Olesen, 1989) and ECMWF temperature data to be 0.23 m water equivalent per month for the iceberg drift in the Scotia Sea. For simplicity we assumed that surface ablation processes caused only a mass loss of the iceberg. Melt-water formation and its associated impact on iceberg freeboard from percolation, refreezing or changes of the overall albedo were neglected as well as accumulation of snow during the drift. The density profile of the iceberg is adapted to the surface melting of snow leading to a change of surface density from  $300 \text{ kg m}^{-3}$  when the iceberg enters the Scotia Sea to about  $400 \text{ kg m}^{-3}$  at the end of simulation.

The basal melting approach is taken from a two dimensional model of ice shelf ocean interaction published by Hellmer and Olbers (1989). The temperature and the salinity at the iceberg base ( $T_B$ ,  $S_B$ ) and the basal melt rate  $\dot{h}$  are calculated from the sea water temperature and salinity ( $T_W$ ,  $S_W$ ) and the parameters for turbulent exchange  $\gamma_T$  and  $\gamma_S$ . Three fundamental equations govern the processes at the ice-ocean boundary, first the balance of heat

(2)

$$\rho_w \cdot c_{pw} \cdot \gamma_T \cdot (T_b - T_w) = \rho_i \cdot L \cdot \dot{h} - \rho_i \cdot c_{pi} \cdot \Delta T \cdot \dot{h}$$

which describes the total heat flux across the interface of ice and ocean as the sum of heat consumed by melting and the conductive heat flow, with  $\rho_w = 1025 \text{ kg m}^{-3}$  and  $\rho_i = 917 \text{ kg m}^{-3}$  denoting the density of sea water and ice,  $c_{pw} = 4180 \text{ J kg}^{-1} \text{ K}^{-1}$  and  $c_{pi} = 2000 \text{ J kg}^{-1} \text{ K}^{-1}$  being the heat capacity of seawater and ice, respectively.  $\Delta T$  represents the temperature gradient within the ice at the iceberg base. The second equation is the balance of salt, which quantifies the total salt flux as dilution caused by the iceberg melt water:

$$\rho \cdot \gamma_S \cdot (S_b - S_w) = \rho_i \cdot S_b \cdot \dot{h} \quad (3)$$

The third equation is the relation of the *in situ* freezing point temperature at the iceberg base to salinity and pressure  $p$ :

$$T_b = a - b \cdot S_b + c \cdot p \quad (4)$$

with the constants  $a = -0.057 \text{ }^\circ\text{C}$ ,  $b = 0.0939 \text{ }^\circ\text{C}$  and  $c = -7.64 \cdot 10^{-2} \text{ }^\circ\text{C MPa}^{-1}$ .

The model input is the temperature and salinity of the ocean and the turbulent exchange coefficients  $\gamma_T$  and  $\gamma_S$ , which are linearly related:

$$\gamma_T = 0.00505 \cdot \gamma_S \quad (5)$$

The equations are solved with respect to  $\dot{h}$  on a model grid with a horizontal resolution of 1.5 km and one vertical layer. The vertical density distribution and its influence on the mean ice column density and thus the freeboard is included (see section “iceberg geometry”).

The model output comprises temperature and salinity at the iceberg base and the melt rate  $\dot{h}$ . The new iceberg thickness is then calculated by subtracting the thickness of the melted ice portion from the original ice thickness. Iceberg freeboard is then calculated according to Equation (1) with a correction term for the changed mean density. A section through the iceberg grid is made at the location of the ICESat profile to compare the freeboard heights. We varied the value of the turbulent exchange coefficient  $\gamma_T$  in steps of  $0.1 \cdot 10^{-4} \text{ m s}^{-1}$  in the range of  $0.2 \cdot 10^{-4} \text{ m s}^{-1}$  to  $2 \cdot 10^{-4} \text{ m s}^{-1}$  until the modelled iceberg freeboard matched the ICESat profiles within the possible accuracy according to the least squares method. The turbulent exchange coefficients are related to the friction velocity  $u^*$  between ice and ocean (Kader and Yanglom, 1972, 1977). To obtain the relative velocity between

iceberg and ocean we estimated a drag coefficient  $c_D$  of 0.0015, following Holland and Jenkins (1999), and calculated the velocity  $u$  with the relation

$$u^*^2 = c_D \cdot u^2 \quad (6)$$

We could not directly derive the turbulent exchange coefficients for the iceberg ocean boundary from friction velocity because of lack of data at the required accuracy. Ocean current velocities for the Weddell Sea and the Scotia Sea from BRIOS (Bremerhaven Regional Ice Ocean Simulations) model data (Timmermann et al., 2002) seem to be too low, as they are slower than the iceberg drift velocities derived from scatterometer data

The oceanic forcing data in the form of annual mean temperature and salinity (Fig. 3 a) were taken from the Hydrographic Atlas of the Southern Ocean (HASO, Olbers et al., 1992) for the Weddell Sea and the Scotia Sea and from a WOCE CTD-profile which was recorded at the later grounding site of iceberg A-38B near South Georgia (WOCE Upper Ocean Thermal, 2006). Sensitivity studies with BRIOS model results (Schodlok et al. 2002, Timmermann et al., 2002) showed that seasonal variations in the temperature and salinity of the ocean during iceberg drift are not significant for the mean monthly melt rate. Interannual variations, for example in the position of the Polar Front seem to play a more important role.

For each month of the iceberg drift a mean basal melt rate was calculated and the iceberg thickness reduced by the resulting value. If the melting at the iceberg bottom had been laterally inhomogeneous, the iceberg surface slope would have been changed during the drift. This behaviour was not observed in the ICESat data, which is probably due to the mixing processes underneath the iceberg. The calving or edge wasting is considered as an ice thickness threshold of 20 m and sidewall melting is neglected as it is minor compared to grid cell size.

## Results

The first model run with a mean  $\gamma_T$  for the entire iceberg drift resulted in an overestimation of the iceberg freeboard. In order to obtain freeboard profiles comparable to ICESat observations, we divided the iceberg drift into three phases characterised by the drift velocity and environmental conditions (Fig. 3 a,b) and adapted  $\gamma_T$  accordingly: (1) In the western Weddell Sea with perennial sea-ice cover the drift is mainly governed by sea ice (Lichey & Hellmer 2001, Schodlok et al. 2006) and includes several phases of stagnation. (2) In the Scotia Sea iceberg A-38B is able to drift freely with the current and also shows a significant increase in drift velocity. (3) In the last three months of the simulation, the iceberg is grounded north of South Georgia. During each of these drift stages an ICESat profile of A-38B was recorded (See section about ICESat data).

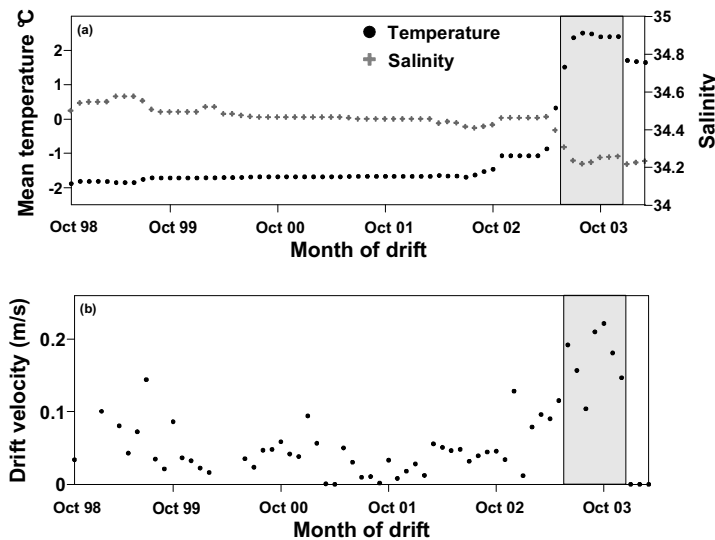


**Figure 3:** (a) Mean ocean temperature and salinity at the iceberg base during its drift, derived from HASO (Olbers et al., 1992). (b) Monthly mean of iceberg drift velocity in  $\text{m s}^{-1}$  derived from Scatterometer data. The grey section marks the borders of the different melting regimes.

In phase (1), i.e. in the Weddell Sea,  $\gamma_T$  was set to  $1 \cdot 10^{-4} \text{ m s}^{-1}$ . Assuming a drag coefficient of 0.0015 (Holland and Jenkins, 1999), the relative velocity between iceberg and ocean emerges at about  $0.23 \text{ m s}^{-1}$ . The corresponding melt rate is low in the first 8 months starting at about 0.1 m per month (Fig. 4 a), during which time the iceberg drifts parallel to the Ronne Ice Shelf front. After A-38B reaches the Antarctic Peninsula and starts drifting northwards with the coastal current, the melting increases to about 0.2 m per month. In the north-western Weddell Sea, the temperature of the upper ocean layers increases further and the melt rate rises to about 0.9 m per month between November 2002 and March 2003. The total mass loss due to basal melting of the iceberg in the Weddell Sea is therefore about 38 Gt in 4.5 years, which is about 8 % of its initial mass of 495 Gt, as calculated from the initial geometry and the mean density for each ice column of the

model grid. The mean iceberg thickness decreased from 191 m at the beginning of the drift to 178 m in March 2003.

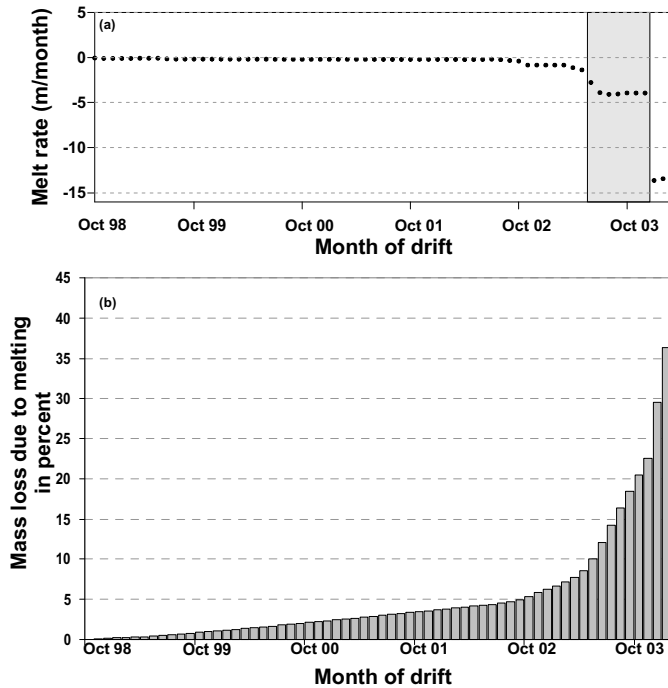


**Figure 4:** (a) Monthly basal melting in m ice equivalent of the iceberg A-38B during its drift. The grey section marks the borders of the different melting regimes. (b) Mass loss during drift in percent.

In the Scotia Sea the iceberg drifts freely with the current and  $\gamma_T$  is set to  $0.4 \cdot 10^{-4} \text{ m s}^{-1}$ , which corresponds to a relative velocity of about  $0.09 \text{ m s}^{-1}$ . Despite the reduction of the turbulent exchange the melt rate rises steeply to about 4 m per month as the ocean temperature is significantly higher than in the Weddell Sea. The total mass loss due to basal melting in the Scotia sea is about 77 Gt during April 2003 to December 2004: about 16 % of the initial mass (Fig. 4 b). Surface melting amounts to about 1 % of the iceberg mass loss, but the associated change in freeboard is about 15 % due to the erosion of the low density ice in the upper part of the iceberg.

During the grounding period near South Georgia we estimate a  $\gamma_T$  of  $1.8 \cdot 10^{-4} \text{ m s}^{-1}$  leading to a relative velocity of about  $0.4 \text{ m s}^{-1}$  and a basal melt rate of about 13.5 m per month. Over this period from January 2004 to March 2004 the iceberg loses about 103 Gt, or 21 % of its initial mass. The mean iceberg thickness after three months of grounding and shortly before the break up is 113 m. The surface melting and associated rise in mean density of the iceberg is responsible for about 10 % of the freeboard change during the grounding period.

The modelled iceberg freeboard profiles (Fig 5,6,7) match the shape of the profiles of A-38B very well, demonstrating the quality of the fit. The freeboard profile for the thicker part of the iceberg, including the sudden change in iceberg surface tilt at the location of ICESat profile km 10, is in better agreement with the ICESat profile than that for the thinner part where a deviation up to 2.5 m is found, corresponding to an overestimation of the total iceberg thickness of about 25 m. This deviation is due to an elevation feature of the initial iceberg geometry marked on the iceberg elevation maps (Fig. 8) which affects all three profiles. The ICESat altimetry data shows a very smooth surface and lateral variations of basal ablation of the iceberg are unlikely. Therefore we assume that the deviation is an error in the initial geometry. The absolute accuracy of our melting approach is limited by the quality of the iceberg geometry, but relative elevation changes from consecutive ICESat profiles enable us to derive melt rates at higher accuracy.

The deviation of ICESat data and modelled freeboard at the iceberg edges for the later stages of the drift is due to very high near-surface melting and the formation of under-water benches, which lead to a hydrostatic imbalance and finally to an upward bending of the iceberg edges (Scambos et al, 2005). These processes are not considered in our melting approach.

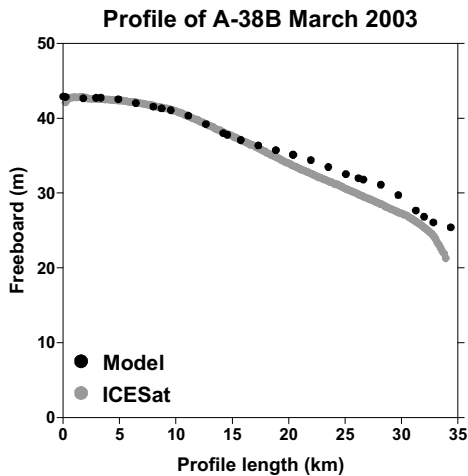


**Figure 5:** Comparison of the ICESat altimetry data (grey line) with melting model results (black dots) for March 3, 2003.

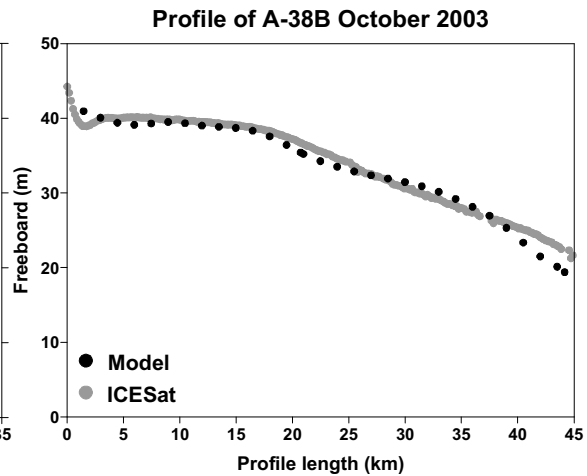


**Figure 6:** Comparison of the ICESat altimetry data (grey line) with melting model results (black dots) for October 31, 2003.

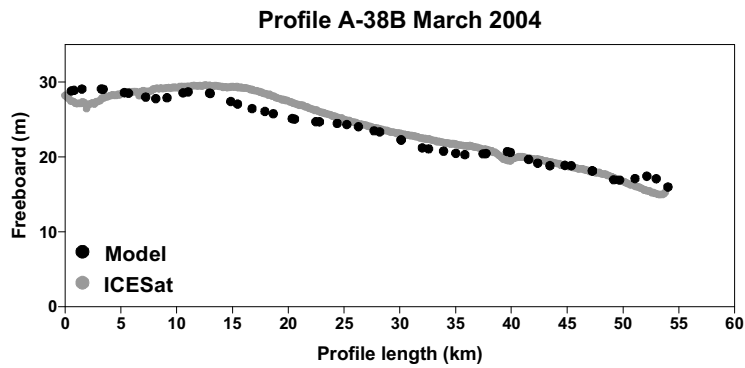


**Figure 7:** Comparison of the ICESat altimetry data (grey line) with melting model results (black dots) for ICESat profile March 19 2004.

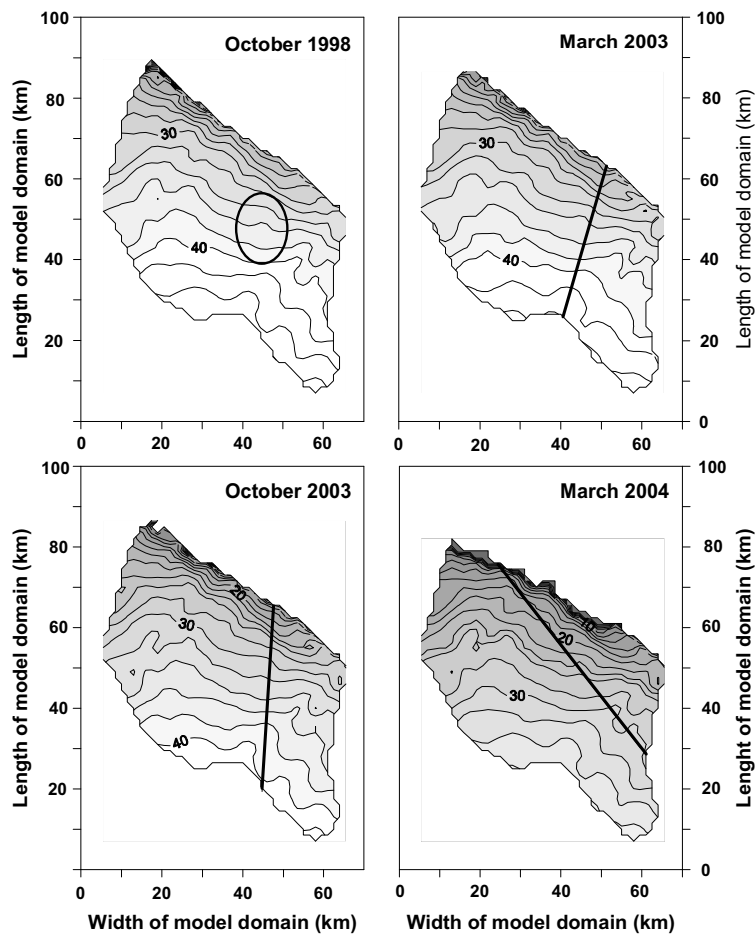


**Figure 8:** Iceberg freeboard maps with ICESat profiles. (a) Initial iceberg geometry derived from Atlas of Antarctica. The circle marks the location of the deviation of the freeboard to the ICESat profiles. (b) Iceberg freeboard March 2003. (c) Iceberg freeboard October 2003. (d) Iceberg freeboard March 2004.

## Discussion

In the Weddell Sea the basal melting conditions of an iceberg are very similar to the situation beneath an ice shelf: In comparison to the thickness of the ice, the water column is thin and the water temperature is low (Fig 3 a). In the western Weddell Sea iceberg drift is slow (about 8 km per day) and, where sea-ice is present at concentrations above a threshold of 93 %, is determined by sea-ice motion (Schodlok et al., 2006). During its northward movement A-38B spent most of its drift on the western continental shelf in sea-ice concentrations exceeding 70 %, including phases of stagnation which probably resulted from grounding. The friction velocity between iceberg and ocean is assumed to be of the same order of magnitude as beneath the ice shelf. We thus estimated the value for  $\gamma_T$  of  $1 \cdot 10^{-4} \text{ m s}^{-1}$  to be appropriate for iceberg melting in the Weddell Sea as it has been applied by, for example, Hellmer and Olbers (1998) for basal melting of ice shelves. The resulting relative velocity of  $0.23 \text{ ms}^{-1}$  between berg and ocean is greater than the current strength of the Weddell Gyre but is consistent with the strong tidal currents in this region (Robertson et al., 1998).

The nearly constant low melt rate derived from our new model approach resulted in a melting of about 8 % of the iceberg's total mass in the Weddell Sea and therefore a transport of 92 % of the reservoir to the ACC.

Silva et al (2005) found a much higher melt rate and melting of 65 % of iceberg mass for geometrically idealized tabular icebergs in the Weddell Sea. This is partly due to their use of a higher turbulent exchange coefficient of  $6 \cdot 10^{-4} \text{ m s}^{-1}$ . However, these results are not directly comparable, as Silva et al. (2005) present a mean of many tabular icebergs.

Schodlok et al. (2005) modelled the melting of tabular iceberg C-7 and derived a mass loss of about 6 % in the Weddell Sea over 1.5 years. They calculated a rise in the monthly melt rate from 0.4 m at the ice shelf front to about 2 m per month at the tip of the Antarctic Peninsula. The deviation from our results, which show the same degree of melting in 4.5 years, can be explained by the eastward offset of the drift path of C-7 in comparison to A-38B, leading the icebergs into different water masses; A-38B drifted through a mixture of Ice Shelf Water (ISW), High Salinity Shelf Water (HSSW) and Antarctic Surface Water (AASW)(e.g. Gordon et al., 1998, Nicholls, 2004) while C-7 transited water masses closer to the Warm Deep Water (WDW) below the surface layer (Fahrbach et al., 1994).

In the Scotia Sea, where the iceberg can drift freely with the ocean current, melting is increased due to a temperature rise of about 3.5 C and a decrease in salinity (Fig. 3 a). Our study leads to a  $\gamma_T$  to  $0.4 \cdot 10^{-4} \text{ m s}^{-1}$ , and therefore the increase of the melt rate is not as large as expected. Due to the low friction velocity between iceberg and ocean the melt water probably builds a plume beneath and around the iceberg which was observed by Foldvik et al. (1980) for smaller icebergs. The basal melt rate of about 4 m per month is

again lower than for the iceberg C-7 which passed the South Orkney Islands to the east and was subject to a basal melt rate of about 7 m per month as calculated by Schodlok et al. (2005).

According to the Hydrographic Atlas of the Southern Ocean (Olbers, 1992) and the WOCE CTD Station, the water temperature is lower at the grounding position to the north of South Georgia than it is in the Scotia Sea. However, the ICESat profile in March 2004 shortly before the break up of the iceberg indicated an increase in melting. The value of  $\gamma_T$  of  $1.8 \cdot 10^{-4} \text{ m s}^{-1}$  required to fit the ICESat profile corresponds to a current velocity of about  $0.4 \text{ m s}^{-1}$ . Strong tidal currents seem to be responsible for the high basal ablation. Tide model results for the Scotia Sea indicate that tidal currents are of the expected order of magnitude in shallow areas like the South Orkney Plateau (Robertson et al., 1998). As bathymetric features around the South Georgia Plateau are similar, we assume that the tidal conditions are comparable. The elevation change during the grounding period shows that a grounded iceberg erodes much faster than a drifting iceberg in the same temperature regime. The grounded iceberg is subject to tidal currents, the cold water plume erodes with the tidal cycle and the temperature leads to an effective melting. In contrast, the drifting iceberg maintains a cold water plume around itself. This also implies that if the iceberg starts to drift again, the decay process would decelerate. The break up of icebergs may be connected to the basal erosion up to the transition zone from consolidated ice to ice of lower density. This explanation could apply to A-38B, as the final break-up occurred after reaching this boundary with a mean thickness of about 100 m.

## Conclusions

The melt rate is sensitive to temperature changes and more importantly sensitive to the turbulent exchange, that is the drift velocity and surrounding ocean currents. The comparison presented here of model and ICESat profiles revealed that it is necessary to take the drift conditions into account and consider separate melting regimes as the use of a mean value  $\gamma_T$  for the entire iceberg drift leads to an overestimation of melt water injection into the Weddell Sea and an underestimation of melting for grounded icebergs. Splitting  $\gamma_T$  into Weddell Sea, Scotia Sea and South Georgia regimes improved the model results for iceberg freeboard and thus melting volume and seems to be an appropriate means to model iceberg decay. This technique could be further improved were more information about the strength of tidal currents available to give better estimations of turbulent exchange. The ICESat GLAS data together with MODIS sequences and other satellite imagery (ERS, RADARSAT, ASTER) proved to be an appropriate means for observing freeboard changes of individual icebergs. If

the initial iceberg geometry is known, a small number of altimetry profiles in sequence provide information about the basal mass loss to the ocean. Because of this requirement this method may only be used for individual icebergs. However, findings about the different melting regimes which result from studies of individual icebergs can be used in simulations in which the entire iceberg population is included. This will contribute to a better estimation of the freshwater input into the Southern Ocean.

## Acknowledgements

We are grateful to R. Timmermann for helpful discussions and for providing part of the BRIOS and HASO data. We also thank H. Sandhäger, who initiated this project. Valuable comments and suggestions of three anonymous reviewers helped to improve the manuscript. We thank the ICESat Science Project and the NSIDC for distribution of the ICESat data (see <http://icesat.gsfc.nasa.gov> and <http://nsidc.org/data/icesat>). The ASTER image was provided by Japanese Aerospace Exploration Agency. The MODIS images were made available by the MODIS Rapid Response Project at NASA/GSFC. The RADARSAT image was provided by the Canadian Space Agency. ECMWF data used in this project have been obtained by the ECMWF data server. This work was supported by the Deutsche Forschungsgemeinschaft under grant SA 1029/1-1.

## References

- Ballantyne, J. (2002), A multidecadal study of the number of Antarctic icebergs using scatterometer data. *In Proceedings of IGARSS'02, Toronto, Ontario, Canada, June 24-28, 2002*, 5, 3029-3031.
- Braithwaite, R.J. and O.B. Olesen (1989), Calculation of glacier ablation from air temperature, west Greenland. In Oerlemans, J. (Ed.), *Glacier Fluctuations and Climatic Change*, Kluwer, Dordrecht, The Netherlands, 219-233.
- Fahrbach, E., R. G. Peterson, G. Rohardt, P. Schlosser, and R. Bayer (1994), Suppression of bottom water formation in the southeastern Weddell Sea. *Deep-Sea Res.*, 41, 389-411.
- Foldvik, A., T. Gammelsrød, Y. Gjessing (1980), Measurements of the radiation temperature of Antarctic icebergs and the surrounding surface water. *Ann. Glaciol.*, 1, 19-22.
- Gladstone, R.M., G.R. Bigg, and K.W. Nicholls (2001), Iceberg trajectory modeling and meltwater injection in the Southern Ocean. *J. Geophys. Res.*, 106(C9), 19903-19915.

- Gordon, A. L. (1998), Western Weddell Sea stratification. In S. S. Jacobs and R. F. Weiss (Eds.), *Ocean, Ice and Atmosphere: Interactions at the Antarctic Continental Margin*, *Antarc. Res. Ser.*, AGU, 215-240.
- Hellmer, H. H. and D. Olbers (1989), A two-dimensional model for the thermohaline circulation under an ice shelf. *Antarctic Science*, 3(4), 433-442.
- Herzfeld, U. C. (2004), *Atlas of Antarctica*. Berlin/Heidelberg: Springer.
- Holland, D. and A. Jenkins (1999), Modeling thermodynamic ice-ocean interactions at the base of an ice shelf. *J. Phys. Oceanogr.*, 29(8 Part 1), 1787-1800.
- Jacobs, S.S., H.H. Hellmer, C.S.M. Doake, A. Jenkins, and R.M. Frolich (1992), Melting of ice shelves and the mass balance of Antarctica. *J. Glaciol.*, 38(130), 375-387.
- Jansen, D., H. Sandhäger, and W. Rack (2005), Model experiments on large tabular iceberg evolution: Ablation and strain thinning. *J. Glaciol.*, 51(174), 363-372.
- Jenkins, A. (1991), A one dimensional Model of Ice Shelf-Ocean Interaction. *J. Geophys. Res.*, 96(C11), 20671-20677.
- Kader, B. A. and A. M. Yaglom (1972), Heat and mass transfer laws for fully turbulent wall flows. *Int. J. Heat Mass Transfer*, 15, 2329-2351.
- Lichey, C. and H.H. Hellmer (2001), Modeling giant-iceberg drift under the influence of sea ice in the Weddell Sea, Antarctica. *J. Glaciol.*, 47(158), 452-460.
- Long, D. G., J. Ballantyne, and C. Bertioia (2002), Is the Number of Icebergs Really Increasing? *EOS, Transactions of the American Geophysical Union*, 83(43), 469 + 474.
- Nicholls, K. W., C. J. Pudsey, and P. Morris (2004), Summertime water masses off the Larsen C Ice Shelf, Antarctica. *Geophys. Res. Lett.*, 31(9), L09309 1-4, doi:10.1029/2004GL019924.
- Olbers, D., V. Gouretzki, G. Seiß, and J. Schröter (1992), *Hydrographic Atlas of the Southern Ocean*. Alfred Wegener Institute for Polar and Marine Research, Bremerhaven.
- Orheim, O. (1980), Physical characteristics and life expectancy of tabular Antarctic icebergs. *Ann. Glaciol.*, 1, 11-18.
- Robertson, R. L., L. Padman, and G. D. Egbert (1998), Tides in the Weddell Sea. In S. S. Jacobs and R. F. Weiss (Eds.), *Ocean, Ice and Atmosphere: Interactions at the Antarctic Continental Margin*, *Antarc. Res. Ser.*, AGU, 341-369.
- Sandhäger, H., D. G. Vaughan, and A. Lambrecht (2004), Meteoric, marine and total ice thickness maps of Filchner-Ronne-Schelfeis, Antarctica. In Smedsrud, L.H. (Ed.), *comp. Forum for Research into Ice Shelf Processes (FRISP)*. Report No.15 (2004). Bergen, Bjerknes Centre for Climate Research, 23-29.
- Scambos, T., O. Sergienko, A. Sargent, D. MacAyeal, and J. Fastook (2005), ICESat profiles of tabular iceberg margins and iceberg breakup at low latitudes. *Geophys. Res. Lett.*, 32, L23S09, doi: 10.1029/2005GL023802.

- Schodlok, M. P., H. H. Hellmer, and A. Beckmann (2002), On the transport, variability and origin of dense water masses crossing the South Scotia Ridge. *Deep Sea Research II*, 49(21), 4807-4829.
- Schodlok, M. P., H. H. Hellmer, J. N. Schwarz, and T. Busche (2005), On iceberg behaviour: observations, model results and satellite data. In Smedsrud, L. H. (Ed.), *comp. Forum for Research into Ice Shelf Processes (FRISP)*, Report No.16 (2005). Bergen, Bjerknes Centre for Climate Research.
- Schodlok, M. P., H. H. Hellmer, G. Rohardt, and E. Fahrbach (2006), Weddell Sea iceberg drift: Five years of observations. *J. Geophys. Res.*, 111, C06018, doi:10.1029/2004JC002661.
- Shuman, C. A., H. J. Zwally, B. E. Schutz, A. C. Brenner, J. P. DiMarzo, V. P. Suchdeo, and H. A. Fricker (2006), ICESat Antarctic elevation data: Preliminary precision and accuracy assessment. *Geophys. Res. Lett.*, 33 (7), Art. No. L07501.
- Silva, T. A. M., G. R. Bigg, and K.W. Nicholls (2006), Contribution of giant icebergs to the Southern Ocean freshwater flux. *J. Geophys. Res.*, 111, C03004, doi:10.1029/2004JC002843.
- Timmermann, R., A. Beckmann, and H. H. Hellmer (2002), Simulations of ice-ocean dynamics in the Weddell Sea. Part 1: Model configuration and validation. *J. Geophys. Res.*, 107 (C03), doi:10.1029/2000JC000741.
- WOCE Upper Ocean Thermal (2006), Physical oceanography at CTD station WOCE\_UOT\_1990\_1503053, *National Oceanographic Data Center, Silver Spring, PANGAEA*, doi:10.1594/PANGAEA.461304
- Zwally, H. J., R. Schutz, C. Bentley, J. Bufton, T. Herring, J. Minster, J. Spinhirne, and R. Thomas (2003, 2004), *GLAS/ICESat L2 Sea Ice Altimetry Data V024 and V026, GLAS/ICESat L1B Global Elevation Data V018*. Boulder, CO: National Snow and Ice Data Center. Digital Media.
- Zwally, H. J., B. Schutz, W. Abdalati, J. Abshire, C. Bentley, A. Brenner, J. Bufton, J. Dezio, D. Hancock, D. Harding, T. Herring, B. Minster, K. Quinn, S. Palm, J. Spinhirne, and R. Thomas (2002). ICESat's laser measurement of polar ice, atmosphere, ocean, and land. *J. Geodyn.*, 34, 405-445.

# Appendix D

## Publication III – Iceberg-generated tremor in the vicinity of South Georgia Island

**Daniela Jansen, Christian Müller.**

Submitted to Geophysical Journal International

### Abstract

We evaluated the seismic records from the HOPE seismic station (King Edward Point, South Georgia Island) for two time periods in which four large Antarctic icebergs reached the island: 1 December 2002 to 31 March 2003 and 1 December 2003 to 29 January 2004. The iceberg movements and small scale drift patterns including rotations were monitored on a day to day basis using MODIS imagery. During the observation periods several seismic tremor events occurred, which could be attributed to the icebergs by 2-D particle motion analysis.

Two key events are described and analysed in this study: **1:** Harmonic tremor occurred when A-43G, a Ronne Ice Shelf iceberg containing a major rift structure, was caught in an eddy at the Southern Antarctic Circumpolar Current Front (SACCF) in the northwest of South Georgia. The signal started with the rotation of the iceberg and is dependent on the position of the rift relative to the current. **2:** The iceberg A-38B caused a high energy tremor with diffuse spectral features when it first collided with the steeply rising sea floor near to the coast of South Georgia Island. Five days later the iceberg finally grounded. The scraping over the seafloor caused a likewise diffuse tremor lasting for two days until the iceberg reached its final position.

In our results harmonic tremor only occurs for iceberg A-43G, which contains a large rift, and only if the rift opening has certain orientations with respect to the surrounding ocean current. The diffuse signals are generated by iceberg collisions and probably represent excitation of elastic modes of the ice masses by stick slip friction.

## 1 Introduction

Large tabular icebergs may be the source of seismic tremor, which is recorded by hydrophones at long distances as T-phases or by land based seismometers as seismic waves which were converted from hydroacoustic signals at the coastal slopes. The duration of iceberg tremor events ranges from seconds to hours or even days. The spectral signature shows a broad variety including monochromatic as well as harmonic signals with well defined overtones and tremor with diffuse spectral peaks. Their contribution to the hydroacoustic background spectrum is of the same order as energy from earthquakes (Talandier et al., 2006)

By evaluating hydroacoustic data from the Polynesian Seismic Network Talandier et al. (2002) first identified a tabular iceberg located in the Ross Sea as the source of tremor events. They attributed the signals, which showed spectral peaks in the range from 3 to 7 Hz, to iceberg B-15B and proposed collisions or scraping along the sea floor as the trigger for these events. As an explanation of the harmonic character of the signal spectrum they offered two possibilities: 1. resonance of elastic modes of the iceberg and 2. oscillation of fluid filled cracks or cavities. The latter was predicated on the analogy to volcanic tremor events and the authors referred to a model proposed by Aki et al. (1977), in which oscillation of fluid filled cracks was triggered by crack opening when a certain pressure threshold is reached.

Chapp et al. (2005), also working with hydrophone data, presented similar results. They found signal clusters lasting from hours to days, with variable spectral peaks and fundamental frequencies ranging from 4 to 10 Hz. The source of the signals correlated with the positions of a large tabular iceberg (B-15D), which drifted westward along Wilkes Land coast during the evaluated period. Additionally, they reported shorter, pulse like signals caused by outlet glaciers at the coast of Wilkes Land. In their discussion of the source mechanism they followed Talandier et al. (2002) and suggested resonance of the iceberg's elastic modes or of fluid filled cavities.

In records of land based seismometers iceberg related tremor events were also found. Müller et al. (2005) presented harmonic tremor including also chaotic phases recorded at the seismological network at Neumayer Base (Dronning Maud Land, Antarctica), which they attributed to the tabular iceberg B-9A. Stressing the analogy to volcanic tremor, they proposed that the flow of water through tunnels or crevasses could be the source of the signal, as fluid-flow through irregular channels with elastic walls can induce oscillation if a critical flow speed is reached (Julian, 1994, 2001). Compared to volcanoes, the physical parameters of the ice-water system are better constrained. Under this aspect icebergs provide a natural laboratory to study fluid-flow induced tremor in detail, as icebergs may be better accessible than volcanic edifices.

However, the variety of spectral features of iceberg tremor indicates the existence of different source mechanisms. Expanding their studies of iceberg generated tremor events in hydroacoustic data Talandier et al. (2006) introduced a classification of tremor events into two families: The first comprised monochromatic events with variable peaks which correlate with stick slip movements between ice masses. The signals allocated to the second family showed a broader spectrum with background activation of a number of resonators and were mostly attributed to freely floating icebergs. Talandier et al. (2006) also pointed out that the position of tremor generating icebergs correlates with the mean position of the Polar Front and discussed hydrostatic imbalances due to different water densities on either side of the front as trigger mechanism of the events.

Although a general conception of the governing mechanism of iceberg tremor can be derived from the articles cited before, some questions remain unanswered, especially regarding the variability of the spectral peaks within a tremor episode connected to stick slip friction, or the originating mechanisms of tremor produced by free floating icebergs.

Our main objective in this study was to investigate the source mechanisms of iceberg generated tremor by combining detailed satellite imagery with the occurrence of tremor derived from the seismological data. In particular, we were interested in the required preconditions for events produced by floating icebergs with respect to iceberg geometry and ocean current situation.

We analyzed tremor events occurring in the vicinity of South Georgia Island, which is located next to the drift routes of tabular icebergs coming from the Weddell Sea and Drake Passage. We monitored the drift of several icebergs which were approaching the island with daily MODIS (MODerate Resolution Imaging Spectrometer) imagery and documented their motions in detail. In this study the focus is on the large tabular icebergs A-43G and A-38B, which originated from the Ronne Ice Shelf. Additionally, we regarded MODIS sea surface temperature (SST) to obtain an overview of the location of oceanic fronts (Moore et al., 1998; Dong et al.2006), which are connected to strong temperature gradients, and thus about the local surface current regime.

The combination of MODIS data and ETOPO2v2 (NOAA, 2006) bathymetry of the island shelf enables classification of the tremor either as scraping event or floating iceberg event, which is also reflected in their spectral signature. To identify iceberg features enabling fluid flow induced elastic interactions inside iceberg cavity structures, we used high resolution RAMP (Radarsat Antarctic Mapping Project, Jezek et al., 1997) images for mapping surficial visible relevant features as trenches, crevasse-, or rift-systems.

## **2 Background information about the involved icebergs and their history**

### **2.1. South Georgia Island**

South Georgia is part of the North Scotia Ridge, the northern boundary of the Scotia Sea. The island is about 160 km long and surrounded by a 50 to 150 km wide shelf, which is shallower than 300 m (e.g. Meredith et al., 2003). Most large tabular icebergs which escape the eastern Weddell Sea at the tip of the Antarctic Peninsula drift towards South Georgia and pass the island with few grounding on the shallow shelf. (e.g. Schodlok et al, 2005) In the following we will introduce the origin and drift routes of several large Antarctic icebergs which reached the island between December 2002 and December 2003.

### **2.2. Iceberg A-38B**

In October 1998, the tabular iceberg A-38 calved off the Ronne Ice Shelf east of Berkner Island, a tabular iceberg with an approximate size of 150 km by 50 km. Shortly after the calving, the iceberg split in two parts of about equal size: A-38A, the formally eastern part of the iceberg, and A-38B (fig. 1), the western part. The ice thickness of A38B varied from about 150 m at the former ice shelf front to 300 m at the calving line according to an ice thickness map of the Ronne Ice Shelf (Sandhäger et al., 2004.). The two icebergs drifted northwards within the Weddell Gyre in direction of the Antarctic Peninsula (fig. 1a). In February 2003 they reached the tip of the Peninsula and proceeded further northeast, leaving the area of permanent sea ice coverage. Leaving the Weddell Sea and the sea ice behind, the icebergs accelerated their drift considerably and reached South Georgia Island by December 2003. Iceberg A-38B which was closer to the island passed South Georgia to the east and then followed the westward current which is predominant in the North of the island near the coast (Meredith et al. 2003). Whereas A-38A drifted further north, A-38B was trapped within the northern boundary current which pushed it towards the topographic rise of South Georgia Island and subsequently grounded it.

### **2.3. Iceberg A-43G**

In May 2000, another calving event happened at the western Ronne Ice Shelf front: A-43 was first recognizable on satellite data on 5 May 2000, probably calved in the afternoon of the previous day. Two days later A-43 broke apart into two pieces, the western part named A-43A, which drifted towards the Antarctic Peninsula and then north alongside the coast. According to ice shelf thickness data (Sandhäger et al., 2004), the mean thickness of the iceberg was about 300 m, with a thinning towards the former ice shelf front. A larger part of the break up of A-43A off Wilkins

Coast in June 2001 was iceberg A-43G with a size of 95 x 15 km (fig. 1c), which left the Weddell Sea in May 2002 and arrived at South Georgia Island by December 2002, passing the island to the East. A-43G remained in deep water but was caught in an eddy in the northwest of the island for several weeks in January and February 2003. Afterwards the iceberg drifted further eastwards and disintegrated in the following months.

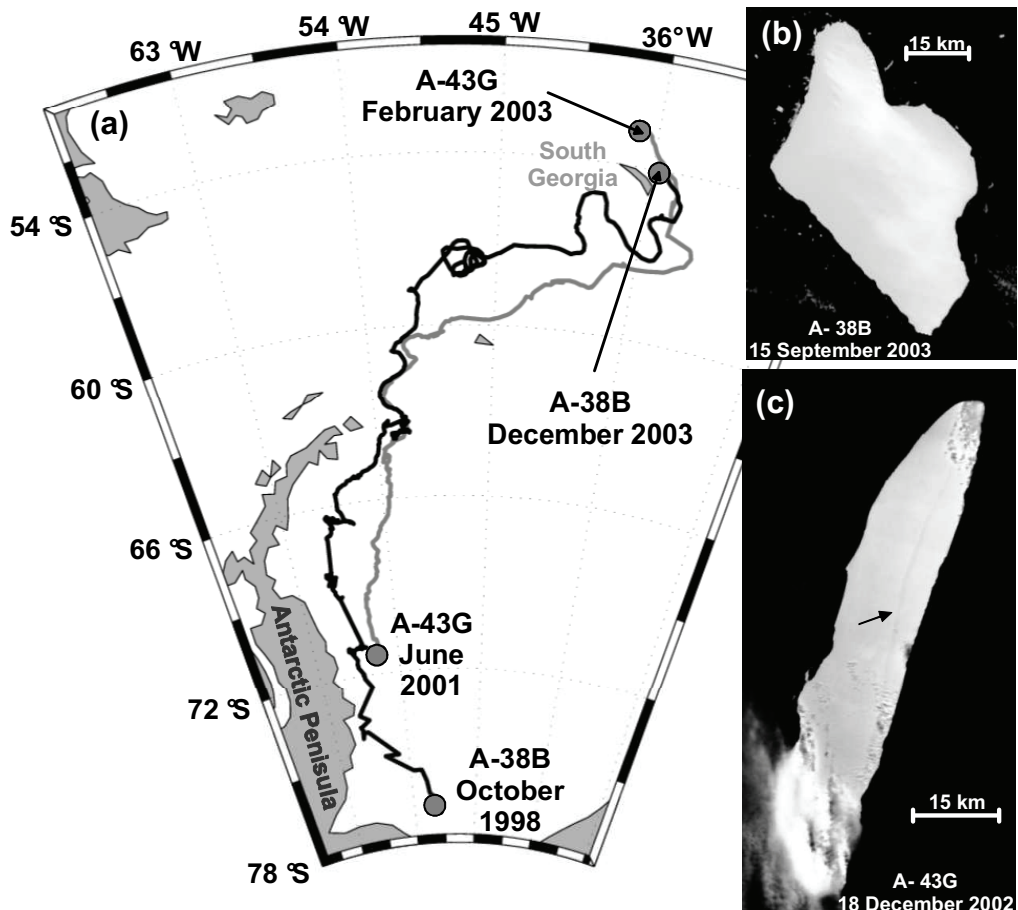


**Figure 1:** (a) Drift route of the tabular icebergs A-38B and A-43G based on QuikScat data from the Antarctic Iceberg Data Base (Long et al., 2002)). (b) MODIS image of A-38B during its drift in the Scotia Sea. (c) MODIS image of A-43G, the arrow indicates the position of the rift.

### 3. Data set and methods

#### 3.1. Seismic data

We evaluated the seismic records from station HOPE (King Edward Point, South Georgia Island, 54.2836 S, 36.4879 W), located at the north coast of the island (Cumberland East Bay). The station which is part of the IRIS (Incorporated Research Institutions for Seismology) network is maintained by the British Antarctic Survey and provides broadband, long period and very long period data streams continuously recorded since December 1996. In this study, we concentrated on two time periods in which several large Antarctic tabular icebergs reached the island: The first period, 1 December 2002 to 31 March 2003 comprises the arrival of B-9A and A-43G, the second period from 1 December 2003 to 29 January 2004 includes the arrival of the icebergs A-38A and A-38B as well as the grounding of the latter. We analysed broadband data from the station's Streckeisen STS-2 triaxial seismometer broad-band data stream recorded with a sample rate of 40 Hz.

For data processing, we used the Matlab signal processing software for calculating moving short time Fourier transforms of the seismograms to identify possible iceberg generated tremor from these spectrograms.

Since the tremor episodes were recorded by a single 3-component seismic station, the determination of the events backazimuths could only be realised by 3-component polarization estimation. We derived the backazimuths of the relevant tremor from 2-D particle motion analysis of the horizontal components.

Depending on whether the icebergs are grounded, sliding over the sea floor or freely floating, different wave types are expected: In the first case seismic P- and S- and surface wave types are generated directly by contact between the iceberg and the seafloor. In the second case, the vibrating iceberg causes oceanic T-Phase waves, which are originally guided hydroacoustic waves. However, when arriving at the continental slope they are refracted and converted to a variety of complex seismic waves (Talandier and Okal, 1998). The recorded seismic signal is then a superposition of body and surface waves originated by hydroacoustic-to-seismic conversion with a composition of wave types depending on the steepness of the continental slope and the orientation of the travelling direction with respect to the slope. In both cases the signal is polarized along or perpendicular to the seismic wave propagation direction and thus allows a simple approach for source detection by 2-D-particle-motion analysis. As there were only few icebergs in the area, the additional degree of non-uniqueness due to the two possible polarization directions is of minor importance in most cases.

### **3.2. Remote sensing**

To verify that tabular icebergs are the source of the recorded tremor events, we have monitored the iceberg drift with daily satellite images derived from the MODIS sensors onboard the NASA Terra and Aqua platforms. With a resolution of 250 m the MODIS Level 1B data gives the opportunity to specify the exact position as well as the small scale drift and rotations of the iceberg. Cloud cover is a limiting factor while analysing MODIS data in the Scotia Sea, but the atmospheric conditions in the relevant time periods allowed to accurately map the iceberg contours on most days. However, geometric anomalies of the iceberg surface (e.g. trenches or rifts) are masked even by a thin veil of clouds. Hence, we had to rely on very few cloudless images to map these structures. As prominent features of the considered icebergs already existed in the pre-calving stages, the RAMP mosaic offered additional information.

To detect when or if the icebergs passed oceanographic front systems we evaluated MODIS Level 3 Sea Surface Temperature (SST) data with a spatial resolution of 4.88 km, derived from the MODIS mid-infrared (IR) and thermal IR channels. As the prevalent cloud cover is problematic when determining SST from space the temporal resolution is here reduced to monthly means.

#### 4. Results: recorded tremor events

In the evaluated time period various tremor events were recorded, with durations ranging from a few minutes to hours or even days. Most of these signals could be attributed to tabular icebergs (tab. 1). Due to primary and secondary ocean swell there was strong noise in the lower part (0.5 Hz to 2 Hz) of the spectrum in all signals. The tremor events had diverse spectral signatures and could be roughly divided into two classes: **1.** Harmonic tremor with well-defined, varying spectral peaks caused by a floating iceberg and **2.** tremor with more diffuse spectral characteristics but still showing prominent spectral bands caused by grounding or icebergs scraping along the island slope. In this study we focussed on several characteristic events (tab. 1).

**Tab. 1:** Recorded tremor events related to tabular icebergs in the evaluated periods.

Year	Julian Day	Start time	Duration [s]	
<b>1. period</b>				
<b>2002</b>	346	07:56	3500	
	349	01:22	2000	
		08:02	1400	
		10:32	2000	
		12:37	8000	
	350	04:08	4000	
	352	05:07	2700	
		11:22	8000	
		17:22	700	
		16:21	11000	
	357	04:10	700	
	<b>2003</b>	3	16:19	10000
		4	02:29	16000
			17:59	7000
6		03:29	8000	
19		19:04	7000	
23		05:14	13000	
27		08:27	2500	
32		00:49	11000	
		17:51	9000	
		01:59	12000	
33		07:19	8000	
		17:31	12000	
		02:45	14000	
34		17:05	18000	
	04:04	12000		
35	18:14	14000		
	11:47	900		
36				
<b>2. period</b>				
<b>2003</b>	347	07:45	5500	
	353	17:44	4000	
	355	00:57	1700	

#### 4.1. December 2002 to February 2003: iceberg A-43G

In December 2002 the tabular iceberg A-43G was approaching South Georgia. The first seismic tremor related to A-43G was recorded on 12 December 2002. It lasted for about one hour and consisted of several short pulses with a constant background tremor with a fundamental frequency of 0.6 Hz and diffuse energy maxima at 2.6 Hz and 5.2 Hz. A MODIS image sequence in combination with ETOPO2 bathymetry data showed that the timing of the first tremor correlated with the icebergs first contact with the island shelf (fig. 2).

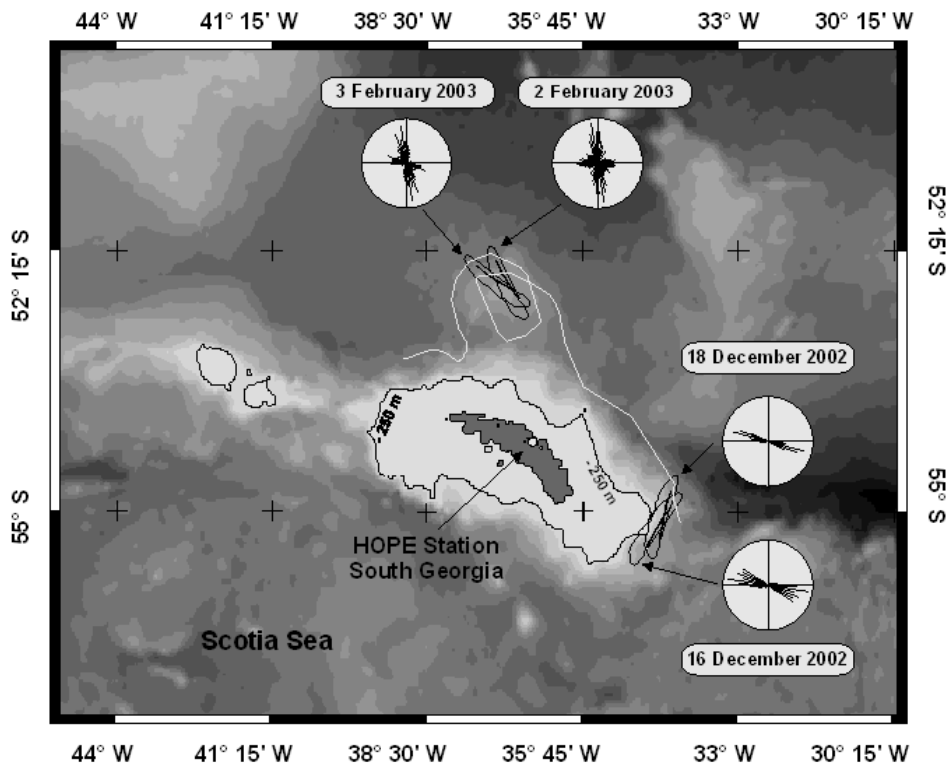


**Figure. 2:** ETOPO2 Bathymetry of the region around South Georgia Island. The grey line indicates the drift route of iceberg A-43G which was derived from MODIS imagery. The circles represent the results from the 2-D particle motion analysis.

In the following days the iceberg further pursued its drift to the north but had to circle an eastward-protruding escarpment of the shallow shelf region. This caused a rotation of the iceberg, which remained close to the island slope. During this period several tremor events were recorded (tab. 1), which changed from the already described pulse-like appearance into continuous signals with downward sliding spectral peaks.

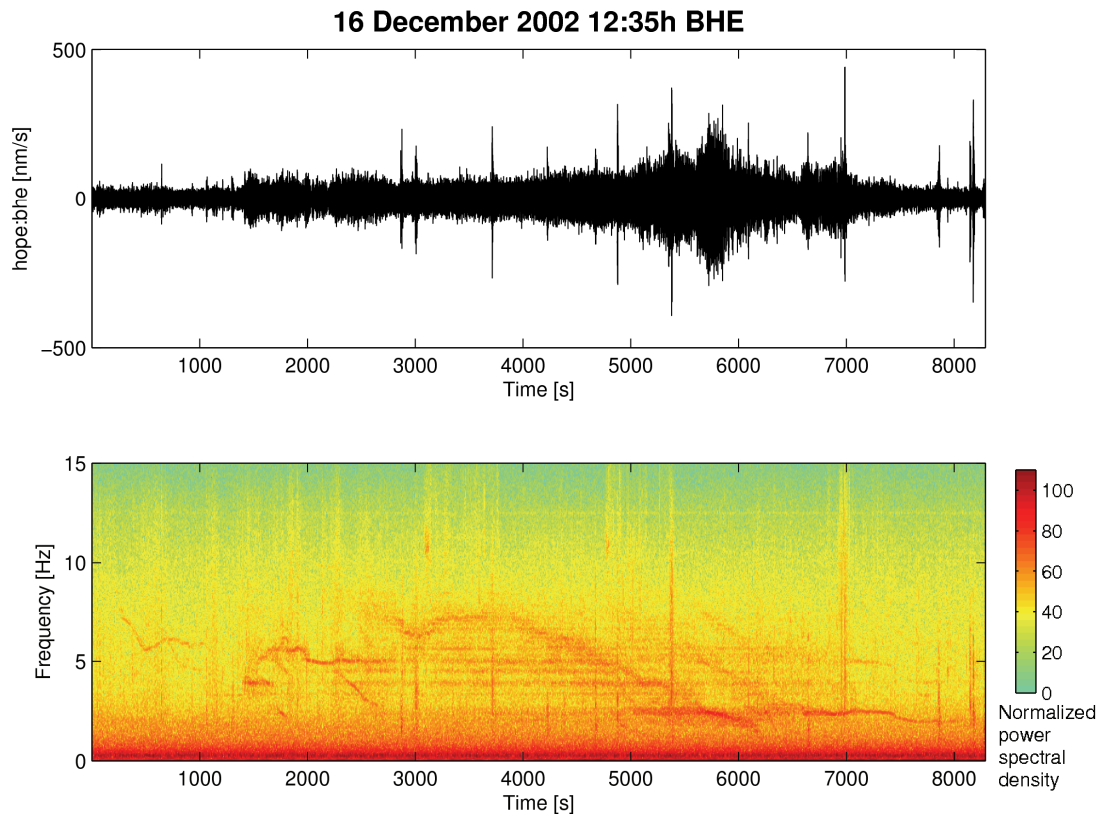


**Figure. 3:** Seismogram and spectrogram of the iceberg tremor on 16 December 2002, caused by iceberg A-43G. The spectrum shows a structured background signal as well as frequency gliding of the spectral peaks.

Some tremor events showed well defined spectral bands with higher variability or even harmonic parts, such as the event on 16 December 2002 (fig. 3). The background sound with the fundamental frequency of about 0.6 Hz was very prominent in all spectrograms and the frequency gliding was gradual in steps of the fundamental mode (fig. 4).

After 19 December, the iceberg moved away from the shelf, turning to the west. Another event was recorded on 23 December, which started monochromatic with a frequency gliding upward from 3 to 4 Hz and developing overtones later. This tremor had a noisy background which was not structured as during the events before. According to ETOPO2 bathymetry the iceberg did not have any contact to the seafloor at that time. The iceberg followed the coastal current northwest along the island shelf during the next days, drifting parallel to its long axis.

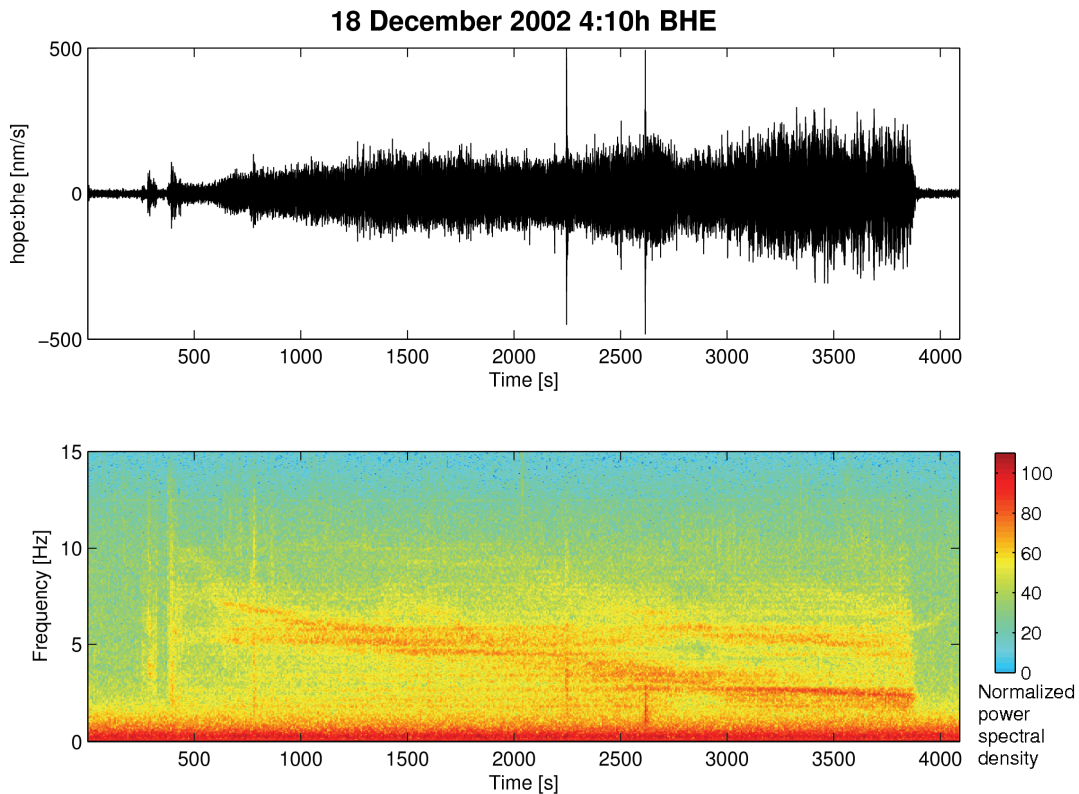


**Figure. 4:** Seismogram and spectrogram of the iceberg tremor on 18 December 2022, caused by iceberg A-43G. The spectral peaks are gliding downwards in steps of the fundamental frequency.

During January and the first week of February 2003, a sequence of harmonic tremor episodes were recorded (tab. 1). In January, the signals were relatively weak and noisy, but after an interval of 10 days of silence several striking events occurred. From 2 February to 4 February, these signals appeared twice a day, lasting for several hours. The spectral structure was dominated by well defined spectral peaks with high variability, gliding up- and downwards continuously between 2 and 5 Hz with a varying number of overtones (fig. 5abc). Additional to the gliding, the frequency changed sporadically in large steps. Occasionally frequency bands were changing independently, leading to intersections of the bands in the spectrogram, suggesting multiple tremor sources inside the iceberg. Particle motion analysis identified A-43G as source of the signal, but in contrast to the so far described tremor where the azimuth of the source could be determined explicitly, an additional  $90^\circ$  polarization orientation existed here, indicating more complicated waveforms.

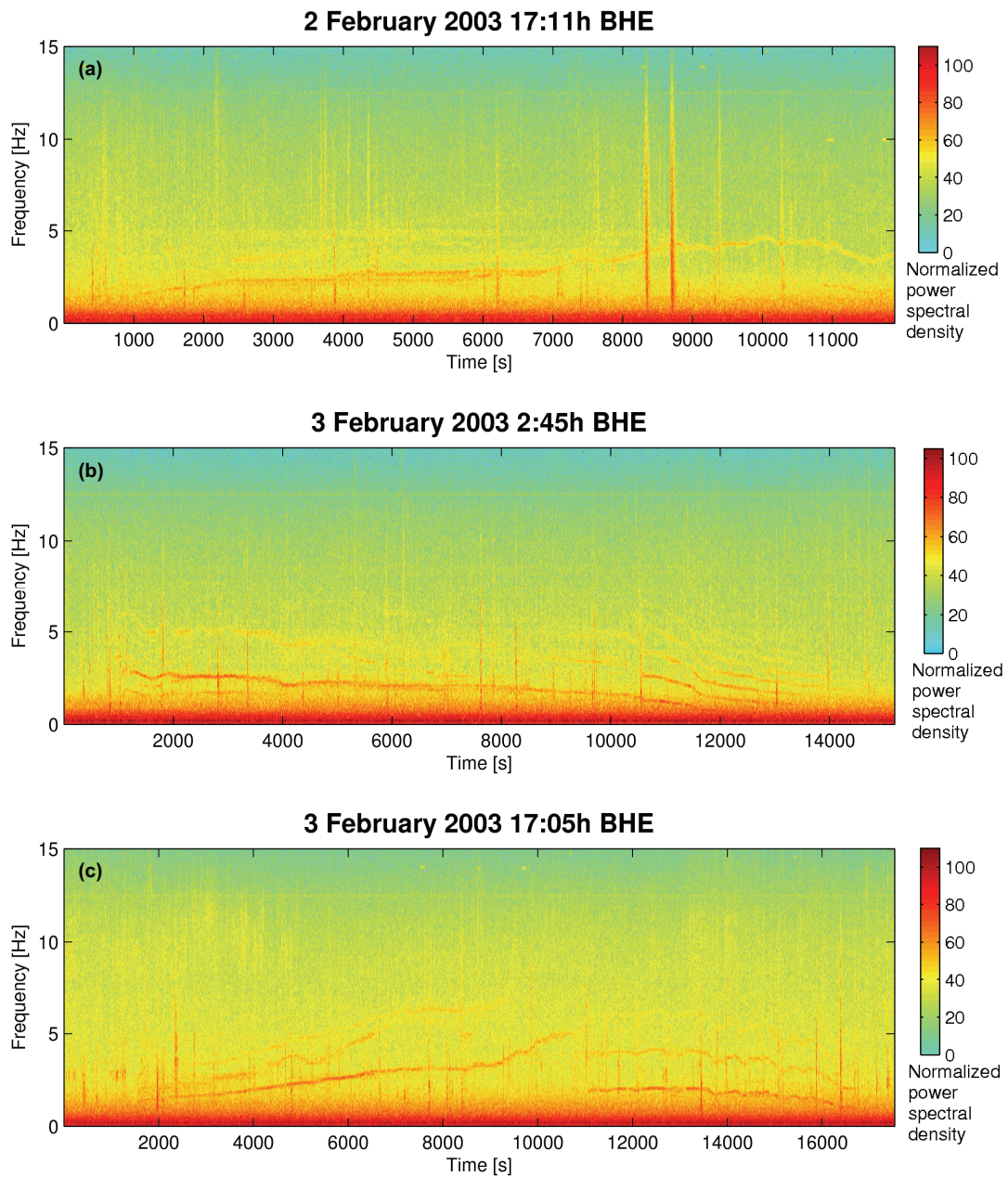


**Figure 5:** Spectrograms of tremor during 2 (a) and 3 (b and c)February, caused by the floating iceberg A-43G. The background signal is missing and the spectral peaks show more variability as in the tremor episodes before.

MODIS images showed that this phase coincided in time with a rotation of the iceberg around its own centre. During 33 days it performed one and a half loop with a diameter similar to its own long axis of 96 km. Sea surface temperature from MODIS indicated a warm core eddy (or ring) at the rotation position (fig. 6). This eddy was located above an about 1800 m high topographic anomaly, the North Georgia Rise (37°W, 52.5°S), which causes a deflection of the Southern Antarctic Circumpolar Current Front (SACCF) in the north of South Georgia, inducing the forming of eddies or rings (e.g. Meredith et al, 2003). The iceberg A-43G was obviously entrained in such an eddy, a process already been observed for other tabular icebergs at this position (Trathan et al, 1997).

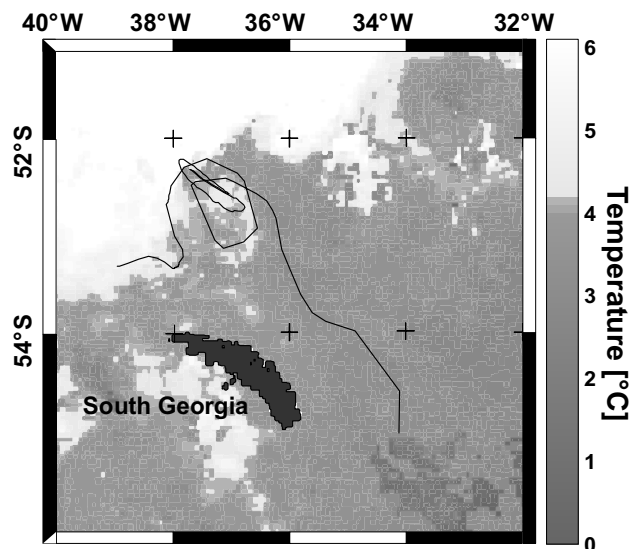


**Figure 6:** Sea surface temperatures (SST) from MODIS thermal channels reveals the eddy in which the iceberg is caught.

After the first 90° of rotation which took about 15 days (probably representing the time it took for dragging the entire iceberg into the eddy), the rotation accelerated to about 25° per day. The silent interval of ten days in the second half of January corresponds to a 180° rotation of the iceberg, starting and ending with a northern position of the long axis. ETOPO2 bathymetry suggested that the iceberg was floating during the entire rotation (fig. 2). In the middle of February 2003, the iceberg left the eddy and turned westwards.

The iceberg B-9A took a different drift route and turned north after passing the island in the east. None of the recorded tremor events was caused by this iceberg, although it produced prominent harmonic tremor (Müller et al., 2005) when passing the Antarctic coast in the eastern Weddell Sea. During the first events B-9A and A-43G had nearly the same azimuth, but as the tremor correlates with the first contact of A-43G with the shelf we assume that A-43G must be the source of the signal.

#### 4.2. December 2003: iceberg A-38B

In December 2003, icebergs A-38A and A-38B reached South Georgia Island and passed the island to the east. A-38A stayed in deep water and farther away from the coast, drifting north on a similar route like B-9A. None of the recorded tremor events could be attributed to this iceberg. The first tremor caused by A-38B was recorded on 13 December, which coincided with a collision of the iceberg with the continental shelf at the same bathymetric feature as one year before iceberg A-43G (fig. 7). According to model results from an iceberg melting model (Jansen et al., 2007) the drought at the colliding part was about 200 m. Thus, the iceberg was repelled from the steep rise and continued its drift.

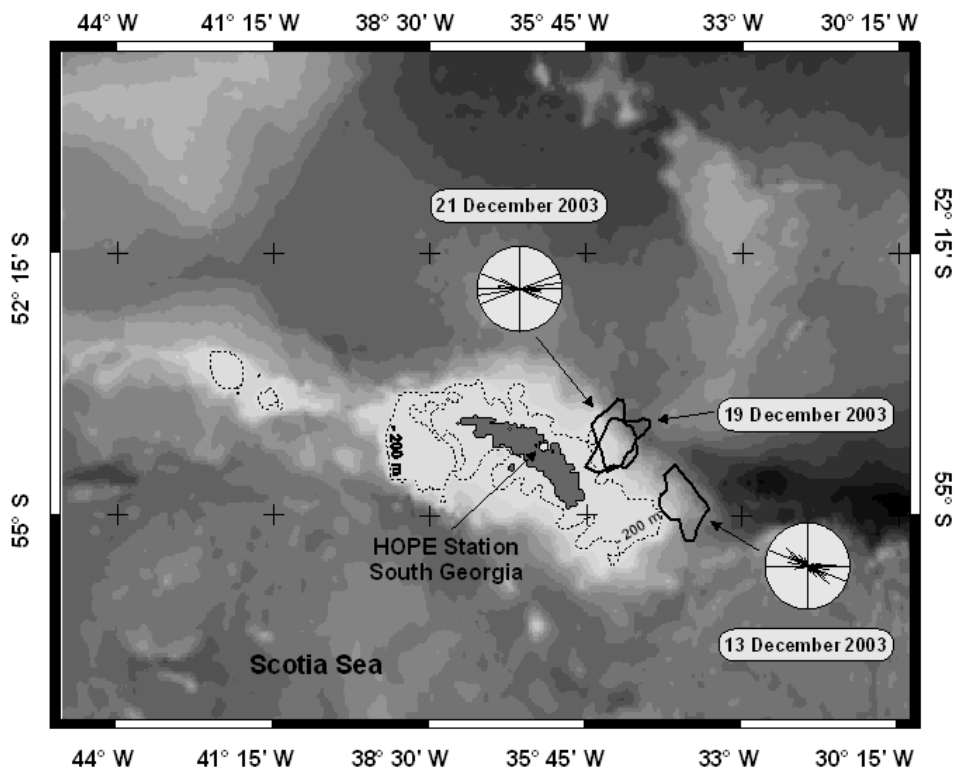


**Figure 7:** ETOPO2 bathymetry of the region around South Georgia Island. The black contours show the position of iceberg A-38B during its collision with the shelf and its grounding. The circles represent the results from the 2-D particle motion analysis.

The event consisted of two phases (fig. 8): it started with weak signals in several frequency bands, followed by increasing amplitudes and a broader and whiter spectrum. Within this period, also downward gliding frequency bands were visible. After 20 minutes the signal amplitude decreased to about 100 nm/s. In the second part of the event the amplitude of the signal rose again to 200 nm/s and the spectrogram showed a frequency band gliding upward from 2 to 5 Hz during 45 minutes. Also noticeable was a

background sound of diffuse frequency bands with a fundamental frequency of about 0.4 Hz.

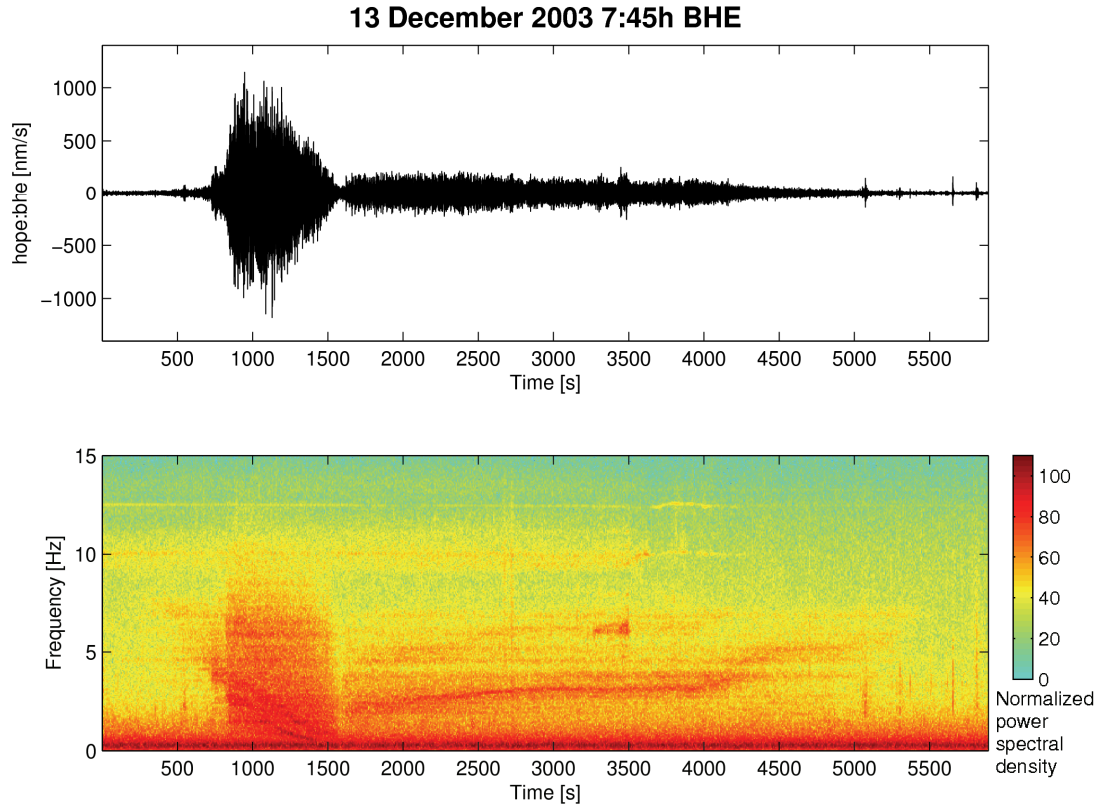


**Figure 8:** Seismogram and spectrogram of the tremor on 13 December 2003, caused by the collision of A-38B with the continental shelf. The two phases differ significantly in amplitude as well as in spectral structure.

The coastal current then pushed the iceberg around the escarpment and forced it into a rotation (fig. 7), so that the iceberg slid onto the shelf with its opposite, much thinner side during the next days. This caused another tremor event with a fundamental frequency of also 0.4 Hz, lasting for 31 hours. The signal had weaker amplitudes than the first, becoming even weaker ( $\sim 200$  nm/s ) after the first hour (fig. 9). The spectrogram showed a stable spectrum which is structured in frequency bands with the fundamental mode of 0.4 Hz. No frequency gliding occurred except in the first hour where the energy seems to drop into the lower frequencies, first concentrated between 3 and 6 Hz, then below 3 Hz. In the following, the energy was distributed equally on overtones of the fundamental frequency. The iceberg stopped when it collided with a small topographic rise, marking the end of the two-day tremor with an earthquake-like signal, after which the tremor terminated abruptly (fig. 10). MODIS images of the following days show that this collision caused the calving of a small iceberg at the

contact point. After the grounding process no more tremor events caused by this iceberg were recorded.

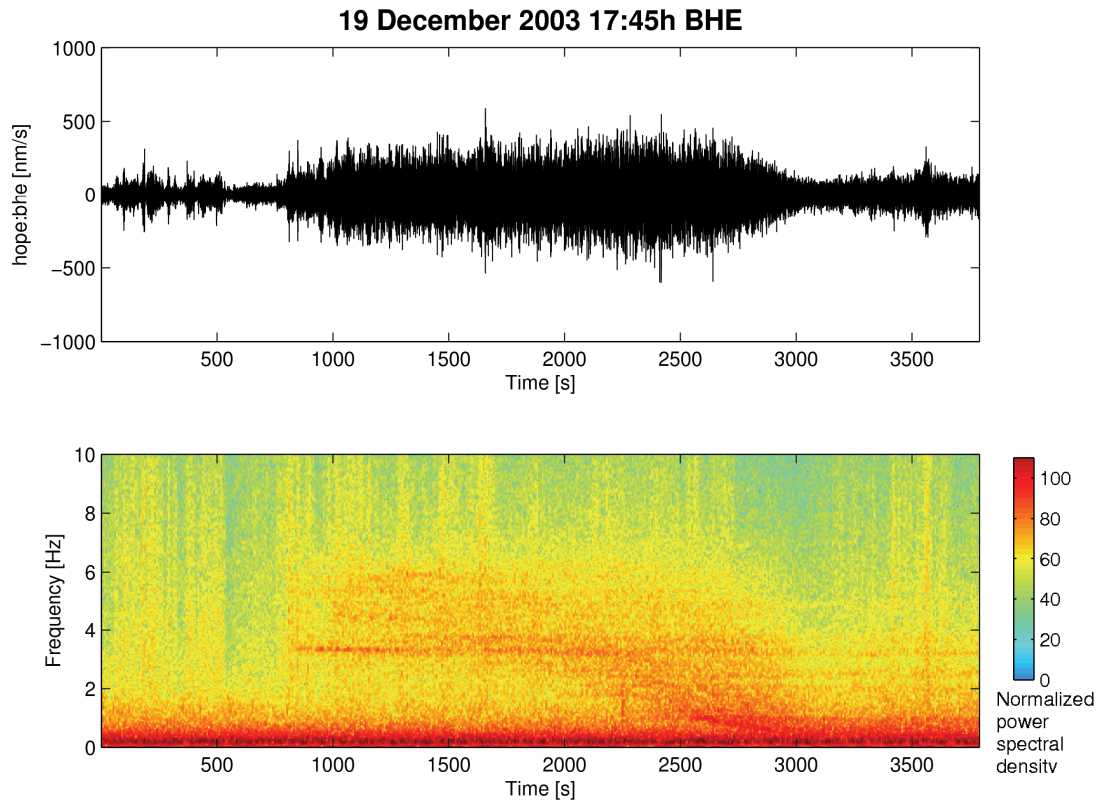


**Figure 9:** Seismogram and spectrogram of the tremor on 19 December 2003, representing the beginning of the grounding of A-38B.

During the evaluated periods, another tabular iceberg was located in the vicinity of South Georgia Island. Iceberg (A-43B) was grounded southwest of the island, almost exactly west of the HOPE station. The grounding of this iceberg also caused tremor during several periods in November and December 2002. Due to its position, particle motion alone did not allow to determine the source of the tremor in case of an east-west azimuth. However, bathymetry and MODIS images showed that the iceberg A-38B and A-43G were colliding with the shelf, whereas A-43B stayed at the same position in the relevant time period. Due to this additional information, we are able to attribute the tremor events to A-38B and A-43G.

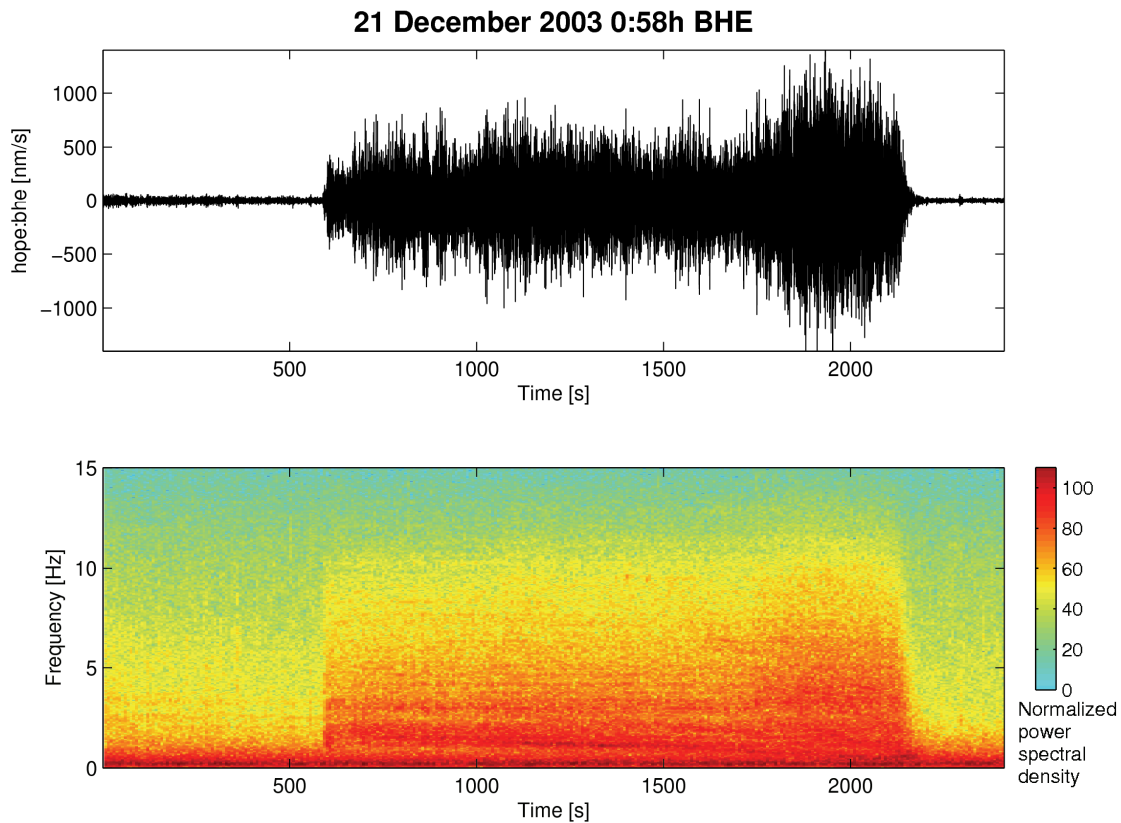


**Figure 10:** Seismogram and spectrogram of the tremor on 19 December 2003, representing the collision with a small topographic anomaly.

## 5. Discussion

By means of satellite imagery and ETOPO2 bathymetry it became clear that the tremor events recorded at HOPE station are generated by freely floating icebergs as well as by grounding icebergs or icebergs sliding along the continental slope, as already proposed by MacAyeal (2004) and Talandier et al. (2006). Depending on the iceberg state, regarding floating or grounding, the spectra of the signal showed different characteristics: In the case of the floating A-43G only few well defined frequency bands existed which were varying in relatively short time scales. The signals from grounding icebergs showed an additional background which was structured in bands of a fundamental frequency.

Curiously, Talandier et al. (2006) reported diffuse signals mostly caused by drifting icebergs and monochromatic and harmonic events to the “Parking Lot”, a group of several big tabular icebergs grounded or stuck in the vicinity of the Mertz Glacier Tongue. A possible explanation may be the different instrumentation: In this study we used land based seismometer

recordings maybe leading to an attenuation of floating iceberg events. Talandier et al. evaluated data from a hydrophone array, possibly not receiving the full signal from collision or grounding events. Moreover, the much greater epicentral distance to the hydrophone array may have an impact on the structure of the received signal. Müller et al. (2005), evaluating data from a land based seismometer array, also associated the more diffuse parts of their B-9 tremor with the iceberg sliding along the continental slope.

### **5.1. Collisions and sliding**

In addition to the already mentioned background sound the ground contact signals show more characteristics which separate them from the floating iceberg events. The amplitudes of these signals and therefore the energy content were significantly higher (1000-1500 nm) and the collision itself caused a superposition of earthquake like frequency structures, leading to a more diffuse or whiter spectrum.

The difference in amplitude also defines the difference between a collision and sliding. This is best explained by analysing the example of the first contact of A-38B with the islands slope (fig. 8). The first part of the signal shows high amplitudes and an earthquake like spectral signature, except for superposed peaks in the lower part of the spectrum, which are gliding down rapidly. We assume that this part represents the collision and rapid slowing down of the iceberg, whereas the second part shows sliding characteristics and originates probably in the icebergs continued motion.

The grounding process a few days later took place in reverse order: As the iceberg slid onto the shelf with its thinner part, first a sliding signal was recorded which endured until the iceberg movement was stopped by a small topographic rise. The corresponding earthquake like signal defines the ending of the grounding process, analogue to the first part of the event described before. The grounding event was lacking a prominent spectral peak. We assume that the much bigger contact plane of iceberg and island shelf due to the grounding leads to a more earthquake like and therefore whiter spectrum.

As we are discussing tremor events generated by icebergs with contact to the solid earth, stick slip friction suggests itself as a source mechanism of the tremor. To explain modulation of the frequency in this case MacAyeal et al (2004) proposed that gliding of natural frequencies are possible for a stick-slip process between two ice masses. In our results also gliding occurred, although only one iceberg was involved. How can the modulation of the spectral peak be explained here? We suppose that the fundamental mode, which is detectable in most sliding and collision connected spectrograms, could play an important role:

When frequency bands are gliding up or down, like in the examples of December 18 2002 and December 13 2003 the gliding is not continuous but

takes place in steps of a fundamental frequency. The frequency differs from 0.4 Hz for iceberg A-38B to 0.6 Hz for iceberg A-43G. This may be connected with the iceberg geometry or thickness: Due to its origin from the western Ronne Ice Shelf A-43G would be expected to be thicker than A-38B (see section 2 ), which calved from the thinner eastern part.

Similar values for fundamental modes were found by Müller et al (2005), who reported a frequency around 0.5 Hz in the B-9A tremor linked to a grounding event. The origin of these modes is unknown, as the frequency is higher than the natural frequency for gravity waves (about 0.05 Hz, MacAyeal, 2006) and too low for vertical shear modes (about 3 Hz or higher, Talandier et al., 2002; Chapp et al., 2005).

According to the stepwise changing of the frequency peak we propose that not the properties of the resonating body are altered during the gliding, but instead the stick slip frequencies, thus exciting different modes of the iceberg. The gliding then could be related to the iceberg's velocity or the changing normal force on the contact plane iceberg/seafloor, which influences the stick-slip-frequency. Monotonous downward gliding of the spectral peak could therefore be interpreted as slowing down of the iceberg. Seismic signals related to stick-slip motion have been observed before in connection with basal sliding of temperate glaciers (VanWormer and Berg, 1973; Weaver and Malone, 1979; Wolf and Davies, 1986, Danesi et al., 2007). The spectra of the reported signals were characterized by monochromatic frequency peaks between 0.5 and 2 Hz. Nevertheless, to our knowledge no detailed analysis of seismic characteristics of grounding icebergs has been reported before.

Upward gliding in connection with ground contact signals was recorded only for the second part of the 13 December 2003 event and may represent the acceleration of the iceberg after it was stopped by the collision before. These ideas are speculative and remain to be investigated further, but we think that they offer a potential explanation for the variability of the spectral peaks.

## **5.2. Floating iceberg: major rifts as a source of the harmonic signal?**

Spectrograms of signals caused by the floating iceberg A-43G at first sight differ significantly from those caused by a collision or by sliding along the continental slope, as the spectral peaks are better defined and more variable. The duration of these harmonic events lasted up to several hours (tab. 1). The prominent tremor episodes in February 2003 occurred during a counter-clockwise rotation of iceberg A-43G. A similar effect has been reported by Talandier et al. (2006) for the tabular iceberg B-19, which also described two loops during a nine month period in austral spring 2002. The detailed monitoring of the icebergs movements and the additional SST data, revealing the size of the eddy in which the iceberg was caught, enables a closer look on the process in our case.

Due to the striking similarity to volcanic tremor events it has been stated before that the harmonic cryosignals originated from coupling of fluid flow through crevasses and cracks within the ice (Müller et al. 2005). In this case the tremor would be triggered by a non-linear process which similarly also governs the excitation mechanism of wind instruments. Such a model was developed by Julian (1994, 2000) which explains flow induced oscillations of pressure driven fluid-flow through narrow channels with elastic channel walls. This non-linear model explains volcanic tremor features as period doubling phenomena, transitions from harmonic to chaotic states and dependencies between oscillation period and tremor amplitudes. Balmforth et al. (2005) elaborated on this model: They expanded Julians considerations by a stability analysis concluding that the system's stability depends on Rayleigh number, the crack's aspect ratio, fluid speeds, and elastic wave speeds. An interesting result predicts tremor appearance for low viscosity fluids preferring magmas with high fluid (water) contents. Rust et al. (2008) proceeded developing these ideas by explaining tremor source mechanisms by flow-induced oscillations from hydrodynamic instabilities, elastic normal modes of the channel walls (Rayleigh waves), the so-called clarinet modes or a combination of those. Clarinet modes or reservoir modes, set by standing waves in an attached reservoir, again suggest the closeness to musical wind instruments. The sound produced in a wind instrument is not simply a combination of frequency produced by a sound generator and a resonator's natural frequency. Sound produced by such instruments is rather the combination of a highly non-linear generator like a clarinet's reed and an attached linear resonator (Fletcher, 2001). In the case of icebergs, the non-linear generating mechanisms is represented by Julian/Balmforth like generators coupled to the resonating systems like the whole iceberg's body or parts of it like the elastic channel's walls. In a non-linear system, the governing frequencies are not necessarily coupled to the geometry of the vibrating system. Thus, the non-linear generator enables phenomena like frequency gliding and does not necessarily imply changes in dimensions.

In the case of A-43G, a pressure oscillation with a frequency proportional to the current velocity might occur if the fluid flow is directed onto a sharp edge like a clarinet's reed. Iceberg tremor would then be related to the local current situation at the opening of a rift or crack. Our results support this approach, as the harmonic tremor events associated with A-43G, which contained a major rift, occurred when the iceberg entered different current regimes.

The first signal with harmonic elements was recorded in December 2002, when the iceberg passed South Georgia in the east. The current in the north of South Georgia is directed westwards and therefore the iceberg is pushed around, with the current directed onto the iceberg's edge with the opening of the rift.

The harmonic tremor occurring in January and February 2003 was also connected with a special current regime: The iceberg was rotating around its own centre. The eddy in which the iceberg was caught had similar dimensions as the icebergs long axis, leading to different relative current vectors at both iceberg's ends. Due to the inertia of the iceberg, relative velocities between iceberg motion and current velocity become possible, enabling a flux through the opening of the rift (fig. 11). The tremor events are therefore triggered by the relation of velocity and direction of the iceberg and the current at the position of the crack opening. Variations in the relative current velocities would lead to frequency gliding, whereas in silent phases the iceberg would be expected to drift with the same velocity as the current. As the SST only gives the positions of fronts and the possible borders of current regimes, we are not able to make quantitative statements about the flow velocities. However, the strong current variation at the spatial scale of the iceberg's size as a precondition for tremor agrees well with the fact that only large icebergs produce these signals.

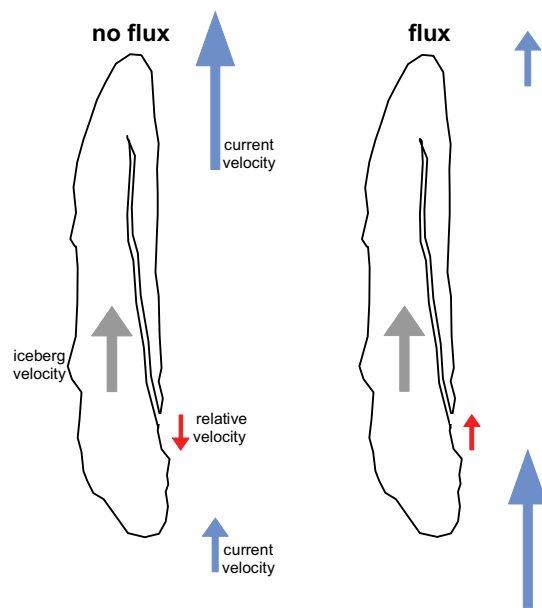


**Figure 11:** Illustration of the ocean current regime required to produce tremor of icebergs with rifts or crevasses (e.g. A-43G)

Another example of iceberg tremor which could be explained by this approach are the tremor episodes reported by Müller et al (2005), generated by iceberg B-9A, which also contained major rift systems. The iceberg was forced into rotation by occasional contact with the continental shelf, altering the position of the rift opening relative to the current. Also iceberg C-18A when passing Western Dronning Maud Land was identified as the source of a tremor after a rotation, exposing the entrance of a trench which is visible in radar data to the coastal current (2007, not published).

Whether the pressure oscillations due to the flow through the rift opening directly create the seismic signals or whether there is a resonance mechanism involved or a combination of both as speculated above remains an open question.

## 6. Summary

We analysed tremor events generated by tabular icebergs in the vicinity of South Georgia Island. By the combination of MODIS satellite imagery and ETOPO2 bathymetry data, we were able to differentiate between events which were associated with contact to the solid earth and events originating from a floating iceberg. These two categories showed different characteristics in their signal spectrograms:

1. The iceberg's grounding or sliding along the continental slope for both icebergs is associated with diffuse tremor events with a background sound structured in frequency bands. The bands appear to be multiples of a fundamental mode, which amounts about 0.6 Hz for iceberg A-43G and 0.4 Hz for A-38B. Its origin is not yet known, but the differing values may indicate a relation to the iceberg's shape or thickness. Superposed onto this background gliding spectral peaks occur. We assume that this is the effect of the stick slip process between iceberg and island slope, with the frequency proportional to the velocity of the iceberg.

2. Harmonic tremor with only a few pronounced, variable frequency maxima occur exclusively for the floating iceberg A-43G, which contains a major rift structure. We suppose that the timing of the tremor events is associated with a particular current regime, which enables a flux through the rift opening. The excitation process of the tremor could then be explained by the coupling of hydrodynamic instabilities with the reservoir modes of the rift channel or oscillations of the channel walls, in analogy to tremor excitation in volcanic systems.

For the first time, the development of iceberg generated tremor with different origin mechanisms could be evaluated by simultaneously combining seismic data, satellite observations of the iceberg's movements and oceanographic considerations about the flow regimes involved. Thus, these observations set novel limits to conceptions of iceberg tremor generating models.

## Acknowledgements

The seismic broadband data was provided by IRIS (see <http://www.iris.edu/data/data.htm>). We thank the ICESat Science Project and the NSIDC for distribution of the ICESat data (see <http://icesat.gsfc.nasa.gov> and <http://nsidc.org/data/icesat>). The MODIS images were made available by the MODIS Rapid Response Project at NASA/GSFC. This work was supported by the Deutsche Forschungsgemeinschaft under grant SA 1029/1-1.

## References

- Aki, K., M.Fehler., and S. Das, 1977. Source mechanism of volcanic tremor; fluid-driven crack models and their application to the 1963 Kilauea eruption, *J. Volcanol. Geotherm. Res.*, 2, 259-287.
- Balmforth, N.J., R.V. Craster, and A.C. Rust, 2005. Instability in flow through elastic conduits and volcanic tremor, *J. Fluid Mech.*, 527, 353-377.
- Chapp, E., D.R. Bohnenstiehl, and M. Tolstoy, 2005. Sound-channel observations of ice-generated tremor in the Indian Ocean. *Geochemistry Geophysics Geosystems*, 6(6).
- Danesi, S., S. Bannister, and A. Morelli, 2006. Repeating earthquakes from rupture of an asperity under an Antarctic outlet glacier. *Earth Planet. Sci. Lett*, 253(1-2), 151-158.
- Dong, S., J. Sprintall, and S.T. Gille, 2006. Location of the Polar Front from AMSR-E satellite sea surface measurements. *J. Phys. Oceanogr.*, 36, 2075-2089.
- Fletcher, N.H., 2001. The nonlinear physics of music instruments, *Rep. Prog. Phys.*, 62, 723-764.
- Jansen, D., M.P. Schodlok, and W. Rack, 2007. Basal melting of A38B: aphysical model constrained by satellite observations. *Remote Sensing of the Environment*
- Jezek, K. and RAMP Product Team, 1997. RAMP AMM-1 SAR image mosaic of Antarctica. Fairbanks, AK: Alaska SAR Facility, in association with the National Snow and Ice Data Center, Boulder, CO. Digital media.
- Julian, B.R., 1994. Volcanic tremor: Nonlinear excitation by fluid flow. *J. Geophys. Res.*, 99(B6), 11859-11877.
- Julian, B.R., 2000. Period doubling and other nonlinear phenomena in volcanic earthquakes and tremor, *J. Volc. Geoth. Res.*, 101, 19-26.
- Long, D.G., J. Ballantyne, and C. Bertoina, 2002. Is the number of Antarctic icebergs really increasing?, *Eos*, 83, 469.
- MacAyeal, D.R., E.A. Okal, and the SOUTHERNBERG Team, 2004. An in-situ investigation of the seismic symphony of iceberg C16, Ross Sea, Antarctica. *Eos, Trans. Am. geophys. Un.*, 85(47), F463 [abstract].

- MacAyeal, D.R., E.A. Okal, R.C. Aster, J.N. Bassis, K.M. Brunt, L. MacCathles, R. Drucker, H.A. Fricker, Y-J. Kim, S. Martin, M.H. Okal, O.V. Sergienko, M.P. Sponsler, and J.E. Thom, 2006. Transoceanic wave propagation links iceberg calving margins of Antarctica with storms in tropics and Northern Hemisphere. *Geophys. Res. Lett.*, 33, doi: 10.1029/2006GL027235.
- Meredith, M.P., J.L. Watkins, E.J. Murphy, P. Ward, D.G. Bone, S.E. Thorpe, S.A. Grant, and R.S. Ladkin, 2003. Southern ACC Front to the northeast of South Georgia: Pathways, characteristics, and fluxes. *J. Geophys. Res.*, 108(C5), 3162.
- Moore, J.K., M.R. Abbott, and J. G. Richman, 1998. Location and dynamics of the Antarctic Polar Front from satellite sea surface temperature data. *J. Geophys. Res.*, 104(C2), 3059-3073.
- Müller, C., V. Schlindwein, A. Eckstaller, and H. Miller, 2005. Singing Icebergs. *Science* 310, 1299.
- NOAA, 2006. ETOPO2v2, U.S. Department of Commerce, National Oceanic and Atmospheric Administration, National Geophysical Data Center. *2-minute Gridded Global Relief Data*.
- Rust A.C., N.J. Balmforth, and S. Mandre (in press). *The feasibility of generating low frequency volcano seismicity by flow through a deformable channel*, In: The Physics of Fluid Oscillations in Volcanic Systems, Special Publication, Geological Society of London.
- Sandhäger, H., D. G. Vaughan, and A. Lambrecht, 2004. Meteoric, marine and total ice thickness maps of Filchner-Ronne-Schelfeis, Antarctica. In: Smedsrud, L.H. (Ed.), *comp. Forum for Research into Ice Shelf Processes (FRISP)*. Report No.15 (2004). Bergen, Bjerknes Centre for Climate Research, 23-29.
- Talandier, J. and E.A. Okal, 1998. On the mechanism of conversion of seismic waves to and from T waves in the vicinity of island shores. *Bulletin of the Seismological Society of America*, 88(2), 621-632.
- Talandier, J., O. Hyvernaud, E.A. Okal, and P.F. Piserchia, 2002. Long-range detection of hydroacoustic signals from large icebergs in the Ross Sea, Antarctica. *Earth and Planetary Science Letters*, 203, 519-534.
- Talandier, J., O. Hyvernaud, D. Reymond, and E.A. Okal, 2006. Hydroacoustic signals generated by parked and drifting icebergs in the Southern Indian and Pacific Oceans. *Geophys. J. Int.*, 165, 817-834.
- Trathan, P.N., M.A. Brandon, and E.J. Murphy, 1997. Characterization of the Antarctic Polar Frontal Zone to the north of South Georgia in summer 1994. *J. Geophys. Res.*, 102(C5), 10483-10497.
- VanWormer, D. and E. Berg, 1973. Seismic evidence for glacier motion. *J. Glac.*, 12(65), 259-265.
- Weaver, C.S. and S.D. Malone, 1979. Seismic evidence for discrete glacier motion at the rock-ice interface. *J. Glac.*, 23(89), 171-184.
- Wolf, L.W. and J.N. Davies, 1986. Glacier-generated earthquakes from Price William Sound, Alaska. *Bull. Seism. Soc. Am.*, 76(2), 367-379.